LASER SURFACE ALLOYING OF STAINLESS STEEL

Charles F. Marsden

Ph.D. Thesis

Imperial College,
University of London.

April 1988

ABSTRACT

This project has investigated the laser surface alloying of an AISI 420 stainless steel, (Fe-12 wt% Cr-0.2 wt%C) in order to modify its surface properties and to gain a better understanding of the pros and cons of the laser surface alloying technique in general.

The microstructures of alloyed zones were investigated by optical microscopy, X-ray diffraction. LIMA, and scanning and transmission electron microscopy; this study revealed very fine microstructures. The rapid cooling rates associated with laser processing enabled the martensitic transformation to occur in all the alloyed zones, except those where the M_s was depressed below room temperature by the presence of sufficient carbon.

Residual stresses were measured in and adjacent to several laser melted and alloyed zones, both parallel and perpendicular to the direction of laser travel, in planes parallel to the specimen surface. The magnitude and sense of the stresses were dependent on the structure of the alloyed zone.

As the 420 stainless steel is used in the power generating industry in environments where it is susceptible to water droplet impact erosion, cavitation erosion tests were carried out. The results showed that all the laser processed samples displayed superior erosion resistance to the conventionally quenched material, and that the erosion resistance appeared to be related to the hardness of the specimen surfaces.

ACKNOWLEDGEMENTS

I owe far more to my parents than to anyone else. Thank you for all the help and encouragement you have always given to me.

I wish to thank the many friends who have supported, helped and encouraged me throughout my time at University. One, however, stands out further than all the others; Sue, thank you very much.

The support and help mentioned above came mainly in the form of free beer and rent free accommodation - I promise I shall do my best to thank you all properly and possibly repay you before you are all duly rewarded in heaven (or hell!)

I am most grateful to my academic and industrial supervisors for their guidance, assistance and encouragement. Many thanks go to David West for his constant encouragement, endless constructive criticsm and overall guidance. Thanks go to Bill Steen for providing the laser facility without which this work would not have been possible and for his unbelievable enthusiasm. I would also like to thank Peter Flewitt at the CEGB, Gravesend for his highly constructive advice and for providing the residual stress measuring equipment as well as the ultrasonic eqiupment for the erosion apparatus.

My thanks go to several members of the Department of Metallurgy and Materials Science at Cambridge. Firstly, to Lindsey Greer for introducing me to the LIMA equipment; to Rob Wallach for allowing me time on the equipment and to both Rob Wallach and Andy Harris for operating the apparatus for me.

Thanks to the technicians in this department. To Russell Stracey and Paul Williams in the Laser Laboratory for their extremely rapid completion of all the jobs given to them and for maintaining the lasers. To Alec Neve and Melvyn Andrews for maintaining the equipment in the John Percy laboratory. To the entire workshop staff who carried out the many boring jobs given to them, in the minimum of time, to the highest degree of accuracy whilst maintaining their sense of humour. To the department's photographers, both past and present, for their efficiency and helpfulness, especially Paul Henry and Romy Driscoll.

It has been a pleasure to work in such a vibrant and active research group as the John Percy Group and I would like to extend my thanks to all members of the group, past and present, for their stimulating discussions, ideas and comments on metallurgy and many other wide-ranging subjects.

Thanks also go to past and present members of the John Percy Day Club, for the many enjoyable events and outings with which I have been associated.

I am happy to thank Gill Hopkins for accurately typing this thesis and remaining cheerful throughout.

Thanks to the SERC and CEGB SE Area for sponsoring this project.

CONTENTS

		Page
Abstract	.. ..	2
Acknowledgements	.. ..	3
Contents	.. ..	5
List of Symbols	.. ..	10
List of Figures	.. ..	12
List of Photographs	.. ..	15

CHAPTER 1 LASER PROCESSING

1.1	Introduction	17
1.2	The Laser	19
1.2.1	Parameters associated with the laser beam	20
1.2.2	Parameters associated with the specimen	21
1.2.3	Parameters associated with the processing arrangement	23
1.3	Laser transformation hardneing	24
1.4	Laser surface melting	26
1.5	Laser surface alloying	28

CHAPTER 2 EXPERIMENTAL PROCEDURES

2.1	The specimens	33
2.2	Processing apparatus	34
2.3	The Laser	34
2.4	Laser processing	35
2.5	Introduction of carbon into the molten pool	36
2.6	Specimen examination	39

		Page
CHAPTER 2	**EXPERIMENTAL PROCEDURES (continued)**	
2.7	Hardness	41
2.8	X-ray diffraction	41
2.8.1	Retained austenite measurements	41
2.8.2	Pole figures	43
2.8.3	Residual stress measurements	44
2.9	Erosion tests	44
2.10	Carbon analysis	44
CHAPTER 3	**STRUCTURAL FEATURES OF LASER SURFACE ALLOYING 420 STEEL WITH CARBON**	
3.1	Introduction	47
3.2	Experimental	48
3.2.1	Single tracks	49
3.2.2	Partially overlapping tracks	50
3.3	Results	50
3.3.1	Series I - Single cycle treatments	50
3.3.2	Series II	53
3.3.3	Series III	59
3.3.4	Series IV - Multicycle treatments	64
3.3.5	Partially overlapping tracks	67
3.3.6	Surface roughness	68
3.4	Discussion	70
3.4.1	Solidification	70
3.4.2	Solidification front morphologies	73
3.4.3	Solid state transformations	79
3.5	Conclusions	81

Page

CHAPTER 4 RESIDUAL STRESSES

4.1	Introduction	83
4.2	Sources of residual stress	84
4.2.1	Shrinkage	85
4.2.2	Plastic deformation at elevated temperatures	85
4.2.3	Phase transformations	86
4.3	Scope of the investigation	87
4.4	Experimental	88
4.4.1	Stress measurements	88
4.4.2	Principles of the X-ray technique	88
4.5	Specimens	92
4.6	Operation	93
4.7	Results	93
4.7.1	Computer output	93
4.7.2	Results of specimens 1, 2 and 3	97
4.7.2.1	Specimen 1 - Unalloyed	98
4.7.2.2	Specimen 2 - Alloyed	100
4.7.2.3	Specimen 3 - Alloyed	102
4.7.2.4	General trends	104
4.8	Discussion	105
4.8.1	Curvature in the plot of 2θ against $\sin^2\psi$	105
4.8.2	Peak broadening and microstress	106
4.8.3	Effect of material removal	108
4.8.4	Transformation plasticity	108
4.8.5	Plastic deformation at elevated temperatures	109
4.8.6	Stresses in the melted zone	110

			Page
CHAPTER 4	**RESIDUAL STRESSES (continued ...)**		
	4.8.7	Stresses away from the melted zone	111
	4.8.7.1	Explanation of the general trends	112
	4.8.7.2	Transverse stresses	117
	4.8.7.3	Longitudinal stresses	117
	4.9	Conclusions	117
CHAPTER 5	**EROSION**		
	5.1.1	Introduction	119
	5.1.2	Mechanism of erosion	120
	5.1.3	Damage resistance of metals	122
	5.2	Experimental	122
	5.2.1	The apparatus	122
	5.2.2	The specimens	124
	5.3	Results	126
	5.3.1	Erosion data	126
	5.3.2	Damage to the specimens	130
	5.3.3	Damage to the horn	133
	5.4	Discussion	133
	5.4.1	Erosion data	133
	5.4.2	The specimens	134
	5.4.3	The horn tip	136
	5.5	Conclusions	137
CONCLUSIONS:			
	Structures		138
	Residual stresses		139
	Erosion		140

Page

FUTURE WORK 141

REFERENCES 142

APPENDIX 1 148

APPENDIX 2 154

APPENDIX 3 158

APPENDIX 4 160

LIST OF SYMBOLS

C	Constant
C_o	Initial solute concentration
D	Beam diameter, diffusivity of the solute in the liquid state
e^{-2M}	Debye-Waller temperature factor
E	Youngs modulus
$E_{C/Cr}$	Correction factor
f	Atomic factor
F	Structure factor
G	Temperature gradient in the liquid
I	Intensity
(hkl)	Miller indices
k_o	The ratio of the solute concentration in the solid to solute concentration in the liquid
K	Constant
m	Multiplicity factor, constant
M	Slope of liquidus, mass loss, constant in Debye-Waller temperature factor
M_s	Martensite start temperature
n	Number of cells in 1 cm^3
P	Beam power, ratio of integrated intensities of martensite to austenite

R	Velocity of solid/liquid interface
R_a	Centreline average roughness
t	Time
T	Freezing time
v	Volume of unit cell
V	Transverse velocity, volume exposed to X-ray
X	Depth of melt zone
Y	Length of melt zone behind line of maxmimum depth of melt pool
α	Ferrite, martensite
γ	Austenite
δ	Delta Ferrite
ε	Strain
$\dot{\varepsilon}$	Strain rate
ε_{Ψ}	Strain at an angle
Θ	Angle
σ	Applied stress, standard deviation
σ_y	Yield stress of weaker phase
ν	Poisons ratio
Ψ	The angle between the direction of the measured strain and the normal to the specimen surface
λ	Wavelength

LIST OF FIGURES

Figure 1.1	Operating regimes for laser processing
Figure 1.2	Some low order TEM mode profiles
Figure 1.3	Various cross-sectional profiles of melt zones
Figure 2.1	Arrangement of laser processing apparatus
Figure 2.2	Shrouding and beam focussing arrangement
Figure 2.3	Typical plot from LIMA apparatus
Figure 3.1	Dimensions of melt zone against transverse rate
Figure 3.2	Hardness against depth for alloyed specimen
Figure 3.3	Hardness against mass of carbon coating
Figure 3.4	Average hardness against number of treatment cycles
Figure 3.5	Hardness against depth for different number of treatment cycles
Figure 3.6	Percentage retained austenite against mass of carbon coating

Figure 3.7 Section through Cr-C-Fe phase diagram at 13 wt%Cr

Figure 3.8 Composition of solidification cell

Figure 3.9 Fe rich corner of metastable C-Cr-Fe liquidus surface

Figure 3.10 The influence of G and R on solidification morphology

Figure 3.11 Schematic representation of solidification

Figure 3.12 Longitudinal section of melt zone to illustrate the relationship between V, R, and Θ

Figure 4.1 Schematic showing the relationship between σ, Θ, Ψ, the X-rays and the specimen surface

Figure 4.2 Display of co-ordinates of points at which stress measurements were made

Figure 4.3(a) Output from computer

Figure 4.3(b) Output from computer

Figure 4.4 Specimen 1-Unalloyed, transverse stresses

Figure 4.5 Specimen 1 - Unalloyed, longitudinal stresses

Figure 4.6 Specimen 2 - Alloyed, transverse stresses

Figure 4.7 Specimen 2 - Alloyed, longitudinal stresses

Figure 4.8 Specimen 3 - Alloyed, transverse stresses

Figure 4.9 Specimen 3 - Alloyed, longitudinal stresses

Figure 4.10 Full width half heights against depth

Figure 4.11 Thermal transients at the surface

Figure 4.12 Schematic representation of residual stress "build-up" after Macherauch[68]

Figure 4.13 Schematic representation of transverse residual stress "build-up"

Figure 4.14 Schematic representation of longitudinal residual stress "build-up"

Figure 5.1 Typical mass loss against time of exposure curve

Figure 5.2 A schematic representation of the experimental apparatus

Figure 5.3 Mass loss against time for different samples

Figure 5.4 Mass loss per hour against hardness

Figure 5.5 Final surface roughness against hardness

LIST OF PHOTOGRAPHS

Photograph 3.1 Transverse section through laser melted parent material

Photograph 3.2 Transverse section through laser alloyed zone

Photograph 3.3 TEI of alloyed zone

Photograph 3.4 SEI of transverse section through laser alloyed zone

Photograph 3.5 Longitudinal section of laser alloyed zone at 90^{o} to surface

Photograph 3.6 Transverse section through laser alloyed zone, with hardness indentations corresponding to Figure 3.2

Photograph 3.7 Transverse section through laser alloyed zone, showing discrete areas of damage caused by LIMA apparatus

Photograph 3.8 Transverse section through laser alloyed zone

Photograph 3.9 TEI of eutectic between dendrites

Photograph 3.10 Transverse section through laser alloyed zone with planar solidification front

Photograph 3.11 Transverse section through laser alloyed zone

Photograph 3.12 Longitudional section of laser alloyed zone at 90^{o} to the surface

Photograph 3.13 Polished and eteched top surface of alloyed zone

Photograph 3.14(a) Transverse section through laser alloyed zone

Photograph 3.14(b) Transverse section through laser alloyed zone

Photograph 5.1 Specimen A after 1 hour of exposure

Photograph 5.2 Specimen A after 3 hours of exposure

Photograph 5.3 Specimen A after 3 hours of exposure

Photograph 5.4 Specimen E after 2 hours of exposure

Photograph 5.5 Specimen E after 3 hours of exposure

Photograph 5.6 Specimen E after 7 hours of exposure

Photograph 5.7 Specimen A after 8 hours of exposure

Photograph 5.8 The horn tip after a 30 hour test

CHAPTER 1

LASER PROCESSING

1.1 Introduction

The first successful operation of a laser was achieved in 1960 by Theodore H. Maiman. After this lasers were developed rapidly and by 1964 machines capable of producing short pulses with peak powers of a billion (10^9) watts had been constructed. These lasers were not suitable for laser surface processing of materials because their pulse rate was too slow to be of use. In the late 1960's the Carbon Dioxide Laser was invented which produced a continuous wave {CW} of laser radiation. Development of the CO_2 laser during the early 1970's enabled the introduction of reliable, high powered, continuous wave sources of laser radiation, capable of producing many kilowatts of power.

These high power density energy sources can be used in many fields of materials processing. Figure 1.1 after Oakley[1] shows some of the operational regimes for laser materials processing, plotted against power density expressed in watts/cm^2 and interaction time. Processing commonly involves moving the specimen under a laser beam. Interaction time is the time that a particular point on the surface is "seen" by the laser and can be approximated to the beam diameter (D) divided by the traverse rate (V), i.e., D/V.

Amongst the regimes shown in Figure 1.1 are:
Laser transformation hardening;
Laser surface melting;
Laser surface alloying.

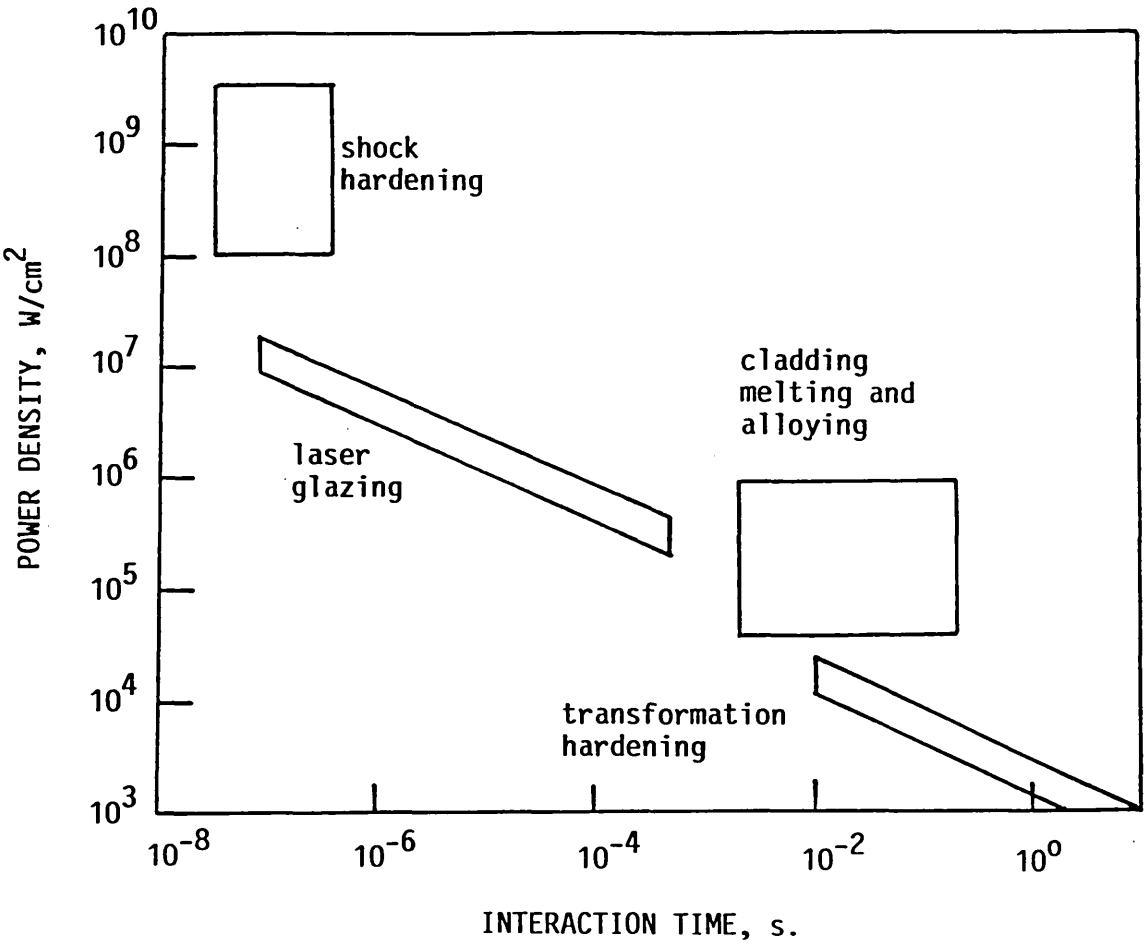


FIGURE 1.1

Operating regimes for laser surface treatment of materials [1]

These techniques and applications will be described later in the following sections, with emphasis placed upon laser surface alloying, as it is around this subject, using a substrate of AISI 420 steel (~ 13 wt% Cr, 0.2 wt % C), that this project is based. Using a 2kW carbon dioxide laser, it is predicted that by enriching the carbon content of the AISI 420 steel that its hardness may be increased.

1.2 The Laser

A CO_2 CW laser is an intense source of monochromatic electro-magnetic radiation in the near infrared region of the spectrum with a wavelength of 10.6 μm. In this work a Control Laser Limited "910" fast axial flow carbon dioxide laser was used.

The advantages of using a laser as a heat source in some fields of materials processing are numerous:

1) It is clean;

2) It is easily conveyed to work stations in air;

3) Shape and area of heated zone are easily controlled;

4) Instant switch on/off;

5) Total heat input low and highly localised; minimising the chances of thermal distortion;

6) If an area can be seen it can be treated;

7) Adjustable power density from 10^7 to 10^2 watts/cm^2;

8) Only the surface layer is affected, therefore the bulk material properties can be retained;

9) Lends itself to automation.

1.2.1 Parameters associated with the laser beam

These parameters are:

i) Wavelength;
ii) Power;
iii) Beam diameter;
iv Power distribution across the beam;
v) Divergence;
vi) Plane of polarisation.

Apart from the wavelength, which is fixed for all CO_2 lasers the other parameters may be varied.

The power of the beam can be altered by changing the current in the discharge tubes.

The beam diameter can be changed by focussing or over focussing the beam by either lenses or focussing mirrors. The lenses used are of two types, potassium chloride (KCl) or zinc selenide (ZnSe). Both these materials have low absorption at 10.6 μm. Zinc selenide lenses are more resistant to damage than potassium chloride lenses, which are also hydroscopic and become misted unless stored in a dry atmosphere; however, the zinc selenide lenses are an order of magnitude more expensive. Focussing mirrors are usually used on lasers of approximately 5kW or more.

The power distribution across the beam is referred to as the mode structure. Figure 1.2 shows a number of mode profiles. TEM_{00} is the lowest order mode, frequently referred to as the Gaussian mode. The TEM_{01*} mode is the so called "doughnut" mode.

The divergence of the beam is mainly affected by two factors: (i) the cavity optics and (ii) the mode structure. The cavity optics remained unchanged throughout the present work as did the mode structure, identified as TEM_{01*} by a laser beam analyser.

The TEM_{00} mode produces the smallest diameter and lowest divergence laser beam[2]. Multi-mode operation is often employed in materials processing where the beam is not focussed to a small spot as it increases the output power but decreases the coherence and increases the divergence[2]. As the distance between the laser and the work station is relatively short, about 3 metres, this decrease in coherence and increase in divergence is not important in the present work.

The plane of polarisation of the laser beam is of importance only when applications of drilling, scribing, cutting and deep penetration welding are required[3]. The laser beam used in the present work was plane polarised.

1.2.2 Parameters associated with the specimen

These parameters are:

1) Absorbtivity and its variation with temperature;

2) Thermal diffusivity and its variation with temperature;

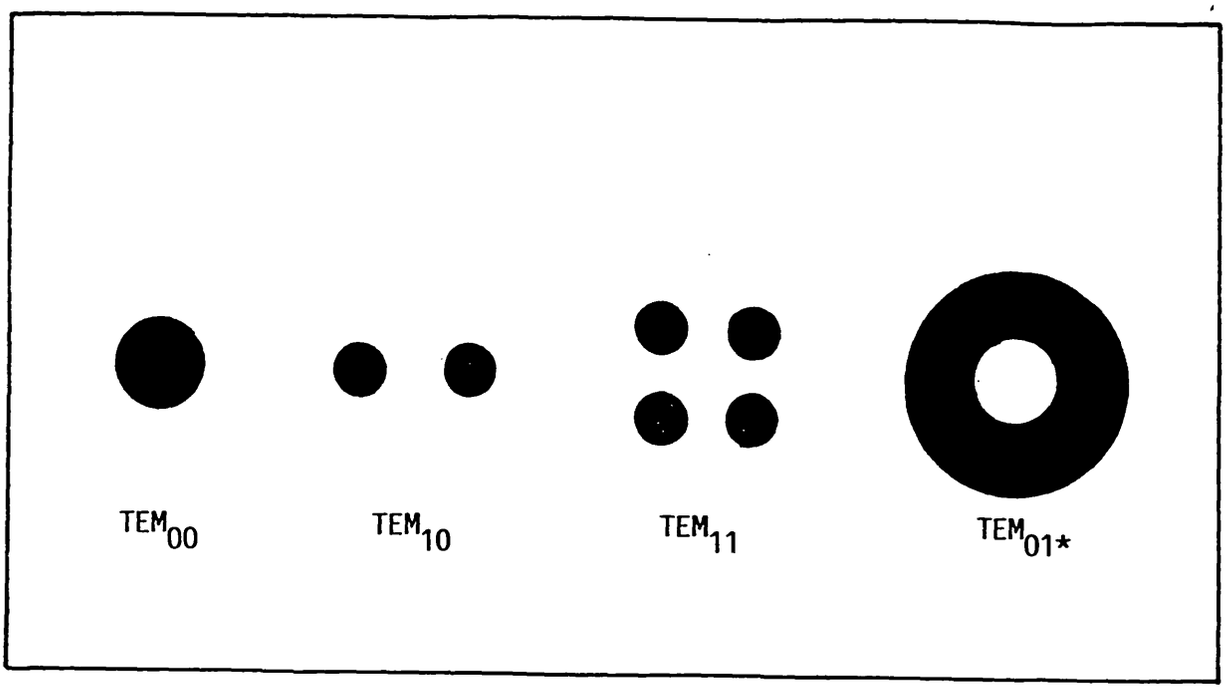


FIGURE 1.2

Some low order TEM mode profiles

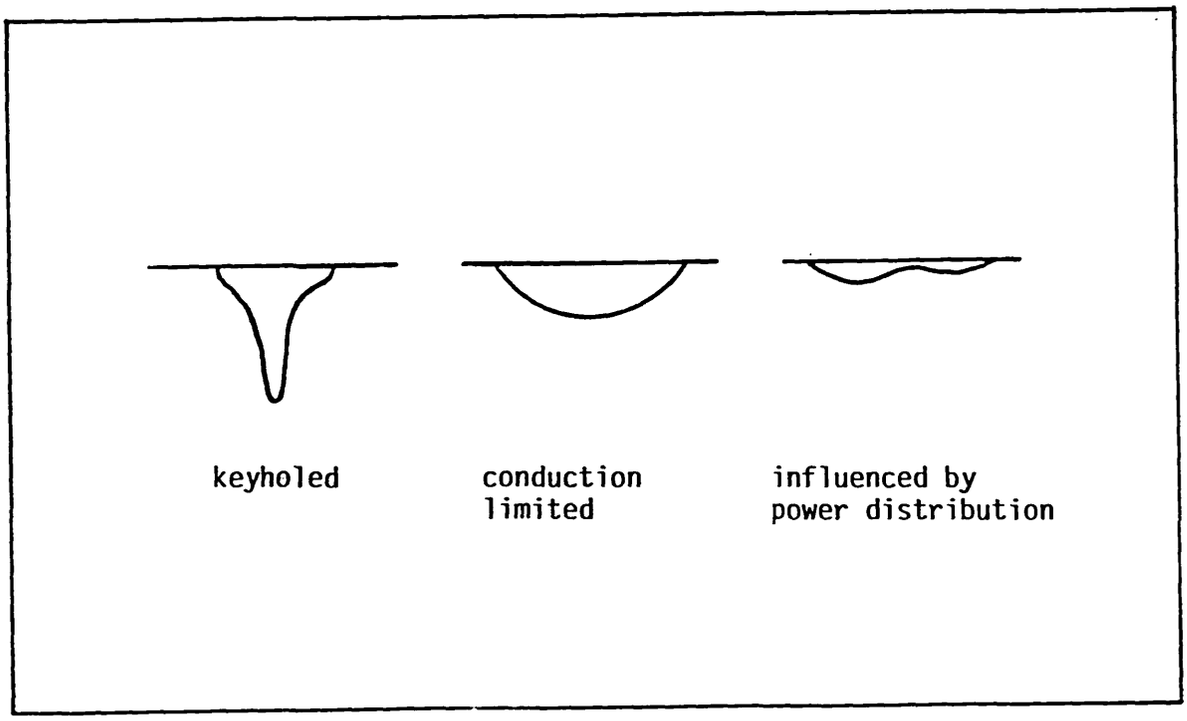


FIGURE 1.3

Various cross-sectional profiles of melt zones

3) Surface tension and its variation with temperature;

4) Ionization potential;

5) Bier-Lambert co-efficient;

6) Latent heats of transformations.

The absorbtivity of a metal surface for a laser beam is sensitive to both the temperatures and the surface finish. A cold steel surface reflects ~95% of 10.6 μm radiation incident on it[4]. However, there is some heating and as the surface is heated its absorbtivity increases, increasing the efficiency of the laser/metal coupling.

Previous work by Lamb[5] on stainless steels found that grit blasting offers the most acceptable method of surface preparation prior to laser processing.

1.2.3 Parameters associated with the processing arrangement

These are:

1) Characteristics of the optics that are outside the laser;

2) Shrouding gas;

3) Velocity of the specimen relative to the incident beam.

The CO_2 CW laser produces light with a wavelength of 10.6 μm which is attenuated if it passes through a humid

atmosphere. There will also be power losses associated with the various optical surfaces the laser beam encounters. These are typically ~1% for each gold coated copper mirror and ~5% for a potassium chloride lens according to the manufacturers literature.

The characteristics of a focussing system and mode structure of the beam define the power distribution across the specimen. In this study the focussing arrangement consisted of a potassium chloride lens, of focal length 75mm lying normal to and in the centre of the axis of the laser beam.

1.3 Laser transformation hardening

Laser transformation hardening involves heat treating a material, usually a hardenable steel or cast iron, through a prescribed time-temperature history, without surface melting, by which the surface microstructure is transformed to martensite. High power CO_2 lasers can be used to selectively heat areas on the surfaces of engineering components after which these regions are rapidly quenched by the conduction of heat into the bulk of the substrate. This highly selective heating minimises thermal damage to a component being treated.

In practice, induction hardening provides a practical means of locally transforming hardening steels, and is used for the mass production of AISI 420 (~ 13 wt % Cr 0.2 wt % C) steel components. Induction heating of this steel in the solid state requires long soak times to produce full hardening. Surface hardening of thicknesses from 0.25 mm to 2.5 mm is often produced. However, because of the way the electromagnetic fields

from the induction head couple into the metal, the amount of induced current and resulting surface heating of an uneven shaped piece may vary with location. For example, if there is a protruding region a significant amount of R.F. radiation will be absorbed in that region, with relatively little heating in the adjacent regions. As a result, it may be difficult or impossible to achieve the desired heat treatment pattern in parts of a complicated shape. The flexible nature of the laser processing is well suited to complicated shape components and the laser technique has been used to generate surface hardening in thicknesses up to 2.5 mm in heat treatable materials.

A number of workers have studied laser transformation hardening of iron carbon alloys with Steen[6] (1979) showing that the case depth is proportional to $P(DV)^{-1/2}$ and that cooling rate as high as $10^4\ ^oCs^{-1}$ can be achieved. P = Power, D = beam diameter, V = traverse velocity.

Laser hardening of a 12% Cr steel was studied by Roth and Cantello[7]. The full potential hardness. ~ 500-600 Hv after an oil quench from > 900°C, was achieved on flat plates of the material. Hardened martensitic zones up to 1.1 mm in depth were produced. Bedogni et al[8] have achieved transformation hardening of the curved surface of the leading edge of a steam turbine blade, to a uniform depth of approximately 1mm, in one pass of the laser using a novel beam shaping technique. The material was also a 12 wt % Cr steel. Although laser transformation hardening has many advantages over other hardening techniques its use in industry has been limited. The earliest reported industrial application was for the selective hardening of main bore surfaces of power steering gear houses in 1974 at the Saginaw steering works of General Motors Limited[9].

1.4 Laser surface melting

Laser surface melting is an extension of laser transformation hardening whereby the surface layer being treated is allowed to melt and again, once the beam has passed, the treated area rapidly cools and solidifies by conduction of heat into the substrate. The technique uses a variety of powers, beam diameters and traverse rates with the aim of modifying and improving the resistance to corrosion, erosion, fatigue and/or hardness of the material surface.

Different combinations of power density and speed of traverse can produce melted zones of different cross sections, see Figure 1.3. For small or focussed beams, fast traverse rates are utilised to avoid "key-holing". For larger beams, slower traverse rates are used to ensure melting of the surface. The rate of cooling and hence solidification decreases with decreasing traverse rates, this being due to the overall heat input increasing. These variations in cooling rate can lead to different solidification structures being produced. At very high cooling rates 10^6 ^oC or higher, laser glazing occurs. This technique utilises the focussed beam travelling swiftly ($1.0\ ms^{-1}$) over the surface of the workpiece. The thin molten trace produced then self quenches. This extremely high quench rate will almost always result in the production of a metastable structure in the surface layer. Kear et al[10] have produced metallic glass layers with a fully non-crystalline (amorphous) structure in a Pd/Cu/Si eutectic alloy.

At progressively lower cooling rates depending on the alloy composition, crystals grow epitaxially from the unmelted zone and eventually the structure will consist of

dendrites and/or cells. The dendrites will be very small, often submicron, due to the comparatively high cooling rates when compared with conventional solidification. When an alloy of eutectic composition solidifies, the interlamellar spacing can be equally small. Surface homogenisation is very similar to laser glazing but is usually slower and requires more energy input. The aim of this process is to melt a reasonably deep layer, dissolve all phases and quench rapidly so that they do not separate out again. Anthony and Cline[11] demonstrated how surface homogenisation could be used to eliminate integranular corrosion in a sensitised stainless steel, by redissolving the chromium carbides and cooling rapidly by self quenching through the sensitization temperature range.

Chen et al[12] have worked extensively on laser melting of cast irons. On melting Silal, Ni-hard, Ni-resistant and high Cr cast irons, the hardness of all the structures was generally increased due to the graphite to cementite and austenite to martensite transformations. Porosity occurred in the Ni-resist alloy due to dissolved gases, which in cast irons are often absorbed in the graphite phase. Cracking occurred for the more brittle structures due to the high residual stresses generated in laser surface melting. High nickel alloys rarely cracked due to their increased toughness. The resistance to wear of the Silal and Ni-resist alloys was enhanced greatly by laser surface melting[13].

Steen et al[14] give a useful summary for various cast iron alloys of their tendency to form cracks and porosity on cooling rate after laser surface treatment. Flake graphite cast iron is the most likely to form both porosity and cracks at all cooling rates with spheroid graphite cast iron, and white cast iron likely to crack at

all cooling rates with Silal tending to crack at high cooling rates only.

Huberty and Nilmen[15] concluded that by laser melting, the hardness of two tool steels could be increased together with a more homogeneous distribution of carbides in the surface layers, leading to the tendency of tools cracking under service conditions being reduced.

Extensive work has been carried out on AISI 316 Austenitic stainless steel (~ 17 wt % Cr 11 wt % Ni 2.4 wt % Mo) and 420 Martensitic stainless steel (~ 13 wt % Cr 0.2 wt % C) by Lamb[5]. The 316 steel did not benefit from laser melting as both the mechanical and electrochemical properties of the material were degraded. However, laser melting of the 420 steel developed the full hardness of the material, and both fatigue life of a test piece and the corrosion pitting resistance were enhanced. The full hardness of the material developed on laser melting caused the surface to be in a state of compression. The combination of these effects prevented fatigue cracks from initiating and growing in this layer. The cracks initiated at inclusions in the matrix below the heat affected zone of the laser treated layer, grew into the softer parent material before brittle fracture occurred. The corrosion pitting resistance was enhanced as the laser melting dissolved the carbide particles and redistributed their chromium and other alloying elements. The compressive residual stresses introduced by the laser melting also enhance the pitting resistance.

1.5 Laser Surface Alloying

Laser surface alloying is a process which uses similar processing techniques as laser melting, the difference in the processes being the addition of foreign

material which mixes with the substrate material in the molten phase. This leads to a surface layer with chemical composition and mechanical properties different from those of the bulk, the aim being to improve the chemical and physical properties of the substrate. The addition of alloying elements can be achieved by a variety of methods too numerous to mention. Here are but a few:-

i) Pre-placed material. Powders, plating, thin foil applications, pre-placed wires, sputter coating, vaporisation, evaporation;

ii) Ion implantation;

iii) Powder injection;

iv) Gaseous injection.

The major advantage of laser surface alloying is that a part can be fabricated from a base metal selected on the basis of cost and mechanical properties. The working surface can then be modified using the high power laser beam, to provide the desired characteristics necessary for the end use application.

Laser surface alloying has been studied extensively in relation to the processing of semi-conductors but relatively little work has been done in the field of metallic materials; the review by Draper[16] in 1985 describes most of the fields in current research.

However, laser surface alloying will gain considerable interest in the near future when the savings mentioned earlier are more fully realised, and especially where savings on strategic and precious metals can be made.

The review below concentrates on laser surface alloying using ferrous substrates and does not cover the whole of the alloying literature.

Walker[17] has surface alloyed pure iron and S135 (Fe-1 wt%C-1.4 wt% Cr) steel with carbon in the form of Dag graphite. The carbon content of the substrate was increased by re-applying the Dag graphite and re-melting. In this way surface layers ranging from hypo-eutectic to hyper-eutectic cast irons were produced. Significant porosity and cracking occurred, particularly at the hyper-eutectic level. The rapid solidification associated with laser processing produced a range of fine, white iron structures whose features depend on carbon content, mixing conditions in the melt and cooling rate. The eutectic structures produced showed interlamellar spacings of < 1 μm and at room temperature consisted of Fe_3C + ferrite and/or martensite. Hardnesses up to 900 HV were achieved.

Alloying carbon into C10 (0.1 wt %C) and ST22 (low carbon steel with U.T.S. 220 Nmm^{-2}) steels by melting in an atmosphere of CO_2 or acetylene has been carried out by Mordike et al[18]. Structures ranging from the parent materials up to hyper-eutectic were achieved, with acetylene being the most efficient carburizing gas. Hardnesses of 600 HV were achieved in the very fine dendritic austenite, whilst hardnesses of about 1200 HV were achieved in the hyper-eutectic structures.

Chen[13] has alloyed flake graphite cast iron, using a powder delivery system developed at Imperial College[19], with a number of powders including Si, Cr, SiC + C, Cr + C, Cr + V, Cr + Ni and Nb. Alloys with up to 10 wt % Si, 35 wt % Cr, 50 wt % Cr + V, 17 wt % Cr + Ni and 20 wt % Nb were produced. The hardnesses of the alloys produced, up to

900 HV, were greater than that of the parent material in either its as-received condition or after laser surface melting. The alloys created after adding Cr + V and Cr + Ni powders, whose compositions were Fe-3 wt % C-2.8 wt % Cr-0.6 wt % V and Fe-3wt % C-3.2 wt % Cr-1.9 wt % Ni respectively, displayed superior wear properties to the laser surface melted Ni-resist and Silal alloys which, as mentioned previously, were more wear resistant than prior to laser treatment.

Much work has been done on the alloying of chromium into ferrous substrates. Das, Dumler and Mazumder[20] have alloyed Cr into an Fe-Cr-C alloy by powder injection into the melt pool in order to study and understand the effect of microstructure on wear properties. They found that unique microstructures could be formed. For example. structures for corrosion resistance were produced with chromium contents of 40% uniformly distributed throughout the matrix and structures for wear resistance were produced with a uniform distribution of carbides throughout the matrix.

Moore[21] produced stainless steels of varying chromium content on a mild steel by coating specimens with chromium of thicknesses varying between 1 μm and 20 μm and melting these at speeds and powers varying from $100mms^{-1}$ to $4000mms^{-1}$ and 2kW to 9kW. The chromium content varied slightly through the track depth: to eliminate this trend the alloying procedure should be carried out again at 90^{o} to the first. This is especially important if the alloyed surface is to be used under corrosive conditions. as corrosion resistance requires that the entire surface be uniformly alloyed to provide protection.

Molian and Wood[22] laser surface alloyed thin and thick chromium coatings on 0.5 and 1.0 wt % C steels to generate

alloys containing 10, 20 and 40 wt % Cr to a nominal depth of 200 μm.

Having considered ferrous alloys it is of interest to note briefly work on titanium alloys. The martensitic transformation does not produce major hardening. However, the formation of hard components by gaseous alloying of titanium with nitrogen has been achieved. This has been carried out using CO_2 lasers by Folkes[23] and with both CO_2 and pulsed YAG lasers by Katayama et al[24]. Both were successful in producing TiN layers in an atmosphere of pure nitrogen. Again, there are few industrial applications of laser surface alloying, because only recently has the technique been employed in the field of metallic materials.

CHAPTER 2

EXPERIMENTAL PROCEDURES

2.1 The Specimens

The specimens were flat discs 10mm thick and 32mm in diameter cut from a bar of fully tempered 420 steel. The composition of the material is given below in Table 2.1.

Table 2.1

Composition of 420 Stainless Steel

Element, weight %										
C	Cr	Cu	Fe	Mn	Mo	Ni	P	S	Si	V
0.19	12.6	--	bal.	0.66	--	0.14	0.01	0.007	0.35	--

The bar was oil quenched from 960^{o}C and tempered for 1 hour at 760^{o}C; the structure consisted of coarse $M_{23}C_6$ carbides and ferrite. The discs were ground flat on a workshop wheel with a continuous flow of coolant. The specimens were then degreased in acetone, grit blasted and degreased once more. That was the condition of all specimens prior to laser treatment unless otherwise stated. This was to ensure a standard uniform surface finish which would help absorb the 10.6 μm radiation.

2.2 Processing Apparatus

The overall arrangement of the apparatus is shown in Figure 2.1. After leaving the laser the beam goes to either the water cooled calorimeter or the workstation. The beam is directed by flat gold plated mirrors. The orientation of these mirrors is adjusted using a visible milliwatt helium-neon laser which is directed to run co-axially with the main beam.

The hydraulic trolley moves along guide rails. A hand screw permits shifting perpendicular to the direction of travel and the production of surfaces that are covered with the over-lapping melt tracks. The guide rails were always clamped to a solid object to prevent movement of the trolley sideways when it was accelerated. The speed of the trolley was measured with a microswitch which activated a timer while the trolley covered a distance of 100mm.

The shrouding arrangement and the lens holder are shown in Figure 2.2. A gold plated mirror reflects the beam downwards to the lens. The nozzle and the flow of argon through the nozzle protect the lens from debris that is thrown up during laser surface treatment. Specimens were inserted into holes in a template so that the surfaces to be laser processed were flush with the template surface. This enabled very good shrouding to be achieved with argon gas flowing through the shrouding plate and through the nozzle, which minimised oxidation and other surface contamination during processing.

2.3 The Laser

The Control Laser Limited "910" fast axial flow carbon dioxide laser used for the work, is capable of supplying powers in the range from 500W to 2kW. A mixture of carbon dioxide, nitrogen and helium flows through the four discharge

tubes. An electrical current flowing through the tubes in the direction of gas flow, pumps the carbon dioxide by way of electron collisions and indirectly by way of vibrationally excited nitrogen, Duley[4]. The helium acts as a coolant and helps to maintain the population inversion that is essential for the lasing action. When the beam is not directed to the specimen it is dumped in a copper cone calorimeter.

The power of the laser is measured by monitoring the temperature rise of the cooling water that flows around the cone.

There is a 300 Hz ripple frequency on the laser beam. This gives rise to "stitched" welds at high traverse speeds, Alexander[25]. This oscillation arises from the rectification of the 50Hz three phase power supply.

Since even diffuse reflections from the laser are harmful a number of safety precautions are recommended, ANSI 1976[26].

In outline they are:

1) Operator training;
2) Eye protection;
3) Enclosed beam path;
4) Remote firing;
5) Key switch interlocks;
6) Restricted entry to the laser area.

2.4 Laser Processing

Three of the processing parameters were varied, the beam diameter, D, the power, P and the traverse velocity, V.

The diameter of the incident laser beam on the specimen was varied by moving the lens up and down relative to the specimen. The incident beam diameters that are quoted in this work were calculated by assuming that the beam diameter varies linearly from the focal point to its diameter measured at the workstation before entering the lens. The diameter of the beam at the focal point depends on optical aberrations in the lens and on the diffraction imposed limitation of the beam diameter. The beam diameter at focus was taken to be 400 μm and the diameter at the workstation before entering the lens was taken to be 20mm, Lim and Steen[27].

The location of the focal point was found by moving a specimen up and down below the lens and looking for the blue flash that is characteristic of the ionisation that occurs at high energy densities. The highest and lowest positions which produced blue flash were measured and the focal point was taken to be half-way between them.

The beam power was varied by desaturating the discharge tubes. The traverse velocity of the specimen was varied by adjusting a valve leading to the hydraulic ram. A beam diameter for the laser alloying was chosen that was large enough to avoid keyholing, whilst being small enough to minimise the effects of any irregular power distributions across the beam.

All work was carried out using a 1.6 kW beam with a 2mm diameter, unless otherwise stated.

2.5 Introduction of Carbon into the Molten Pool

The method and control of carbon into the molten pool is described in Chapter 3, Section 3.1

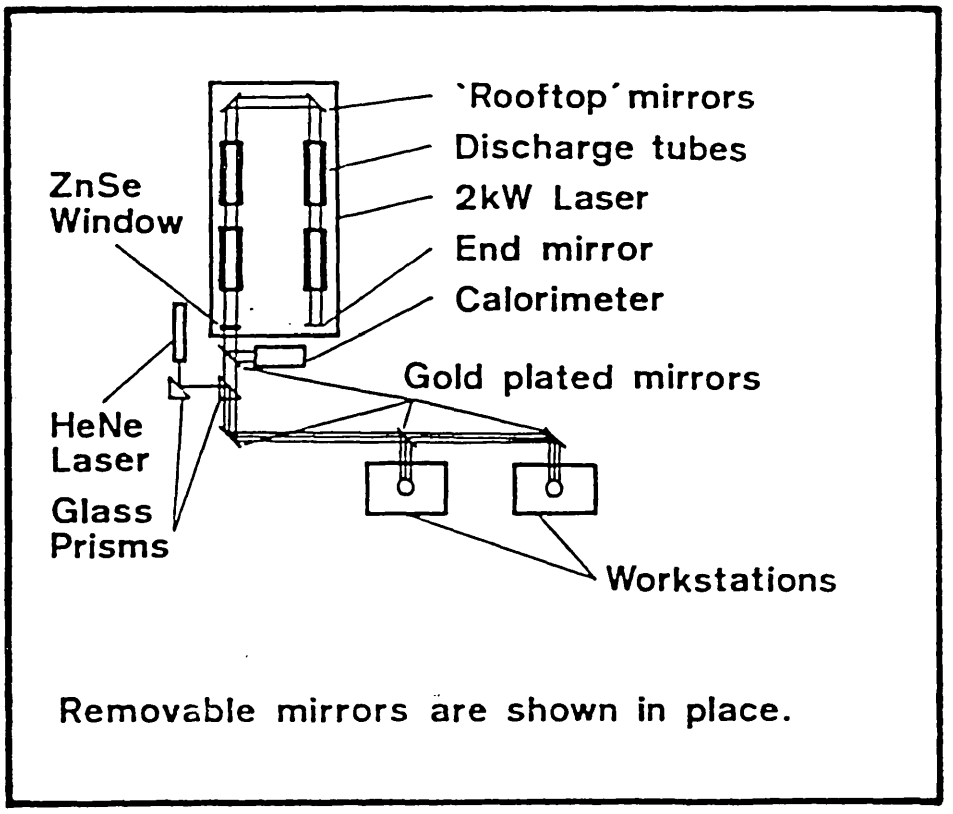


FIGURE 2.1

Arrangement of the laser processing apparatus[5]

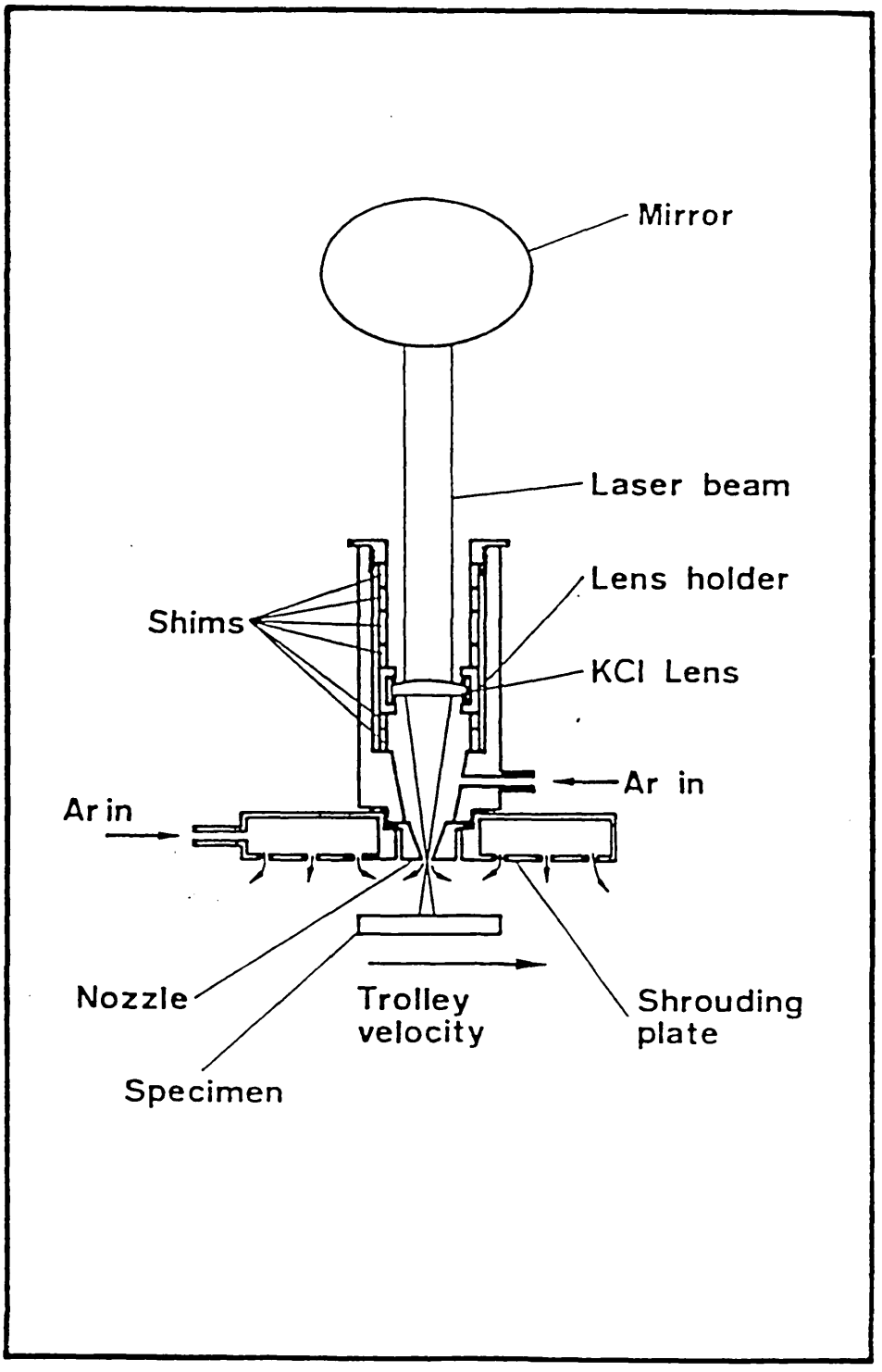


FIGURE 2.2

Shrouding and beam focussing arrangement[5]

2.6 Specimen Examination

After treatment the specimens were examined for oxidation, and surface roughness measurements were made both along and across single and over-lapping tracks using a Taylor-Hobson Talysurf. The results are centreline average values (CLA), R_a. The preparation for optical and scanning electron microscopy work was as below:

i) Section the specimen with a laboratory cut off wheel;

ii) Grind the cut off surface on 320, 400, 600, 800, and 1200 grit grinding paper;

iii) Polish with 6, 1, 1/4μm diamond paste on a napped cloth;

iv) Etch.

Etching was by one of the following reagents:

i) Villela's Reagent. (5ml hydrochloric acid, 1g picric acid and 100ml methanol). This was used to show the general structure of the steel;

ii) Acid Chloride Etch. (10ml hydrochloric acid in 100ml ethanol). This was used to show the general structure of the steel. The specimen was etched either by immersion in warm (25^{o}C) etchant or electrolytically (6V) to show the martensitic structure.

After etching, the depths of the melt zones were measured on a random transverse section and microhardness measurements were taken on the cross sections. The width of the tracks were measured from the track tops. Occasionally

longitudinal sections were examined and uniformity of depth was observed.

Preparation for transmission electron microscopy

1) A slice of material containing the laser treated area was removed parallel to the specimen surface with a slitting wheel under flood cooling to avoid heating.

2) The specimens were ground down to between 50 and 80μm thickness on silicon carbide paper. Initial grinding was on 220 grit paper while the last 50μm was removed using 1200 grit paper. Material was removed from the underside of the treated region.

3) A 3mm disc was then "punched" out of the specimen.

4) Electrochemical thinning of the 3mm disc was carried out in a Struers "Tenupol" machine. The electrolyte used was a solution of 10 vol % perchloric acid, 15 vol % glycerol and 75 vol % ethanol. This solution is potentially explosive and must be kept below $30^{o}C$. Thinning was carried out at a potential of 15 volts and a temperature of $\sim -10^{o}C$.

5) Immediately after a hole had been produced in the 3mm disc, the disc was removed and washed in ethanol, before being rinsed in acetone and left to soak in a final bath of acetone.

6) Specimens were stored in a desiccator to prevent contamination.

After preparation, foils were examined in either a JOEL "120 Cx" scanning transmission electron microscope or an AEI EM7 high voltage (1000 kV) microscope. Also a JOEL

"2000 Fx" microscope with an EDS detector connected to a Link AN 10,000 computer system for analysis, was used to determine the Cr distribution across several solidification cells.

2.7 Hardness

Hardness surveys were carried out using both a Vickers hardness machine, with a load of 10kg and a Lietz Miniload 2 with a load of 0.1 kg. When a hardness number is quoted it is an average of approximately 10 values.

2.8 X-Ray Diffraction

2.8.1 Retained austenite measurements

Specimens consisting of over-lapping tracks covering an area of at least 100mm^2 were rotated over a range of values of 2θ (the angle between the X-ray source and the specimen surface) between 20^o and 105^o. The specimens were spun during diffractometry to minimise any texture effects. The work was usually carried out on the top surface of the as-laser processed specimens, however, the retained austenite contents of a number of specimens were measured at different depths. This required material to be removed by electropolishing. The electrolyte used was the same as that employed for electro-chemical thinning, as described above, though electropolishing was carried out at 0^{o}C. A Philips "PW 710" diffractometer was used with Cu Kα radiation. The peaks were indexed and the crystal structure identified.

The method employed is based on comparing the integrated intensities of selected (hkl) reflections of the austenite and martensite phases. The integrated intensity of a diffracted line, after Durnin and Ridal[28], is given by :

$$I_{(hkl)} = n^2 Vm(LP)e^{-2M}(Ff)^2 \qquad [2.1]$$

in which $I_{(hkl)}$ = integrated intensity for a special (hkl) reflection;
n = number of cells in 1 cm^3;
V = volume exposed to the X-ray beam;
(LP) = LORENTZ-POLARIZATION factor;
m = multiplicity of (hkl);
e^{-2M} = Debye-Waller temperature factor;
F = structure factor;
and f = atomic factor.

For n^2V we may substitute V/v^2 in which v is the volume of the unit cell.

If the ratio between the integrated intensities of martensite and austenite is denoted by P:

$$P = \frac{I_{martensite(\alpha)}}{I_{austenite(\gamma)}} = \frac{V_\alpha v_\gamma^2 m_\alpha (LP)_\alpha e_\alpha^{-2M}(F_\alpha f_\alpha)^2}{V_\gamma v_\alpha^2 m_\gamma (LP)_\gamma e_\gamma^{-2M}(F_\gamma f_\gamma)^2} \qquad [2.2]$$

values of f were obtained from the International Tables[29]. Values of LP, F, v and M (for e^{-2M}) were obtained from Elements of X-ray Diffraction by Cullity[30] and apart from v are all dependent upon the reflections used.

Equation [2.2] may be simplied to:

$$P = \frac{V_\alpha}{V_\gamma} \frac{C_{\alpha(hkl)}}{C_{\gamma(hkl)}} \qquad [2.3]$$

where $C_{\alpha(hkl)}$ and $C_{\gamma(hkl)}$ are the constants for the particular reflections under consideration.

Assuming α and γ are the only phases present:

$$V_\alpha + V_\gamma = 1 \qquad [2.4]$$

$$V_\gamma = \frac{1}{P \times \frac{C_\gamma}{C_\alpha} + 1} \qquad [2.5]$$

Appendix 2 gives appropriate values of $C_{\alpha(hkl)}$ and $C_{\gamma(hkl)}$ and how they were obtained.

2.8.2 Pole figures

(111) pole figures were plotted using the (111) γ peak at $2\theta = 43.4^{o}$, employing a Philips PW 1078 texture camera and Cr K_α radiation. Pole figures were plotted for a number of laser alloyed samples.

2.8.3 Residual stress measurements

Residual stress measurements were made and are reported in Chapter 4.

2.9 Erosion tests

Erosion tests were carried out and are reported in Chapter 5.

2.10 Carbon Analysis

To determine the carbon content of different areas within a single melt zone a laser-induced ion mass analyser (LIMA) was used. It has the ability to analyse very small discrete volumes of material, typically from 3μm to < 1μm in diameter and some tenths of a μm in depth[31]. A LIMA combines a pulsed, microfocussed laser-beam with a time-of-flight mass spectrometer. A short pulse of laser radiation, provided by a Q-switched Nd:YAG laser, is focussed onto the samples. The very high power-density in the focussed spot causes evaporation of a small volume of material. Analysis of this material is effected by measuring the mass-to-charge ratio of the ions extracted from the microplasma by time-of-flight mass spectrometry. Output data is received as a plot of relative ion current against atomic mass. Figure 2.3 shows a typical plot. This data is converted into relative wt % as follows:

It is known that the composition of the unalloyed material is approximately:

Cr 12.7 wt % - 13.3 At%
C 0.2 wt % - 0.9 At %
Fe 87.1 wt % - 85.8 At %

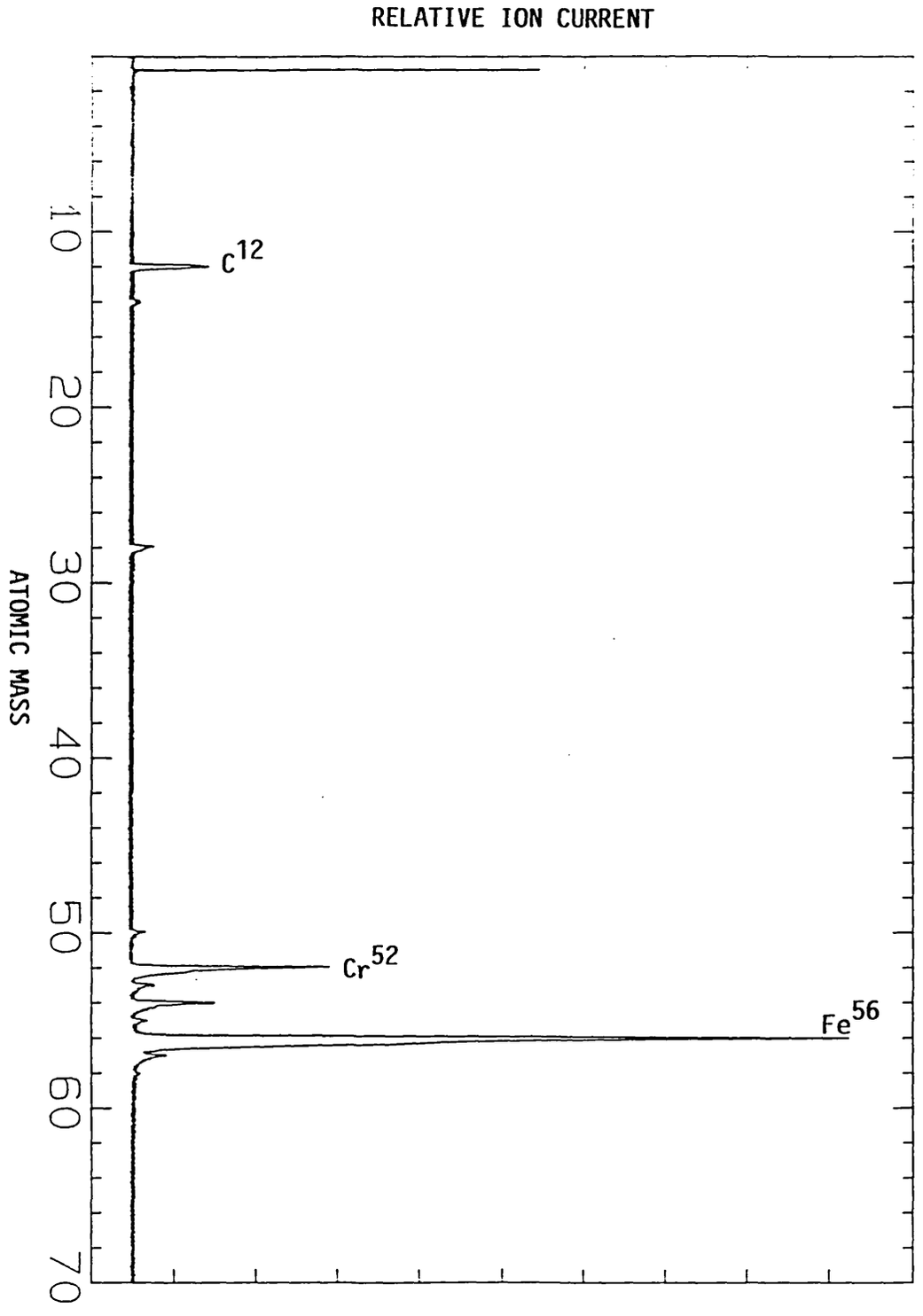


FIGURE 2.3

Typical plot from LIMA apparatus

The integrated areas of the relative ion currents due to carbon (12) and chromium (52) are calculated and expressed as a percentage of the sum of the two areas. This gives the Raw Isotope Yield (RIY) . These values have to be corrected to account for isotope compositions, C^{12} = 98.89% and Cr^{52} = 83.76%. These corrected values were ratioed C/Cr to give the Corrected Isotope Ratio (CIR) . These ratios were converted to atomic percent by multiplying the CIR values by the known atomic percentage of carbon in the parent metal, assuming that:

i) the steel was composed of only Cr, C and Fe
and
ii) the Cr/Fe ratio was constant throughout the material

Initially, an unalloyed area of parent material was analysed, to provide a standard, both for a comparison and to provide a correction to the relative sensitivity of the instrument. Whenever gathering data, the laser was triggered a number of times before recording the data, to eliminate any surface contamination, and an average of at least ten individual areas adjacent to one another was taken. The value of At%C obtained from the LIMA was 2.25 ± 0.68 At%C. It is known that At%C in the parent material is 0.9 At%. Thus the correction factor for the relative sensitivity of the machine is:

$$E_{C/Cr} = 0.9/2.25 = 0.4$$

Having obtained the correction factor, all the corrected isotope ratios obtained in the laser alloyed zones were multiplied by $E_{C/Cr}$ before conversion to atomic percentages.

CHAPTER 3

STRUCTURAL FEATURES OF LASER SURFACE ALLOYING 420 STEEL WITH CARBON

3.1 Introduction

Laser surface alloying with carbon offers the possibility of forming a martensitic layer of greater hardness than those produced by conventional hardening methods, laser transformation hardening or laser surface melting on a tempered substrate. High hardnesses are associated with good erosion resistance (see Chapter 5) and if the hardness of this martensitic layer can be raised whilst remaining crack free and well bonded to the substrate a substantial increase in erosion resistance is expected.

In this chapter the structural features, surface roughness, hardness and integrity of the melt zones are examined. Retained austenite measurements were made on specimens with partially overlapping tracks.

The most common method used for alloying a flat steel specimen with carbon is to coat the specimen with Dag graphite diluted with a binder, or for thicker coatings with a slurry in which the Dag is less diluted, Walker[32]; though some workers have used an atmosphere of acetylene or CO_2, Mordike et al[33]. The former method has several disadvantages. Results obtained by Walker suggest that at critical traverse speeds the binder used in the Dag is evaporated and the combination of gas flow from the laser nozzle and shroud blows the remaining carbon away from the molten pool, leading to less carbon absorption. Other problems associated with coating the surface with Dag, in both diluted and slurry form, are the difficulties in

producing coatings of standard and uniform thicknesses.

A more suitable and controllable means of applying a coating would be to spray the carbon in a binder in a similar manner to spray painting. In this way standard coatings of uniform thicknesses can easily be produced. A commercial product in aerosol form which incorporated an organic binder was used after preliminary tests had shown it to be suitable.

There are three fundamental ways in which the quantity of carbon introduced into the molten pool can be varied. There are:

i) by keeping the carbon coating uniform and varying the size of the molten pool by altering the laser parameters;

ii) by keeping the size of the molten pool constant and varying the mass of the carbon coating;

iii) by repeated cycles of coating and laser alloying a track.

3.2 Experimental

The size of the molten pool can be varied by altering either the interaction time (traverse rate/beam diameter) or the power density (beam power/diameter). After preliminary results had been obtained the power density was kept constant but the interaction time was varied by altering the traverse rate.

3.2.1 Single tracks

To observe the combined effects of (i) and (ii) above, single tracks were produced under a 1.6kW, 2.0 mm beam with carbon coatings of different thicknesses at speeds of traverse between 10 and 400 mms^{-1}. Three series of experiments were carried out, as shown below. Series (II) was designed on the basis of the results from Series (I). Series (III) was designed on the basis of results from Series (I) and (II).

Series (I): Carbon coatings varying from 14.5 x 10^{-6} gmm^{-2} to 97.1 x 10^{-6} gmm^{-2} and speeds of traverse between 10 and 400 mms^{-1} were used.

Series (II): Carbon coatings varying from 0 to 4.8 x 10^{-6} gmm^{-2} and speeds of traverse between 10 and 66 mms^{-1} were used.

Series (III): A fixed speed of traverse of 10 mms^{-1} and carbon coatings varying from 0 to 153 x 10^{-6} gmm^{-2} were used.

The mass of the carbon coatings was obtained by measuring the mass of the specimens to the nearest 0.1 mg, using a pair of chemical balances, before and after the application of the carbon coating. The difference between the two values was then divided by the surface area of the specimen to give a value expressed in gmm^{-2}.

To observed the effects of (iii) above, a series of runs, Series (IV) was carried out using a 1.6kW, 2.0mm beam at 10mms^{-1}. Alloyed tracks were produced, the carbon was re-applied and the areas re-treated. In this way a series of single tracks was produced which had been treated up to 16 times. The mass of each carbon coating was not known.

It is not possible to calculate the carbon contents of the melted zones from the mass of the carbon coatings and the volume of the melted zones, as carbon is lost during laser processing due to oxidation and vaporisation. The carbon contents of the melted zones were estimated from the microstructures displayed and the results of hardness testing.

Throughout the work unalloyed laser surface melted specimens were produced as a standard against which the alloyed structures could be compared.

3.2.2 Partially overlapping tracks

To cover the surface of an engineering component with a laser surface alloyed layer, it is likely that partially overlapping tracks will be required. Having found the optimum combination of laser processing parameters and mass of carbon coatings to maximise the hardness in a crack free track, a series of partially overlapping tracks was produced.

The processing parameters were a 1.6kW, 2.0mm beam and a traverse rate of $10 mms^{-1}$. Carbon coatings varied between 4 and 16 x 10^{-6} gmm^{-2}. The intertrack advances employed were 0.5, 1.0 and 1.5 mm corresponding to approximately 67, 33, and 1% overlap of the preceeding track respectively

3.3 Results

3.3.1 Series I - single cycle treatments

This series produced alloys with a range of carbon contents from ~0.8 to ~3.5 wt% C. Similar alloys were produced in Series II, III, and IV and the microstructural

features and hardness profiles of these series will be discussed later.

Series I will be used to illustrate the dimensions of the melt zone at different traverse rates as well as the structure of the laser melted parent material at these different rates.

Figure 3.1 shows the dimensions of the melt zone against traverse rate for single cycle treatments with a uniform carbon coating of 91×10^{-6} gmm^{-2}. The traverse rates varied from 10 to 400 mms^{-1}. Within the accuracy of the experiment no differences were noted due to different thicknesses of carbon coating, however, minor variations were observed from parallel experiments carried out at different times, due to minor variations in laser parameters.

It can be seen that the depth of the melt zone decreases more rapidly than the width as the traverse rate is increased.

This result is important as it shows that the carbon concentration, in the melted zone, increases as a result of the increase in the surface area/volume ratio with increasing traverse rate. This occurs because the amount of material introduced into the molten pool per unit length is dependent upon the surface area, which is proportional to the width whereas, the volume of the molten pool into which this extra material is alloyed is dependent upon the cross-sectional area which is proportional to the depth as well as the width. Most tracks produced in this work were of the conduction-limited type and no keyholing was observed. At higher traverse rates > 100mms^{-1} the depth of the melt tracks was influenced by the power distribution across the laser beam. Virtually no melting occurred at speeds in excess

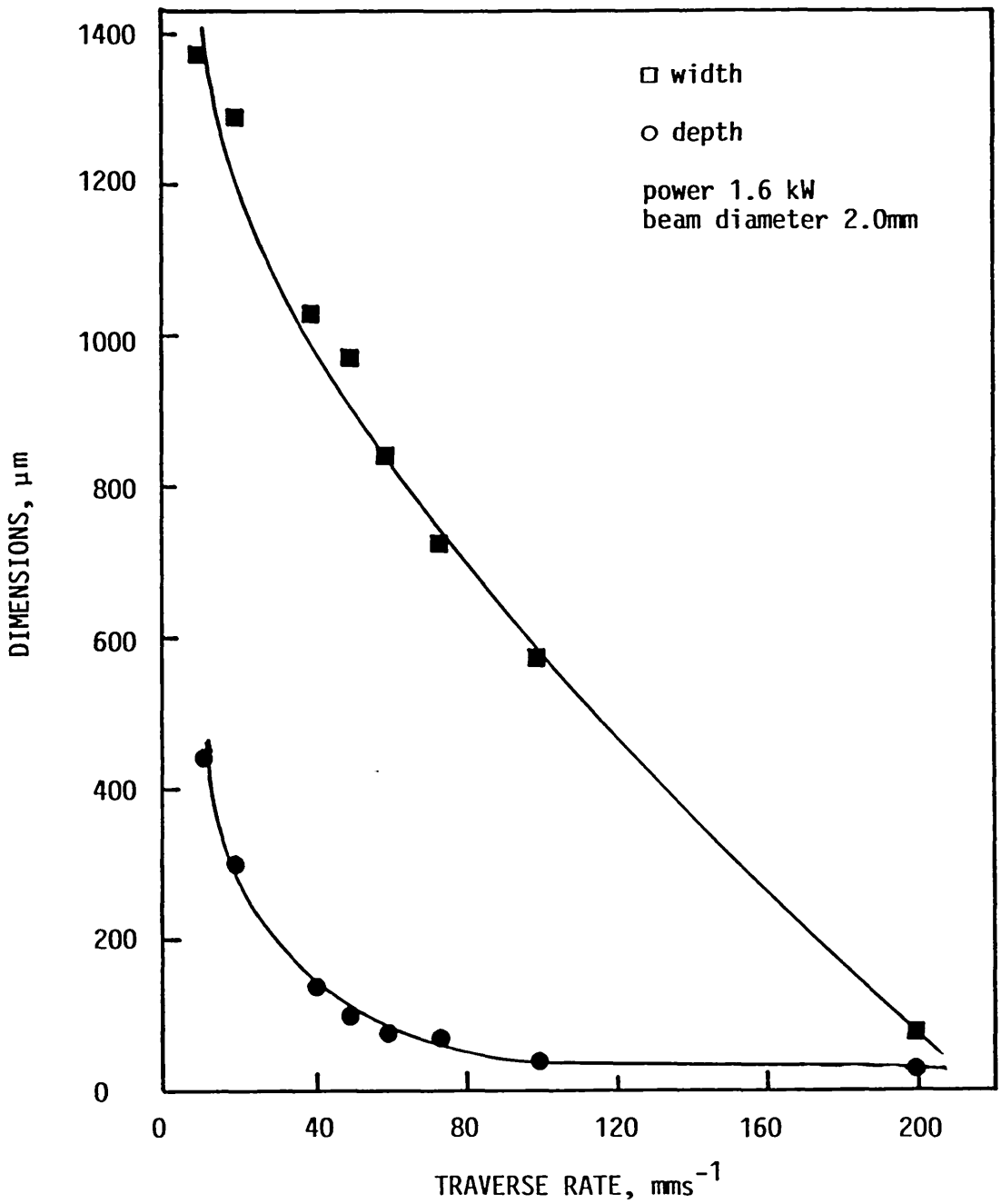


FIGURE 3.1

Dimensions of melt zone against traverse rate

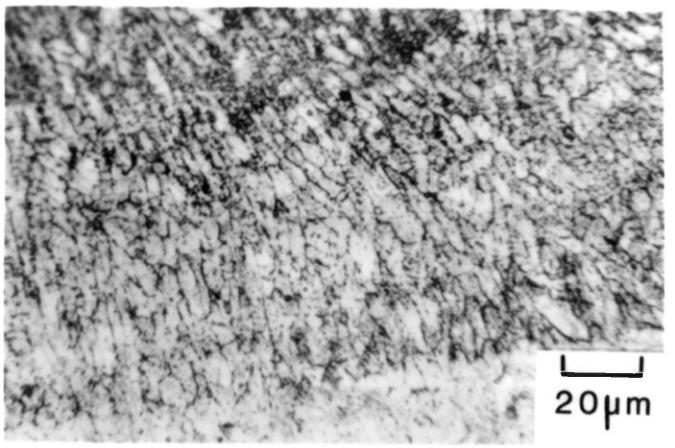
of 200mms^{-1}.

When no carbon coating was applied, light etching (< 60 secs) of the laser melted parent material showed the structure consisted of cells separated by a thin dark etching region. Photograph 3.1. Cell spacings were of the order 3μm for specimens processed at 10mms^{-1} whilst those processed at 200mms^{-1} displayed cell spacings of about 0.6 μm, indicating cooling rates of between ~1 x 10^3 and 6 x 10^4 Ks^{-1} respectively[34].

On deeper etching (up to 600 secs), the martensitic nature of the structure became apparent, confirming work by Lamb[5]. The hardness of the laser melted parent material was typically ~600 Hv. There is a heat affected zone interpreted as consisting of martensite (~600 Hv): the area of the HAZ adjoining the melt zone is lighter etching than the remainder of the zone and partial melting may have occurred in this region. Growth of cells occurs from this region into the melt, Photograph 3.1.

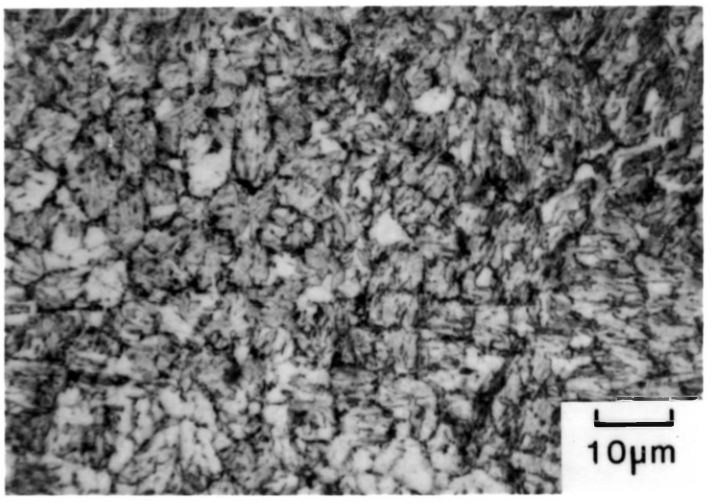
3.3.2 Series II

When a very thin carbon coating (up to 4.8 x 10^{-6} gmm^{-2}) is applied before laser processing at 10 mms^{-1}, the etched structure is similar to that of the unalloyed structure showing fine cells of a martensitic nature as shown in photograph 3.2. Photograph 3.3 shows martensite at a higher magnification. The hardness of these structures increased from 600 Hv to ~800 Hv increasing with the amount of carbon alloyed. The structures of the melt zones were homogeneous for all tracks processed at speeds up to 20 mms^{-1}. However, for specimens with carbon coatings > 0.6 x 10^{-6} gmm^{-2} processed at 40 mms^{-1} and above and for specimens with carbon coatings > 0.5 x 10^{-6} gmm^{-2} processed at 50 mms^{-1}



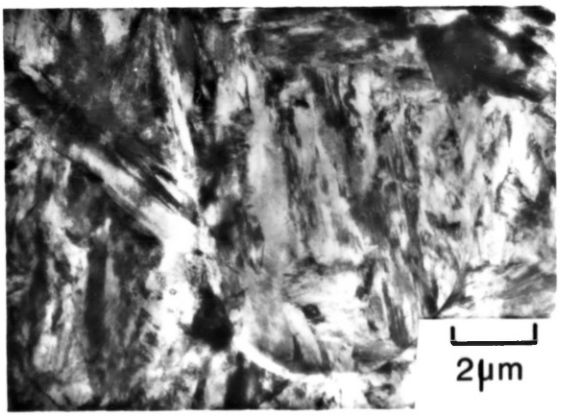
PHOTOGRAPH 3.1

Traverse section through laser melted parent material (P=1.6kW, D=2.0mm and V=10mms^{-1}).



PHOTOGRAPH 3.2

Traverse section through laser alloyed zone. (P=1.6kW, D=2.0mm, V=10mms^{-1} and carbon coating = 4.8x10^{-6} gmm^{-2})



PHOTOGRAPH 3.3

TEI of alloyed zone. (P=1.6kW, D=2.0mm, V=10 mms^{-1} and carbon coating = 4.8 x 10^{-6} gmm^{-2})

and above, the structures were not homogeneous throughout the melt zone. Light and dark etching regions were observed indicative of convective flow effects in the liquid state; Draper[16] has reviewed work on such flow effects. These effects were also noted in the more heavily alloyed specimens of Series I at speeds of traverse as low as $20mms^{-1}$. Photograph 3.4 shows a secondary electron image of such a region from a transverse section and photograph 3.5 shows an optical image of such a region from a longitudinal section at 90^{o} to the surface. The light etching regions were observed to have hardness values of ~700-800 Hv, about 200-300 Hv greater than the remainder of the structure. Otherwise the hardness values did not vary significantly through the melted zone.

Figure 3.2 shows a plot of hardness against depth for a specimen alloyed with a carbon coating of 4.8×10^{-6} gmm^{-2} at 10 mms^{-1}. The hardness is constant throughout the melted zone and decreases through the HAZ with distance. Photograph 3.6 shows the corresponding melt zone and hardness indentations.

To determine whether there was a compositional, as well as a structural difference, between the light and dark etching regions LIMA (Laser-induced Ion Mass Analyser) apparatus was used to determine the carbon contents of these regions and also to check the carbon contents of some homogeneous melt zones produced at slower traverse rates. The results are shown in Table 3.1 and are based on the average of 10 values; the error stated is the standard error of the 10 results ($\sigma/\sqrt{10}$). The results reveal that the light etching regions had a carbon content up to 0.6 wt% C and the dark etching regions had a carbon content of between 0.9 and 3.0 wt% C. These results together with the observation that convective flow

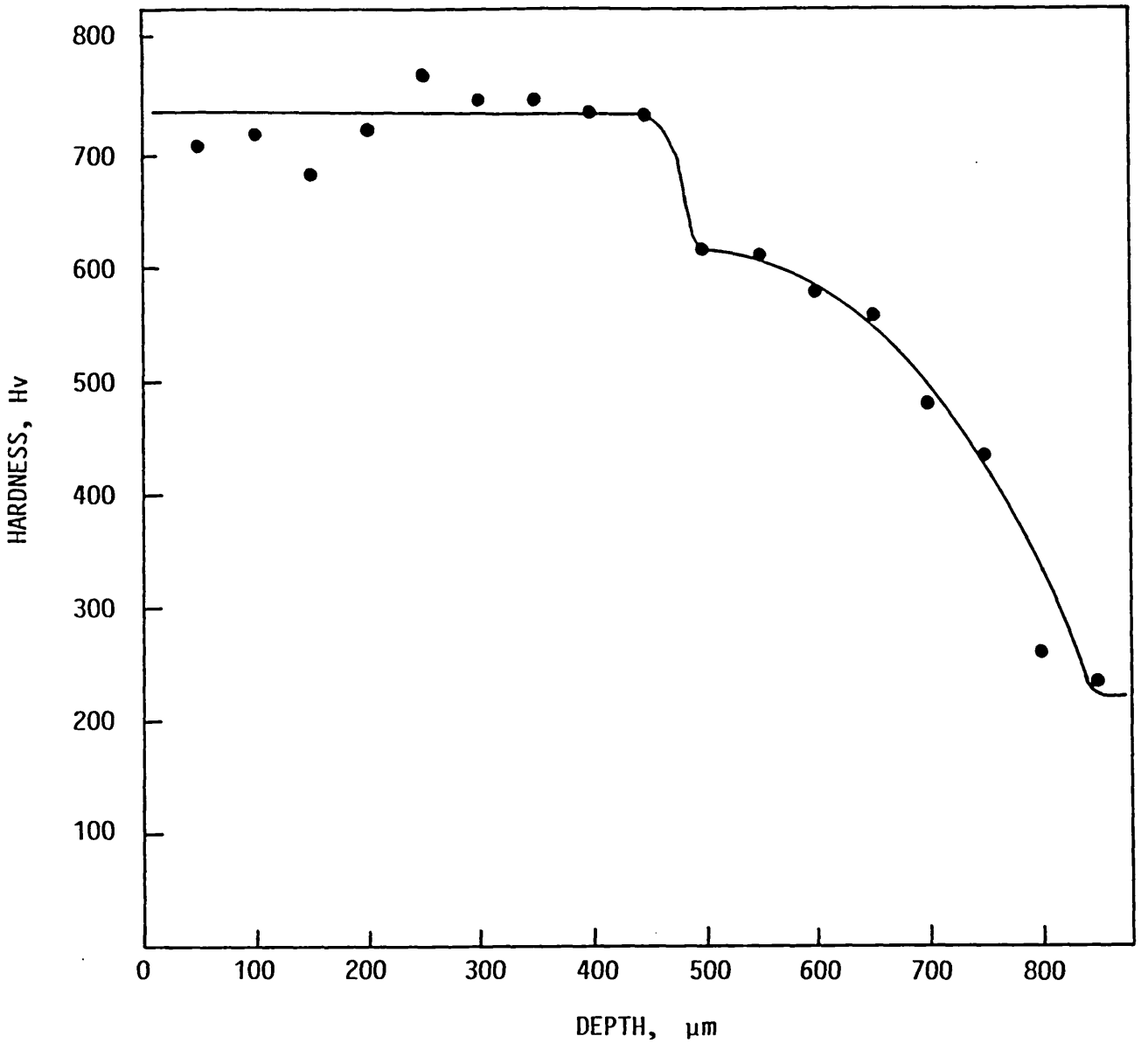
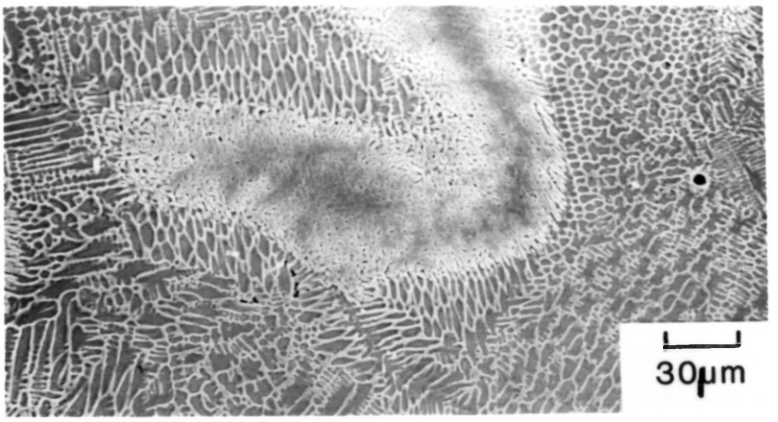


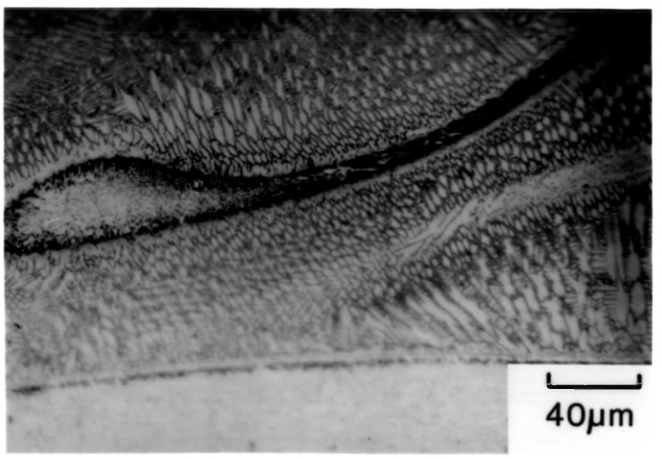
FIGURE 3.2

Hardness against depth,
for an alloyed specimen processed at $10mms^{-1}$
under a 1.6 kW, 2.0mm beam with a
carbon coating of 4.8×10^{-6} gmm^{-2}



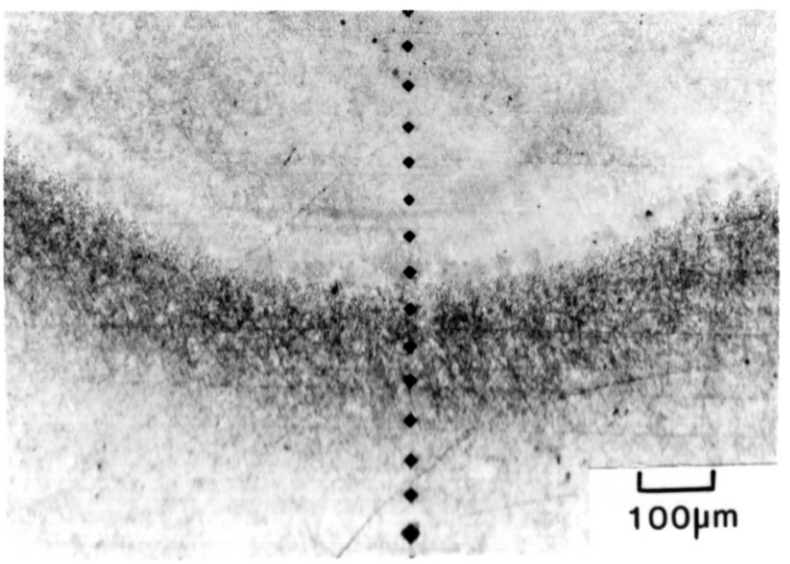
PHOTOGRAPH 3.4

SEI of transverse section through laser alloyed zone ($P=1.6kW$, $D=2.0mm$, $V=20mms^{-1}$ and carbon coating = 57.5×10^{-6} gmm^{-2})



PHOTOGRAPH 3.5

Longitudinal section of laser alloyed zone at 90° to the surface ($P=1.6kW$, $D=2.0mm$, $V=20mms^{-1}$ and carbon coating = 80.2×10^{-6} gmm^{-2})



PHOTOGRAPH 3.6

Transverse section through laser alloyed zone, with hardness indendations corresponding to Figure 3.2. ($P=1.6kW$, $D=2.0mm$, $V=10mms^{-1}$ and carbon coating = 4.8×10^{-6} gmm^{-2})

Mass of carbon coating gmm^{-2}	Speed of traverse mms^{-1}	Type of area	wt% C
4.8×10^{-6}	10	Homogeneous	0.51 ± 0.12
4.8×10^{-6}	10	Homogeneous	0.50 ± 0.09
4.8×10^{-6}	40	Inhomogeneous light etching	0.25 ± 0.04
4.8×10^{-6}	40	Inhomogeneous Dark etching	0.94 ± 0.15
4.8×10^{-6}	66	Inhomogeneous Light etching	0.63 ± 0.10
4.8×10^{-6}	66	Inhomogeneous Dark etching	3.00 ± 0.53

TABLE 3.1

effects were observed at lower speeds of transverse for heavier carbon coatings indicate that there is a finite time required for diffusion and convective flow, both in the liquid state, to evenly distribute the additional alloying element throughout the melted zone. Photograph 3.7 shows the discrete areas from which the material was ionised and the "damage" caused. The lower concentration of carbon in the light etching regions enabled the martensitic transformation to occur whereas, the high concentrations of carbon in the remainder of the melt zone prohibited the formation of martensite due to its effect of lowering the Ms temperature (see section 3.4.3).

3.3.3 Series III

The structures produced when alloying with coatings between 0 and 10 x 10^{-6} gmm^{-2} at 10mms^{-1} were very similar to those produced in Series II at the same traverse speed. In Series II the maximum carbon coating was 4.8 x 10^{-6} gmm^{-2} and the maximum hardness achieved ~800 Hv. The carbon content of these structures was estimated to be up to ~0.6 wt% C. For specimens processed with carbon coatings between 4.8 and 10 x 10^{-6} gmm^{-2} the hardness of the melt zones increased from ~800 Hv to over 900 Hv. No retained austenite was detected in any of the samples by light microscopy but the problems associated with etching the 420 steel and the fine scale of the structure should be borne in mind. The carbon content of these structures was estimated to be no more than 0.6 wt% C.

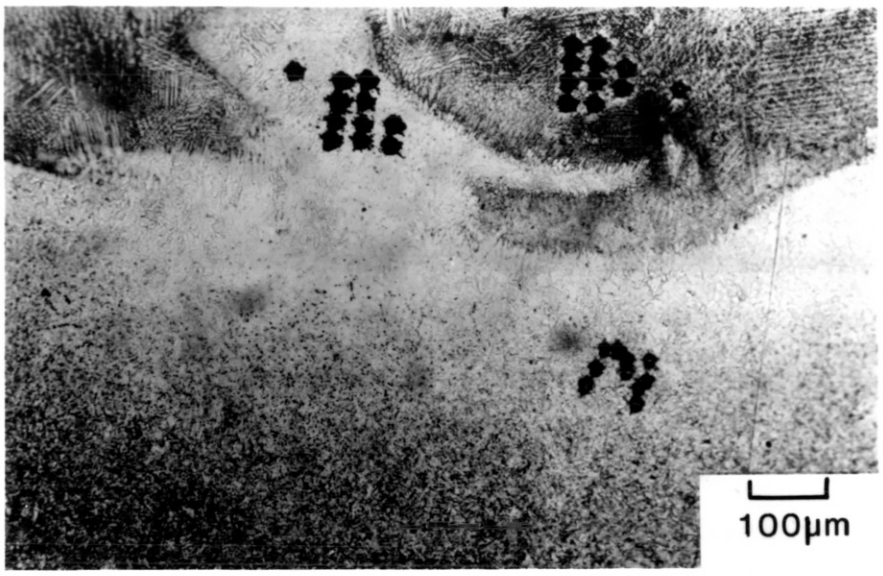
As the mass of the carbon coatings was increased from 10 to 50 x 10^{-6} gmm^{-2} the etched structures which had displayed a cellular/dendritic nature became increasingly dendritic. The hardness of the melted zone decreased as the mass of the carbon coatings increased, until the alloy produced by alloying with a carbon coating

of 50 x 10^{-6} gmm^{-2}, had a hardness of only ~500 Hv. The structure was fully dendritic, Photograph 3.8, with thin dark regions between the dendrites, shown by TEM, to be very fine eutectic with interlamella spacings of ~0.1μm, Photograph 3.9.

On increasing the mass of the carbon coatings from 50 to 150 x 10^{-6} gmm^{-2}, the structure initially consisted of austenite dendrites with a very small proportion of interdendritic eutectic, Photograph 3.8; however, with increasing amounts of carbon alloyed the proportion of interdendritic eutectic grows, Photograph 3.10 until the structure is fully eutectic Photograph 3.11.

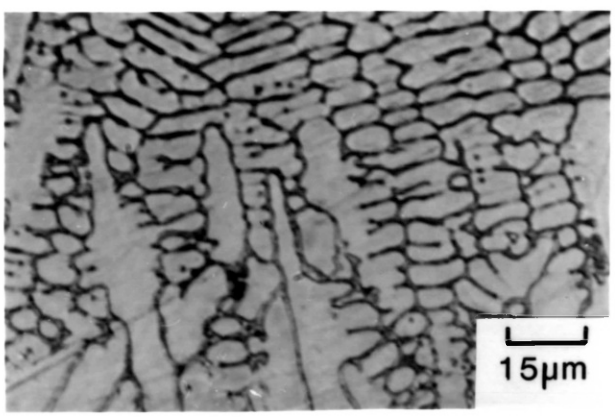
Dendrites grow anti-parallel to the direction of maximum heat flow. Photograph 3.12 is a longitudinal section at 90^{o} to the surface showing dendritic alignment, the laser passed from right to left. Photograph 3.13 shows the alignment of dendrites at the surface of the track. The dendrites grow from the edges towards and then along the middle of the melt zone. The carbon content of these melt zones was estimated to be ~0.9 wt% C for the fully dendritic structures and up to ~3.5 wt% C for the fully eutectic structures. The hardnesses of these structures varied between 500 and 1200 Hv; increasing with the amount of carbon alloyed. Two different types of area between the HAZ and melted zone were observed; the first being similar to the light etching region mentioned earlier and shown in Photograph 3.1. The second was a narrow featureless band, typically ~3-12μm in extent, interpreted as austenite, suggestive of planar solidification from which cells or dendrites developed, as shown in Photograph 3.10.

Figure 3.3 shows the average hardness of the melt zone plotted against mass of carbon coating. It can be



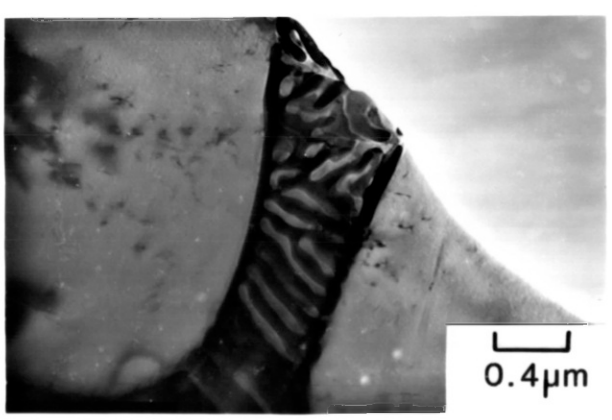
PHOTOGRAPH 3.7

Transverse section through laser alloyed zone, showing discrete areas of damage caused by the LIMA apparatus (P=1.6kW, D=2.0mm, V=40mms^{-1} and carbon coating = 4.8 x 10^{-6} gmm^{-2})



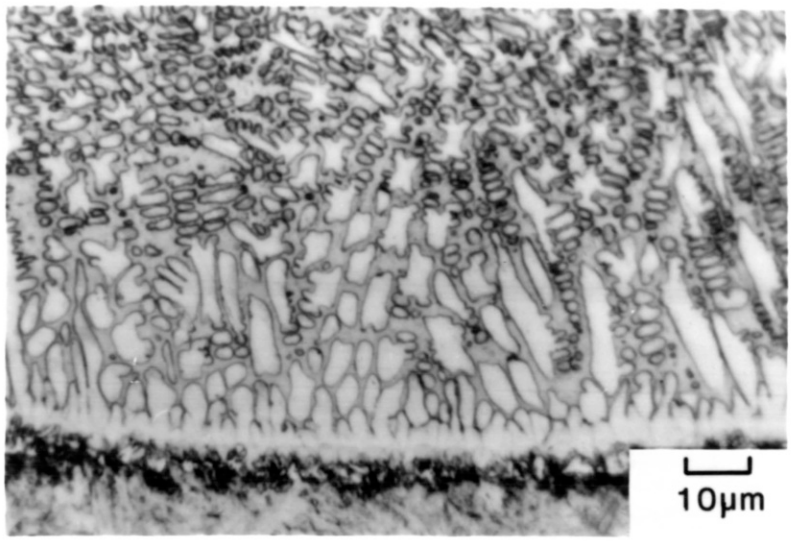
PHOTOGRAPH 3.8

Transverse section through laser alloyed zone. (P=1.6kW, D=2.0mm, V=10mms^{-1} and carbon coating = 45 x 10^{-6} gmm^{-2})



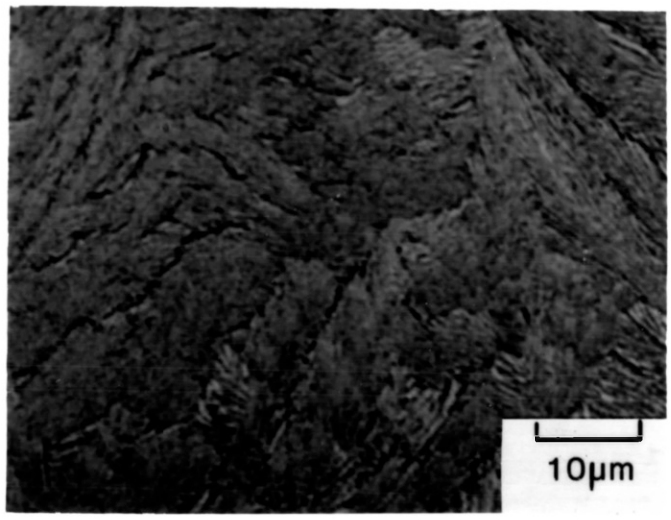
PHOTOGRAPH 3.9

TEI of eutectic between dendrites (P=1.6kW, D=2.0mm, V=10mms^{-1} and carbon coating = 45 x 10^{-6}gmm^{-2})



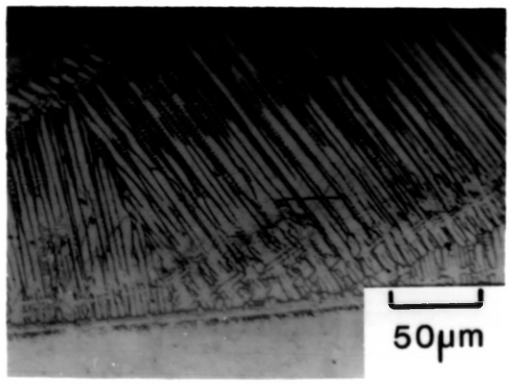
PHOTOGRAPH 3.10

Transverse section through laser alloyed zone with planar solidification front (P=1.6kW, D=2.0mm, V=10mms^{-1} and carbon coating 100 x 10^{-6} gmm^{-2})



PHOTOGRAPH 3.11

Transverse section through laser alloyed zone. (P=1.6kW, D=2.0mm, V=10mms^{-1} and carbon coating = 127 x 10^{-6} gmm^{-2})



PHOTOGRAPH 3.12

Longitudinal section of laser alloyed zone at 90° to the surface. (P=1.6kW, D=2.0mm, V=10mms^{-1} and carbon coating = 80.2 x 10^{-6} gmm^{-2})

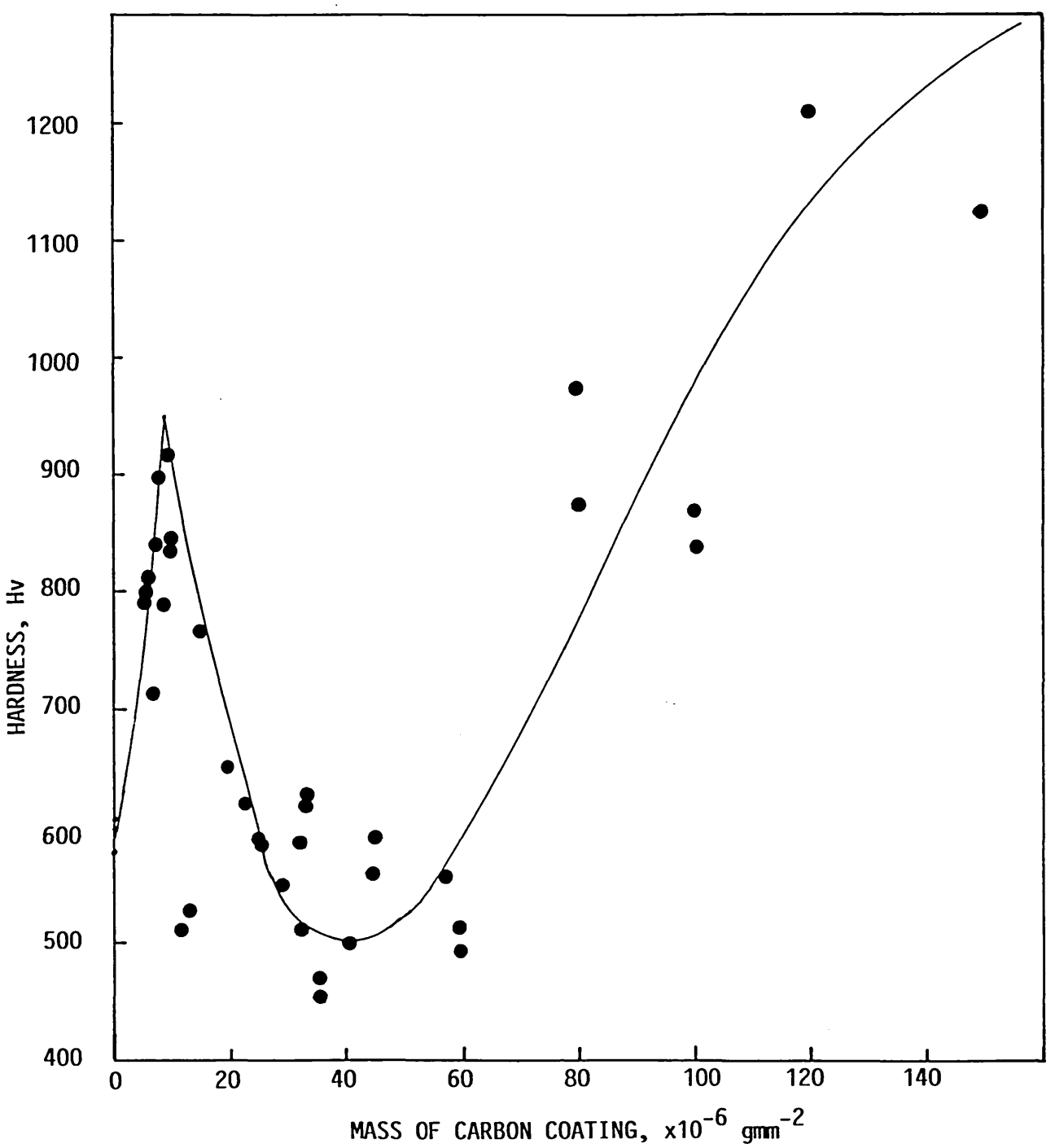


FIGURE 3.3

Hardness against mass of carbon coating

seen that the hardness increases rapidly to a maximum of over 900 Hv before falling equally rapidly to a minimum of ~500 Hv, after which the hardness rises steadily with increasing mass of carbon coating.

3.3.4 Series IV - Multicycle treatments

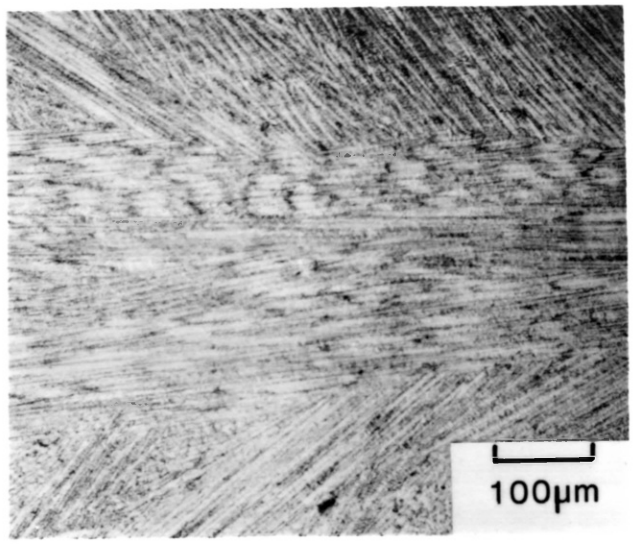
The multicycle laser treatments produced high carbon structures ranging from hypo-eutectic to hyper-eutectic. The mass of each individual carbon coating was not known and therefore the results are not as quantitative as those above.

In the specimens treated between 1 and 2 cycles the structures were cellular and similar to those reported eariler in Series II. As the number of cycles increased the structures became dendritic, the quantity of interdendritic material increased until after 4 cycles the structures were predominantly eutectic with some austenite dendrites, as described in Series III.

After 7 or more cycles the structures were hyper-eutectic, Photographs 3.14, (a) and (b) consisting of carbides and eutectic. These structures suffered from cracking and porosity, the extent of porosity increasing with successive treatment above 7 cycles.

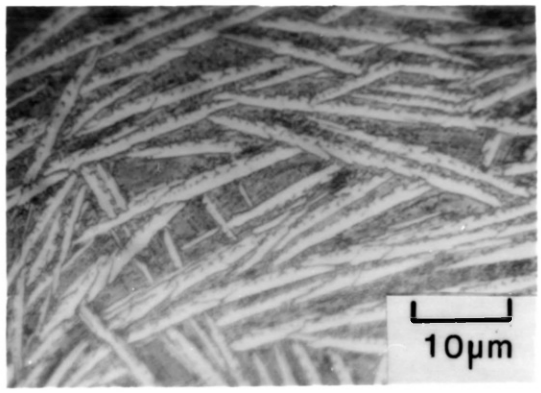
Heat affected zones with both the light etching and planar features were observed; the planar tended to be observed in the specimens which displayed a dendritic structure.

Figure 3.4 shows average hardness of the melt zone against number of treatment cycles. The hardness increased as the carbon content of the treated zones increased, from ~600 to 1400 Hv.



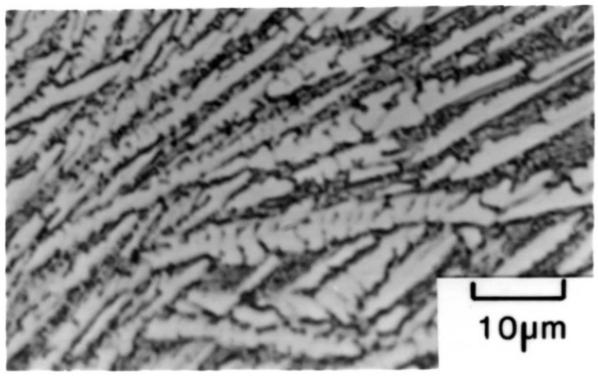
PHOTOGRAPH 3.13

Polished and etched top surface of alloyed zone. (P=1.6kW, D=2.0mm, V=10mms^{-1} and carbon coating = 129 x 10^{-6} gmm^{-2})



PHOTOGRAPH 3.14(a)

Transverse section through laser alloyed zone (P=1.6kW, D=2.0mm, V=10mms^{-1} Number of treatment cycles = 12)



PHOTOGRAPH 3.14(b)

Transverse section through laser alloyed zone (P=1.6kW, D=2.0mm, V=10mms^{-1} Number of treatment cycles = 16)

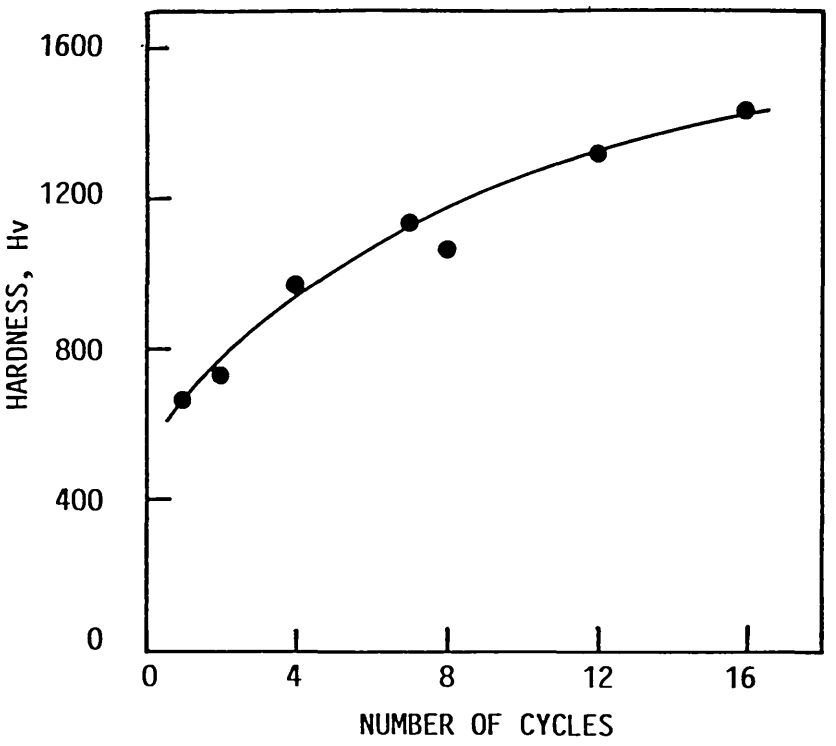


FIGURE 3.4

Average hardness against number of treatment cycles

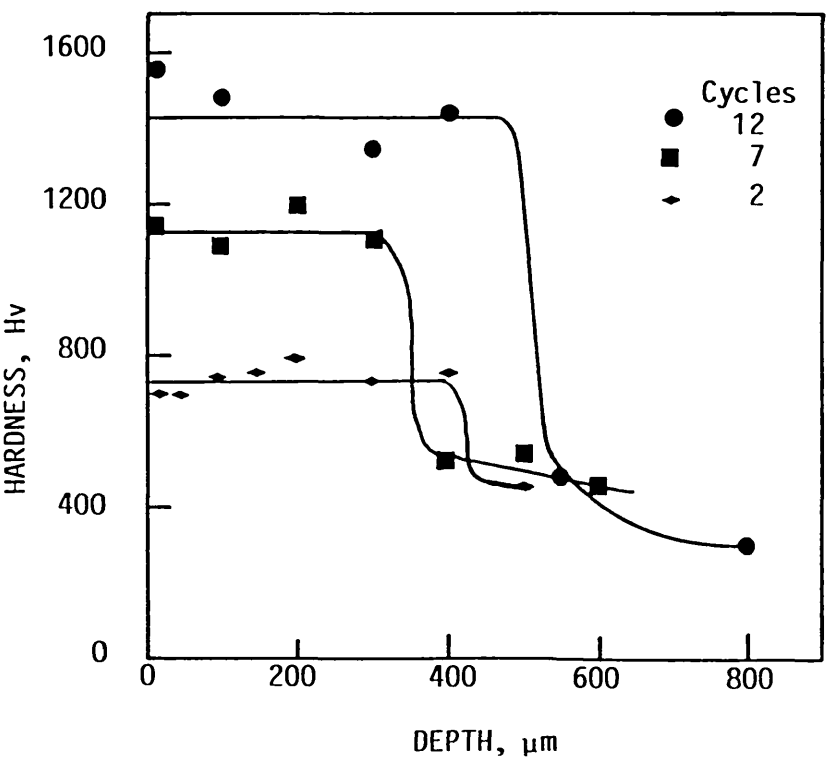


FIGURE 3.5

Hardness against depth for a selection of different numbers of treatment cycles

Figure 3.5 shows the hardness as a function of depth below the surface of the melt zone for a selection of different numbers of cycles. The microhardness values showed considerable scatter in the melt zone and no clear trend or variation with depth was detected.

The scatter of hardness values through the depth of a treated zone suggests a degree of heterogeneity. This could also be seen in the structures, due mainly to the melt pools created by successive laser cycles penetrating to different depths.

3.3.5 Partially overlapping tracks

The hardness and structures of the melt zones were similar to those described earlier in sections 3.3.2 and 3.3.3 for specimens produced under identical laser parameters using carbon coatings of similar thicknesses . The structures were homogeneous throughout the melt zones and the average hardness values of the specimens increased with increasing mass of the carbon coatings and varied between ~650Hv and ~900 Hv.

The results of retained austenite measurements (see section 2.8.1 for method used) taken from a number of specimens are shown in Appendix 3 and are represented graphically in Figure 3.6. There is a roughly linear relationship between the mass of the carbon coatings (4 to 16 x 10^{-6} gmm^{-2}) and the percentage of retained austenite (~10 to 46%). The value at the origin is for the parent material oil quenched after 1 hour at 960^{o}C. The degree of overlap did not appear to have any effect on the percentage of retained austenite. Pole figures indicated that there was no significant texture present as no intensity was greater than two times random.

On a number of specimens, after the initial retained austenite measurements were made material was removed from the surface by electropolishing and the retained austenite measurements repeated. The polishing was repeated and measurements taken at 50μm intervals until the parent material was reached. No significant variation in the austenite content was noted with depth.

3.3.4 Surface roughness

The surface roughness of single tracks varied slightly with processing speed. However, it varied to a greater extent with the percentage carbon introduced into the melt zone: the roughest tracks being those with the highest carbon contents. R_a values ranged from 0.7 to 7.0 μm (typically they lay between 0.7 and 5.0 μm) along single tracks and less than 1μm across them.

The R_a values obtained from overlapping tracks were between 0.7 and 5.0 μm along the tracks and varied between 2.0 and 5.0 μm across the overlapping tracks. There was no relation between roughness and degree of overlap.

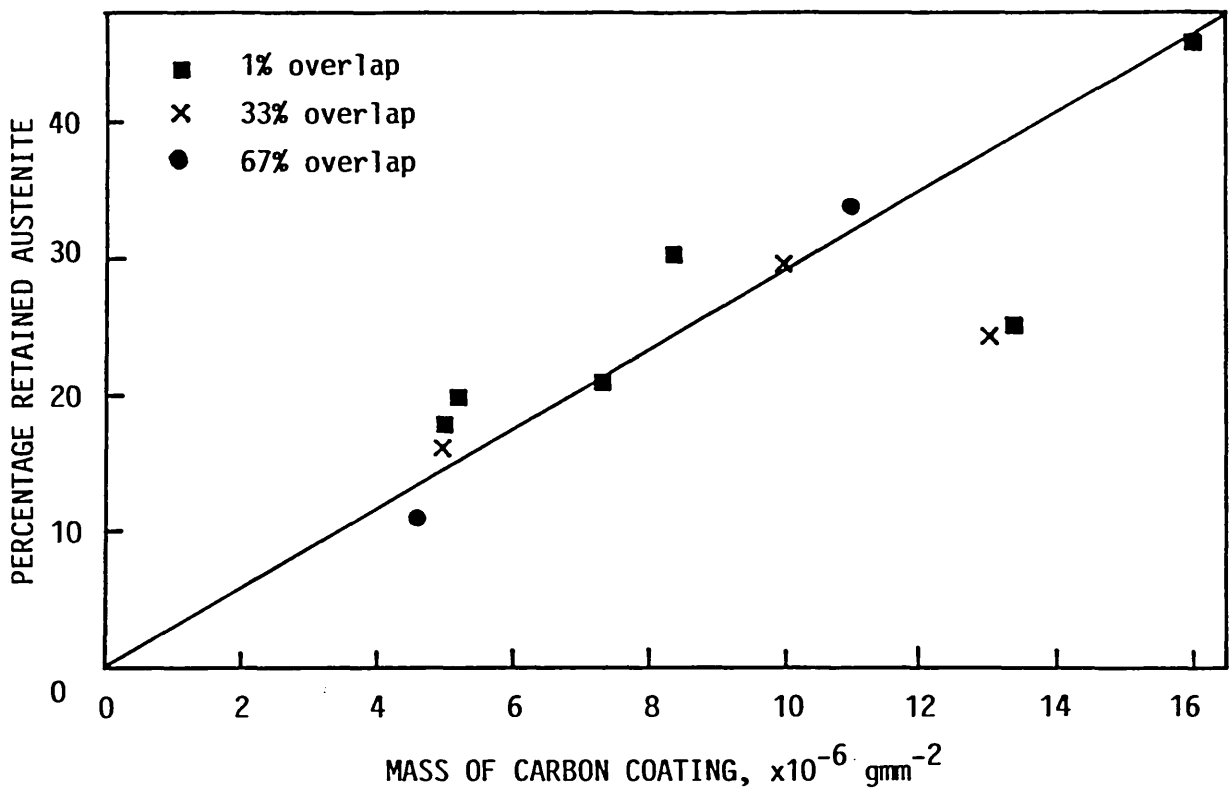


FIGURE 3.6

Percentage retained austenite against mass of carbon coating

3.4 Discussion

3.4.1 Solidification

Figure 3.7 shows a section through the Fe-Cr-C phase diagram at 13 wt% Cr after Bungart[35]. On solidification of the 420 stainless steel (~0.2 wt% C), the primary phase is α (B.C.C.); on cooling under equilibrium conditions in the solid state, α transforms to γ (F.C.C.) and the final structure at room temperature would consist of $\alpha + M_{23}C_6$. When the solid state cooling rate increases sufficiently γ will transform to martensite. As indicated in the results the phase constituting the cells has been identified as martensite, confirming work by Lamb[5]. The dark regions observed between the cells indicate the occurrence of C and Cr segregation during cooling, possibly involving a small amount of eutectic formation. EDS analysis across a number of solidification cells from different areas of a specimen of laser melted parent material confirms the segregation of Cr to the intercellular regions. Figure 3.8 shows the profile of Cr through a solidification cell. The Cr content is ~12 wt% throughout the cell, rising to between 23 and 29 wt% in the intercellular regions.

As the carbon content of the alloy is increased various phases form on solidification. The maximum equilibrium solid solubility of carbon in γ at 13 wt% Cr is ~ 0.8 wt%, Figure 3.7. For a carbon content of 1.0 wt% the phases expected to be present at the completion of solidification would be austenite dendrites and eutectic. The type of the carbide in the eutectic was not positively identified, but according to the phase diagram it should be M_7C_3.

Transformations subsequently occurring in the solid state would depend on the cooling rate, though at

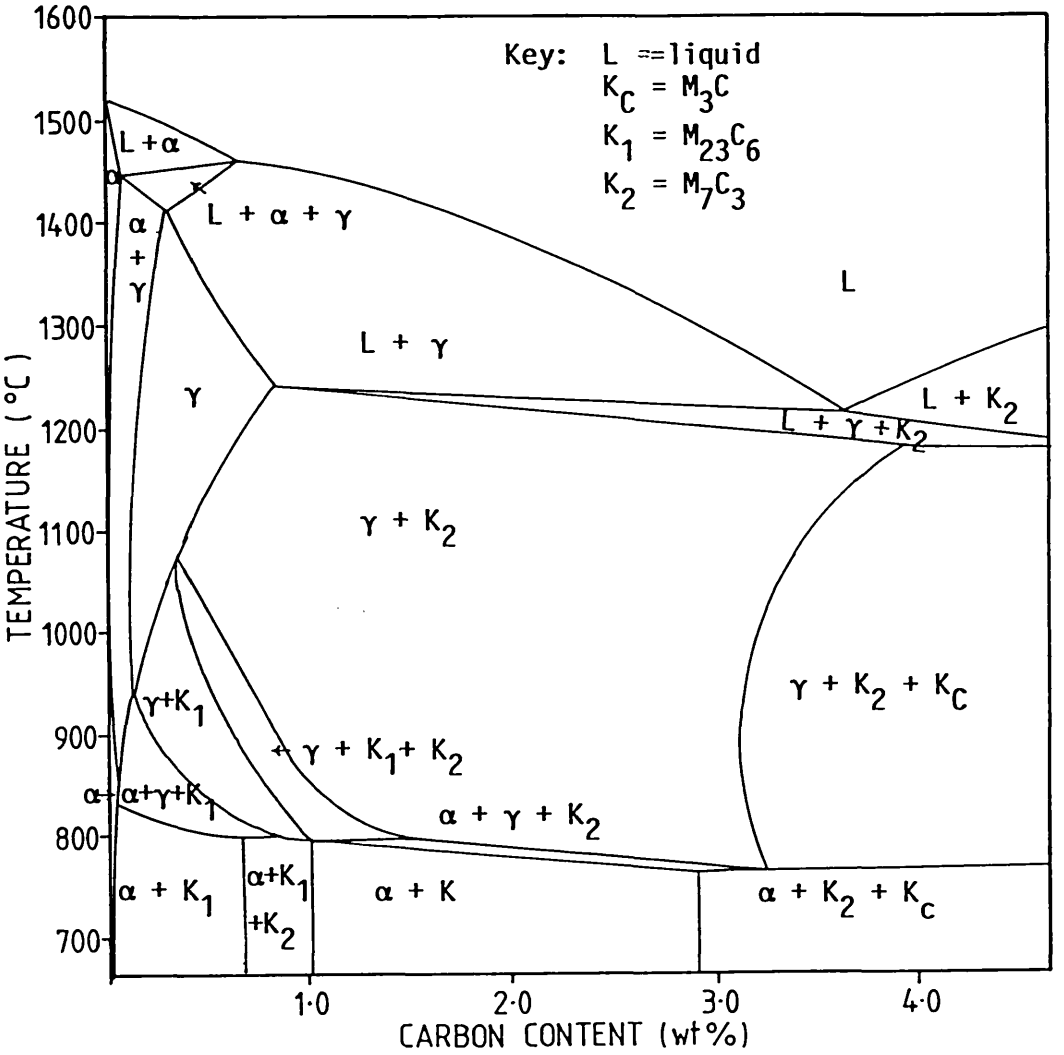


FIGURE 3.7

Section through the Cr-C-Fe phase diagram at 13 wt% Cr

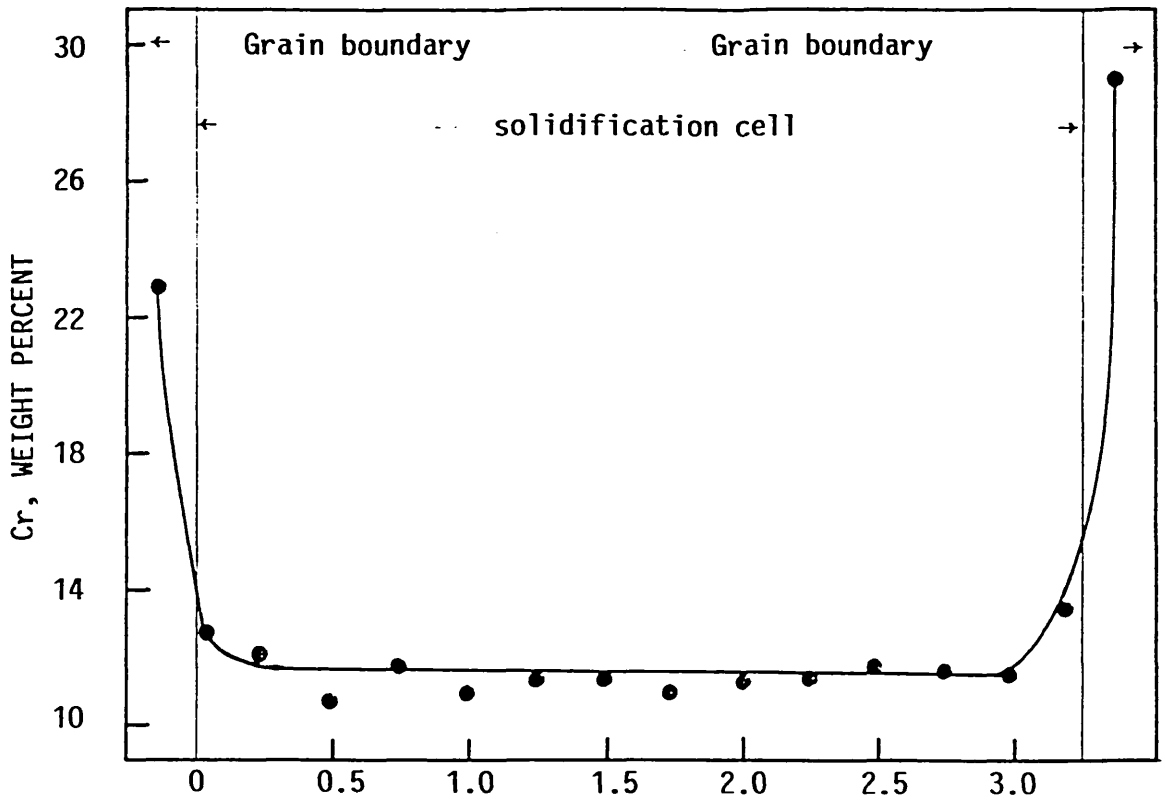


FIGURE 3.8
Compositional profile of Cr through a solidification cell, from a specimen of laser melted parent material. (P=1.6 kW, D=2.0mm, V=10mms^{-1})

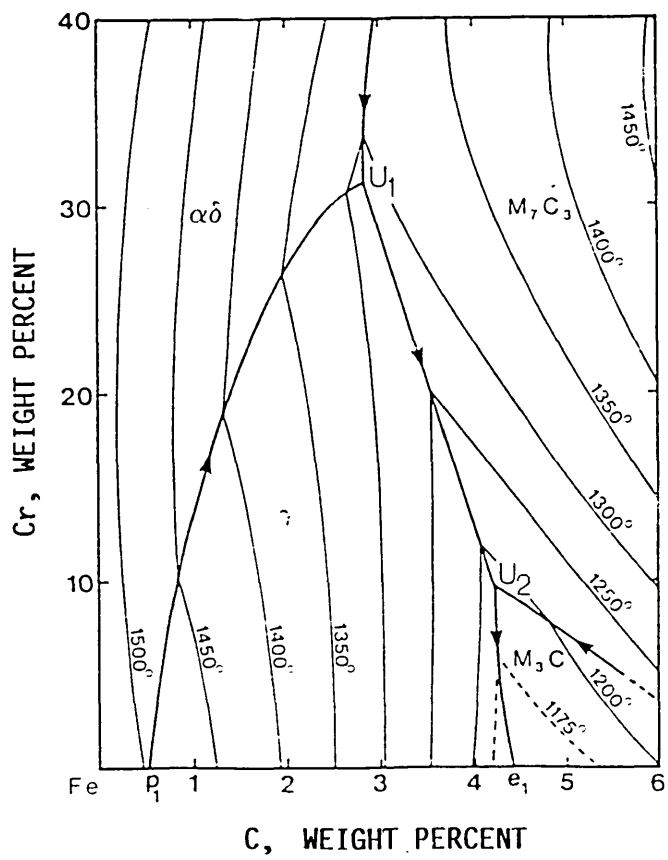


FIGURE 3.9

Fe rich corner of metastable C-Cr-Fe liquidus surface[36]

higher carbon contents, retention of austenite can occur at cooling rates likely to produce martensite due to the lowering of the M_s temperature caused by carbon, (see section 3.4.3). As the carbon content of the alloy progressively increases, the proportion of eutectic present on solidification would increase at the expense of the austenite dendrites, until at ~3.5 wt% C the solidification structure would be fully eutectic. Recent work by Thorpe et al[36], (Figure 3.9), indicates that the eutectic is nearer to ~4.0 wt% C in a 13 wt% Cr alloy. With the addition of yet more carbon the proportion of eutectic would be expected to decrease as primary carbide (M_7C_3) is formed, increasing in amount with increasing carbon content.

3.4.2 Solidification front morphologies

For a planar solidification front to be present, constitutional undercooling must not occur, and therefore

$$\frac{G}{R} \geq \frac{m C_o}{D} \frac{(1-k_o)}{k_o} \qquad [3.1]$$

where G = the temperature gradient in the liquid
R = the velocity of the solid/liquid interface
m = the slope of the liquidus
C_o = the initial solute concentration
D = the diffusivity of the solute in the liquid
k_o = the ratio of the solute concentration in the solid to solute concentration in the liquid.

At a G/R ratio lower than the minimum value for a

stable planar front a cellular morphology develops as a result of constitutional supercooling; still lower G/R ratios lead to dendritic growth.

The influence of G and R on solidification morphology is illustrated by data for an Al-0.1 wt% Cu alloy in Figure 3.10 after Cohen et al[38]. The trends may be taken to be typical.

Laser surface melting and alloying produce melted zones containing material that has solidified at varying G/R ratios[39]. Extremely high values of G/R occur at the bottoms and sides of the melt zones, where the rates of solidification are low, whilst lower values of G/R occur at the tops and centres of the melt zones where the rates of solidification are high.

The reasons for the extremely high values of G/R which occur at the bottoms and sides of the melt zones is that after the laser has passed there will be an instant where melting is no longer taking place but freezing has not yet started. At this point R is zero and therefore G/R is infinite, thus explaining the presence of the featureless ring of austenite often observed between the HAZ and melted zones, after which the G/R ratio decreased and cellular or dendritic solidification occurred. The ring of austenite tended to occur in those specimens whose melt zones had a carbon content greater than ~0.8 wt% C and therefore no solid state transformations occur. (See section 3.4.3). However, in those specimens where the carbon content of the melt zone was less than ~ 0.8 wt% C the area between the HAZ and melt zone consisted of the light etching material; the detail of this could not be elucidated due to solid state transformations occurring, which obscured any original features which may have been present. It is likely that there is a thin band of

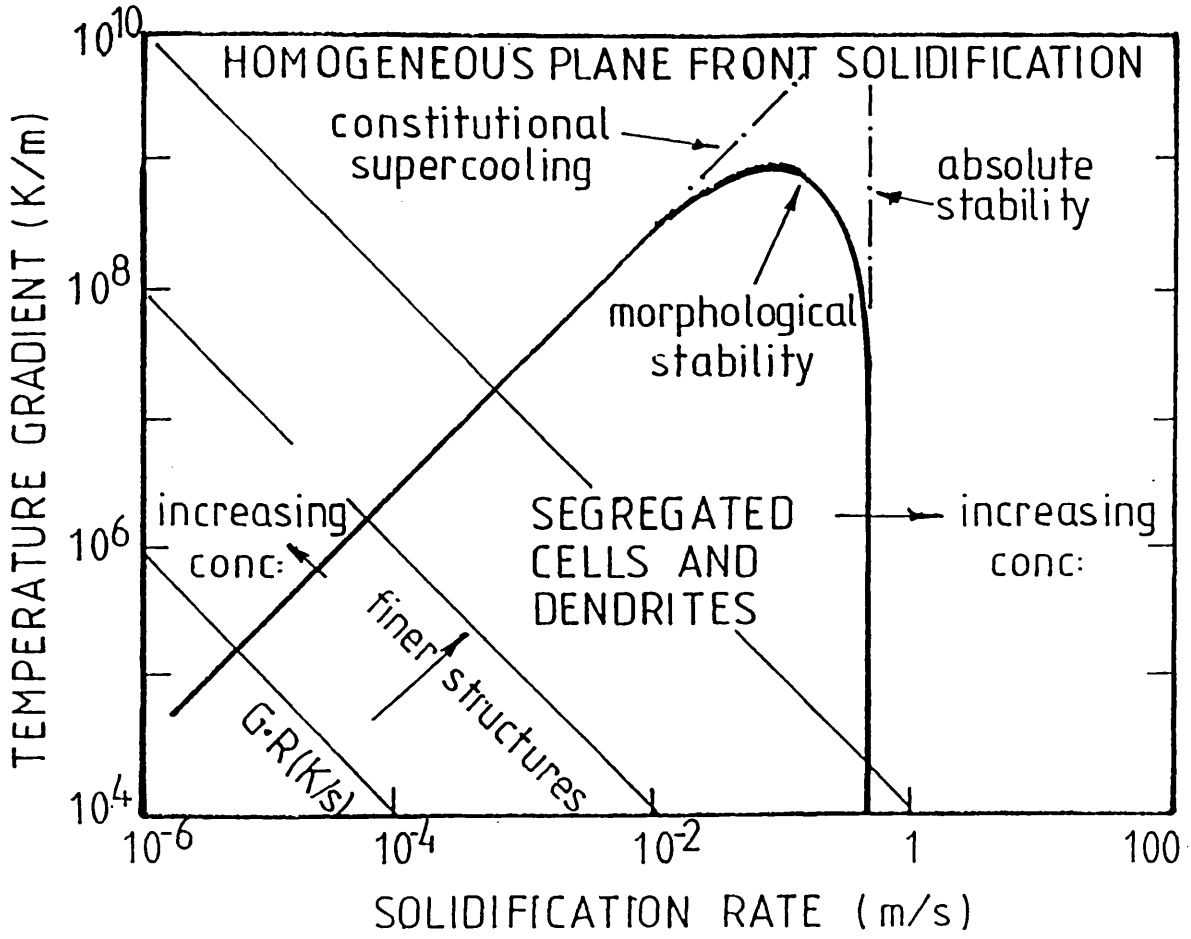


FIGURE 3.10

The influence of temperature gradient and solidification rate on solidification morphology for an Al-0.1 wt% Cu alloy[38]

material created by planar solidification present in these specimens, as the only component of equation 3.1 that changes on increasing the carbon content for identical laser parameters is the initial solute concentration, C_o. As C_o increases, with all other things being equal, the probability of a planar solidification front being stable diminishes because the value of the right hand side of equation 3.1 will increase and thus approach the critical value of G/R.

Planar solidification fronts have been observed in many different alloys after laser melting or alloying e.g. in Titanium alloys by Folkes[23], in cast irons by Walker[40] and Chen[13] and in 316 stainless steel by Lamb[5].

To obtain an approximate average value of G/R to the correct order of magnitude, a schematic representation by Hawkes[41] of melt zone solidification, shown in Figure 3.11, can be used to obtain an approximate 'average R' from the melt zone centre-line. From earlier work by Walker[40] it can be assumed for conduction limited melt zones that Y in Figure 3.11 approximates to the beam diameter. G can be assumed to be equal to the difference between the boiling point, assumed to be reached at the top of the melt zone (See Figure 4.11 in Chapter 4) and the solidus temperature, at the bottom of the melt zone divided by the depth of the melt zone, X in Figure 3.11.

For the laser melted parent material using a 2.0 mm beam at 1.6 kW power and a speed of traverse of $10 mms^{-1}$.

$$G \sim 3000\ Kmm^{-1}$$

$$R \sim 4\ mms^{-1}$$

$$\text{Giving } G/R \sim 1000\ Ksmm^{-2}$$

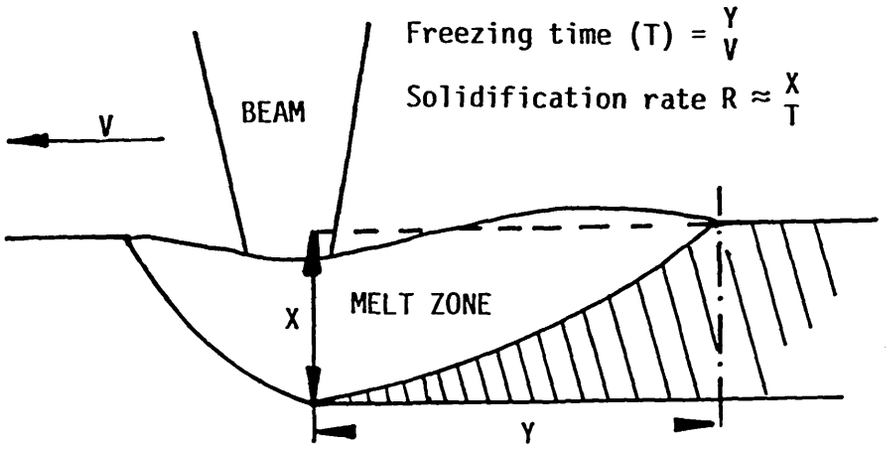


FIGURE 3.11

Schematic representation of solidification after Hawkes[41]

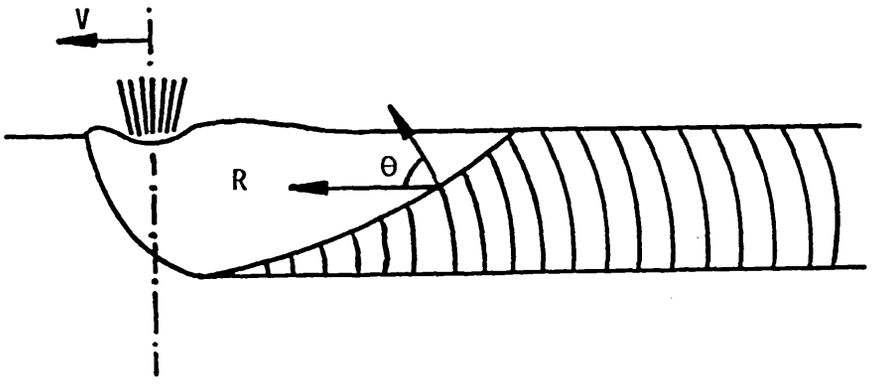


FIGURE 3.12

Longitudinal section of melt zone to illustrate the relationship between V, R and θ after Rappaz et al[37]

Coriell and Sekerka[42] predict that stability for a planar solid front morphology will occur when

$$\frac{G}{R} \geq \frac{\Delta T_o}{D} \qquad [3.2]$$

where ΔT_o is the temperature interval between the liquidus and solidus

Assuming values of 10^2K and $10^{-2}mm^2s^{-1}$ for ΔT_o and D respectively a value of

$$\Delta T_o/D \sim 10^4 \ Ksmm^{-2}$$

Thus $G/R < \Delta T_o/D$ and cellular or dendritic growth will occur, agreeing with observed results.

Laser processing produces melted zones containing material that has solidified at varying values of R as mentioned earlier. The value of R at any point can be related to the speed of traverse whilst laser processing via the relationship

$$R = V \cos \Theta \qquad [3.3]$$

where R is the rate of solidification
V is the speed of traverse
Θ is the angle between the vectors representing the traverse rate (V_T) and solidification rate (R)

Figure 3.12 after Rappaz et al[37] shows this more clearly.

From Photograph 3.12 it can be seen that the value of Θ is approximately 60^o for the majority of the

dendrites. Given that the speed of traverse was 10mms^{-1}, a value of R = 5 mms^{-1} is obtained which is very close to the values obtained using Hawkes' representation of solidification with Walker's assumptions of the size of the melt zone, of 4 mms^{-1}. However, Photograph 3.13 shows dendrites growing parallel to the direction of traverse on the top surface indicating a value of R equal to the rate of traverse, which was 10 mms^{-1}.

3.4.3 Solid state transformations

According to Pickering[43] the M_s temperature of Fe-0.1 wt% C-12 wt% Cr alloy is about 300^{o}C and is depressed below this value by further additions of C and Cr according to the equation:

$$\Delta M_s = -(474 \text{ wt\% C}) - (17 \text{ wt\% Cr}) \qquad [3.4]$$

The above equation gives an M_s temperature of ~260^{o}C for the present 420 stainless steel, an M_s of ~ 0^{o}C for a carbon content of ~0.65 wt% and an M_s of ~-190^{o}C for a carbon content of 1.1 wt%. The martensite will not occur when a hypo-eutectic structure of a composition exceeding the solid solubility limit solidifies and cools rapidly to room temperature; austenite retention will occur.

Results of a number of refrigeration experiments showed that by quenching some specimens in liquid nitrogen (-196^{o}C) significant increases in the hardness of the melt zone could be achieved. All specimens, except the laser melted parent material, with structures varying from cellular to fully dendritic experienced these increases. However, dendritic structures which contained more than a minimal amount of interdendritic eutectic did not experience any increase in hardness on quenching to -196^{o}C. These results agree with theory, the Lever rule

giving a eutectic content of less than 8% for a carbon content of 1.1 wt% C which has an M_s of -190°C.

Lamb[5] reported martensitic structures in the 420 base material after laser melting without alloying, similar to the results reported here. Similar work by Bee and Wood[44] on rapid solidification of 12 wt% Cr steels of various carbon contents by pendant drop melt extraction and melt spinning producing cooling rates of 10^5 and 10^6 Ks^{-1}, showed that the as-quenched structures were similar to those produced by other rapid solidification techniques. With increasing carbon content, the constituent phases were martensite (0.14 wt% C), martensite and austenite (0.45 wt% C) and austenite and M_7C_3 (0.87 and 1.25 wt% C). These results show that no martensite would be expected to form in 12 wt% Cr alloys containing more than 0.8 wt% C on cooling to room temperature agreeing with previous work by Pickering[43]. Molian[45] laser alloyed a 0.2 wt% C steel with up to 10 wt% Cr; he concluded on the basis of TEM observations that the microstructures were essentially dislocated lath martensite irrespective of composition (up to 10 wt% Cr) and cooling rate.

The initial increase in hardness shown in Figure 3.3 for carbon coatings between 0 and ~14 x 10^{-6} gmm^{-2} is believed to be due to an increase in the tetragonality of the martensite produced, even though less martensite is known to be formed when the carbon content of the melt zone is increased, Figure 3.6. The hardness decreases to a minimum when only austenite is present; the relatively high hardness of this austenite is due to the fine structure. The hardness then increases with the proportion of eutectic. The very high hardnesses reported in Section 3.3.4 achieved by multicycle treatments are due to the presence of primary carbides.

High cooling rates and fine structures have both been identified as having some effect on the formation of martensite. Ansell et al[46] have observed an increase in M_s with an increase in the cooling rate, (up to ~25 x 10^3 Ks^{-1}) in steels. It was proposed that rapid cooling prevented carbon atoms diffusing to imperfections in the austenite. Thus the resistance to shear of the austenite is decreased, leading to an increase in the M_s. Leslie and Miller[47] showed that the M_s could be lowered in Fe-Ni alloys by grain refinement achieved by thermomechanical means and concluded that the lowering of the M_s was due to the prevention of growth of the martensite after nucleation. However, in the present work the greatest influence on the M_s is the carbon content of the melted zone.

3.5 Conclusions

1) High levels of carbon (> 4.0 wt% C) can be introduced in a controlled manner into the surface of 420 stainless steel.

2) The hardness increased with carbon content up to ~900 Hv, associated with martensite formation; increasing austenite retention with further increase in carbon led to lower hardness values. until a hardness increase (up to ~1500 Hv) occurred as carbide appeared beyond the solubility limit.

3) Structures beyond the solubility limit suffered from cracking and porosity.

4) The amount of retained austenite increases with increasing carbon content.

5) Slow speeds of traverse (~10 mms^{-1}) created homogeneous melted zones for all single cycle treatments.

6) Surface roughnesses on single tracks varied between 0.7μm and 7.0μm longitudinally and were less than 1μm across the tracks. On partially overlapping tracks the surface roughnesses varied between 0.7μm and 5.0μm longitudinally and between 2.0μm and 5.0μm across them.

CHAPTER 4

RESIDUAL STRESSES

4.1 Introduction

Residual stresses are self-equilibrating stresses existing in materials or components under uniform temperature conditions. There are many ways in which residual stresses can be generated, for example, by forging, rolling, grinding, quenching and welding, but first the different kinds of residual stress must be understood.

Macherauch[48] describes a standard system of designation, classifying three different kinds of residual stress as being residual stresses of the first, second and third order. Using the term 'homogeneous' for "constant in magnitude and direction" the following definitions hold:

> Residual stresses of the first kind are nearly homogeneous across large areas, say several grains, of a material and are in equilibrium over the bulk of the material. Every interference in the equilibrium of forces and moments of a volume containing first kind residual stresses will change its dimensions
>
> Residual stresses of the second kind are nearly homogeneous across microscopic areas, say one grain or parts of a grain, of a material and are equilibrated across a sufficient number of grains. Macroscopic changes of the dimensions of a volume comprising second kind residual stresses may only

be observed if distinct disturbances of this equilibrium occur.

Residual stresses of the third kind are inhomogeneous across submicroscopic areas of a material, say some atomic distances within a grain and are equilibrated across small parts of a grain. No macroscopic changes of the dimensions of the stressed material will occur if this equilibrium is disturbed.

Usually, a superimposition of residual stresses of the first, second and third kind determines the total residual stress acting at a particular point of a material, a component or a structural part. Residual stresses are commonly referred to as being either macro or micro residual stresses. Macro refers to the first kind of residual stresses and micro to a combination of the second and third kinds.

Residual stresses will affect the fatigue[49], creep and brittle fracture[50] properties of a component as well as its structural stability[51] and corrosion behaviour[52]. It is, therefore, important that residual stresses be studied and understood.

4.2 Sources of residual stress

As the thermal history of a "weld bead on a plate" is similar to that of a laser melted track, residual stress generation has been studied in the welding literature and the different sources have been identified.

4.2.1 Shrinkage

Residual stresses in welded components arise directly from the localised shrinkage associated with the cooling down of the hot weld metal which is restrained by the cold sections surrounding the weldment. The melted metal is subjected to tensile stresses as soon as its temperature has fallen enough to allow the development of a marked yield strength. As the yield strength increases, with a further decrease in temperature, the tensile stresses in the continuously contracting melted material increase as well. The finally resulting tensile stresses parallel to the melted zone, in the case of steels can be equal to the yield stress[53,54]. These residual stresses caused by shrinkage can be reduced by pre-heating, as this will prevent shrinkage stresses developing between the pre-heat temperature and room temperature.

4.2.2 Plastic deformation at elevated temperatures

When temperature gradients give rise to thermal stresses and plastic deformation at elevated temperatures, internal stresses will be developed when the temperature gradients are removed after cooling. These internal residual stresses are often referred to as quenching residual stresses and will be maximised if a material has a low yield strength in the temperature range in which the maximum temperature difference, and thus maximum thermal stress, through the cross-section occurs. They will also be maximised when the treatment/materials combination gives rise to high thermal gradients. Laser surface treatments give rise to extremely high thermal gradients. However, quenching residual stresses will be minimised if cooling rates are such that plastic deformation at elevated temperatures is unable to occur. Cooling rates of the order of up to $\sim 10^5\ ^{o}cs^{-1}$ in the solid

state are typically associated with laser surface treatments, which is several orders of magnitude greater than those associated with conventional welding techniques.

4.2.3 Phase transformations

In a steel cooling from above the austenite temperature a transformation to ferrite, bainite or martensite will occur over a temperature range. These transformations are associated with volume increases. In laser surface melting or alloying the transforming material is constrained by the surrounding material, and, assuming the transformation temperature is sufficiently low that the material has a reasonable yield strength after transformation, may be subjected to compression. The higher the yield strength in the temperature range of the austenite transformation the more pronounced will be the residual stresses and therefore the magnitude of these stresses will increase with decreasing transformation temperature.

However, it is possible for plastic flow to occur at stresses much lower than the yield stress of either phase during a phase transformation. This phenomenon is known as transformation plasticity. Jones and Alberry[55] measured this stress in two steels, 2CrMo and 9CrMo, having undergone a simulated welding cycle from austenite to ferrite on cooling. The stresses were also calculated assuming that the tensile stress accumulated in the austenite off-loads elastically. The calculated stresses were 270 MPa and 390 MPa respectively. The measured values were an order of magnitude smaller at 30 and 62 MPa respectively.

Transformation plasticity is thought to result from the superposition of the low external stress field and the high local stress field associated with transformations[56]. Greenwood and Johnson[56] adopted the flow theory for a rigid, ideal plastic material and showed that on passing through the transformation

$$\epsilon = \frac{5}{6} \frac{\Delta V_T}{V} \frac{\sigma}{\sigma_y} \qquad [4.1]$$

where ϵ is the total strain, $\Delta V_T/V$ is the volume dilation associated with transformation, σ is the applied stress and σ_y is the yield stress of the weaker phase.

Other theories to explain transformation plasticity include Scheit's concept[57]; when a martensitic transformation occurs under stress, the product phase chooses an orientation minimising the total energy, including that resulting from the applied stress. Clinard and Sherby[58] have proposed a creep mechanism to explain the observed transformation plasticity.

A number of suggestions have been made concerning methods by which transformation plasticity can be introduced into calculations. These include the use of an unusually low yield stress during transformation, and the use of an applied strain to represent the enhanced dilation or contraction of the material as it transforms in the presence of an applied stress.

4.3 Scope of the investigation

As mentioned above there are three sources of residual stress; shrinkage due to cooling, phase transformation and plastic deformation at elevated

temperatures. The contributions made by each of these to the final stress distribution are dependent upon both time and temperature. The spatial extent of each contribution is unknown as is the interaction between the various stress sources. Therefore, the resultant stress distribution within and around a laser melted zone cannot be calculated, and thus have to be measured.

Previous work by Lamb[5,59] and James et al[60] on residual stresses of laser melted specimens have dealt with partially overlapping tracks. Lamb[5,59] found that the stresses in single tracks on 420 steel were compressive and that in partially overlapping tracks the stresses were tensile and became more so the smaller the amount of intertrack advance. By measuring the stresses in single laser melted and alloyed tracks a greater understanding of the relative stress contributions is aimed for without the additional complications caused by thermal cycling in partially overlapping tracks.

4.4 Experimental

4.4.1 Stress measurements

The residual stresses were evaluated by the X-ray method, which has the major advantage of being a non destructive technique enabling the residual stresses at many points on a surface to be measured. Other methods of stress evaluation include the mechanical techniques which compare the stressed with the relaxed state of a body. These necessitate some removal of material and hence damage to the component.

4.4.2 Principles of the X-ray technique

The X-ray technique measures stress indirectly by

measuring the shift in the angle of the diffracted peak, $\Delta\theta$ for crystal planes oriented at different angles to the specimens surface Ψ, Cullity[61].

Isotropic elasticity theory gives the relationship between measured strains and uniaxial surface stress σ, as

$$\varepsilon_{\Psi} = (\frac{1+\nu}{E})\sigma \sin^2\Psi - \frac{\nu\sigma}{E} \qquad [4.2]$$

where E is Youngs modulus
ν is Poissons ratio
ε_{Ψ} is the strain at an angle

Ψ to the surface where Ψ is the angle between the direction of the measured strain and the normal to the specimen surface.

The engineering stress and strain in a component exists down to the atomic level, and is reflected in the crystal structure where the separation of atomic planes varies according to the stress acting normal to them. In any material these planes have a characteristic equilibrium separation which, under the action of an applied stress, changes elastically by an amount given from the relevant elastic moduli. This separation may be measured using X-ray diffraction.

According to Bragg's Law, a beam of X-rays with a wavelength λ incident on an array of lattice planes is diffracted through an angle 2θ, where

$$\lambda = 2d \sin\theta \qquad [4.3]$$

and d is the interplanar spacing. Changes in d (i.e. strain, ε) result in a change in $2\theta = (\Delta 2\theta)$ which is described by differentiating equation[4.3]:

$$\varepsilon_\Psi = \frac{\Delta d}{d} = \frac{-\Delta 2\theta_\Psi}{2\tan\theta} \qquad [4.4]$$

where $\Delta 2\theta_\Psi = (2\theta_\Psi - 2\theta_e)$ and $2\theta_e$ is the equilibrium value of $2\theta_e$ obtained from a stress-free sample.

The X-ray method of stress measurement involves determination of the strains ε_Ψ by evaluating changes in the positions of diffracted X-ray peaks recorded from lattice planes inclined at various angles Ψ to the sample surface. The basic layout is shown in Figure 4.1. Consequently, by measuring $\Delta 2\theta_\Psi$ the strain may be calculated. Substituting for ε (equation [4.4]) into equation [4.2] gives

$$\Delta 2\theta_\Psi = -2\tan\theta \left(\frac{1+\nu}{E}\right)\sigma \sin^2\Psi + K \qquad [4.5]$$

where K is a constant; and $\Delta 2\theta_\Psi$ is the angular shift of the diffracted peak recorded from various angles Ψ with respect to the specimen surface.

From equation [4.5] a plot of $2\theta_\Psi$ against $\mathrm{Sin}^2\Psi$ results in a straight line with a slope of

$$-2\tan\theta \left(\frac{1-\nu}{E}\right)\sigma \qquad \text{(from ref. 62)}$$

The value of Ψ is varied by rotating the specimen with respect to the incident beam. A practical limit of Ψ is $\sim 60^\circ$ which is controlled by the spread and the focussing of the X-ray beam.

Equation [4.5] shows that the sensitivity of stress measurement increases as θ approaches $90^\circ (\tan\theta \to \infty)$. The accuracy of the technique is maximised by

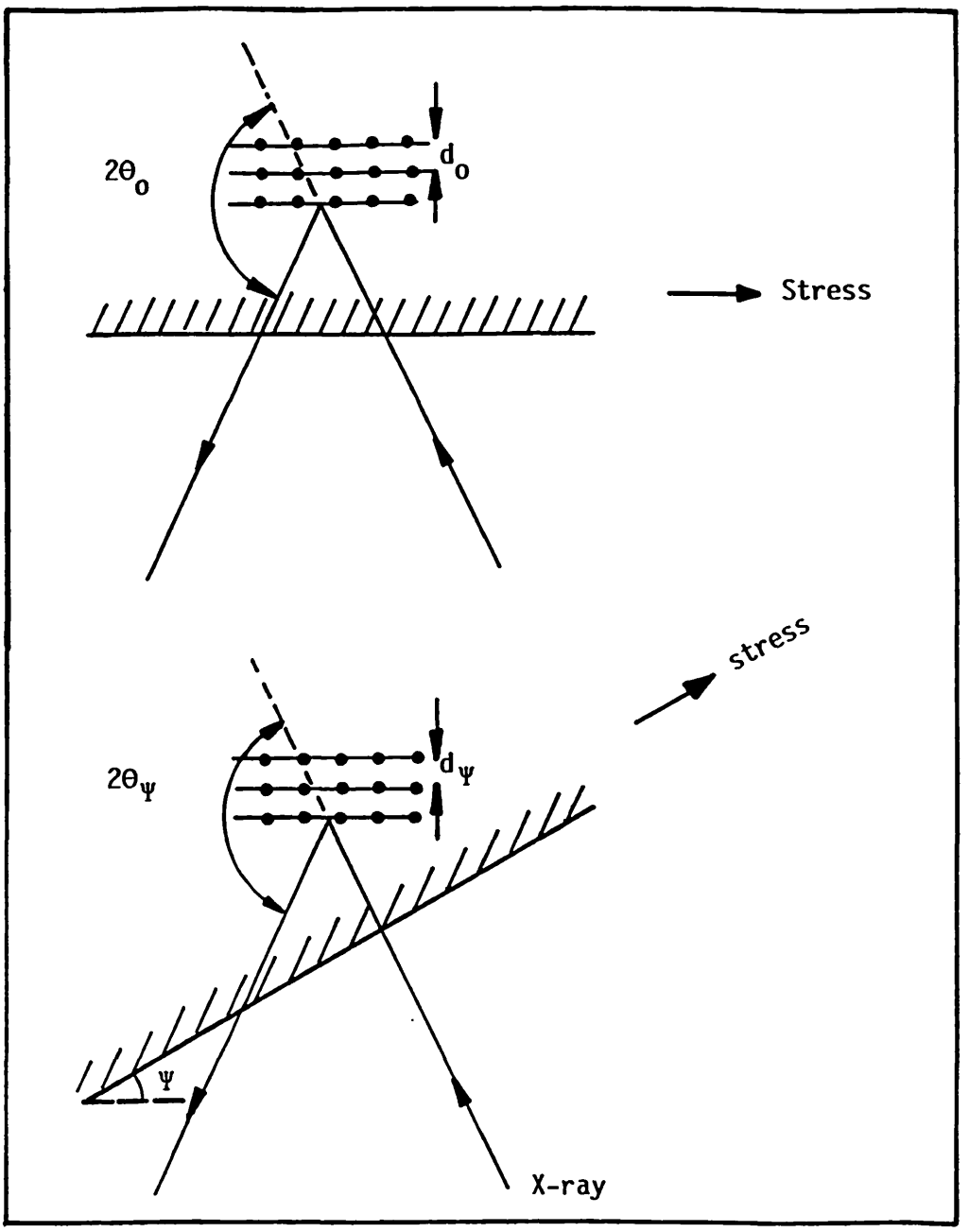


FIGURE 4.1

Schematic diagram showing the orientation of lattice planes and X-ray beams with respect to the specimen surface and direction of the strain measured at an angle ψ with respect to the sample surface [62]

choosing an X-ray wavelength which produces a strongly diffracted beam at a large diffraction angle (2θ). On this basis a combination of CrKα radiation and the {211} planes was used. This gave a diffraction angle of 156^{o}, on a value of $\theta = 78^{o}$.

Accuracy of the system is quoted to be $\pm$20 MPa[62].

4.5 Specimens

Three discs 32mm in diameter and 10mm thick were processed using a 1.6kW, 2.0mm beam at $10mms^{-1}$, to produce a single track on each specimen. The masses of the carbon coatings were 0, $10x10^{-6}$ and $40x10^{-6}$ gmm^{-2} for specimens 1, 2 and 3 respectively. The structures produced in the melted zone of these specimens were fully martensitic, partially martensitic and almost fully austenitic as described in Chapter 3.

To enable stresses below the surface to be measured a slope of 1:100 was ground longitudinally along the specimen. The grinding operation was carried out slowly, with a freshly dressed grinding wheel, under flood cooling conditions to prevent heating and to minimise the introduction of stresses. The specimens were then electrolytically polished to remove the damaged layer of material containing residual stresses caused by the grinding operation, estimated to extend ~10μm below the surface[63]. Polishing was carried out in a solution of 15% perchloric acid and 10% glycerol in ethanol. This mixture is potentially explosive and must be kept below $30^{o}C$.

4.6 Operation

The specimens were placed on a numerically controlled x-y table and the distance from the centre of the goniometer circle to the specimen was measured and set, with the aid of a dial gauge to an accuracy of 50μm.

The incident X-ray beam was collimated down to a diameter of 800μm and the position of the diffracted peaks was obtained by means of a position sensitive detector.

The diffractometer and x-y table were controlled by a computer based system which also logged and processed the test data. The x-y table moved systematically through a grid of 44 points, the co-ordinates of which are shown in Figure 4.2. The slope ground onto the specimens enabled the stresses below the surface to be measured. The progressively larger steps in the longitudinal direction were introduced as it was believed that the most dramatic changes in stress would occur close to the surface.

Each residual stress measurement was evaluated from at least ten measurements of lattice spacings spread over a range of orientations to the surface, Ψ varied from 3 to 50^{o}. The time taken for each stress measurement was typically about 400 seconds after which the computer provided a plot of 2θ against $\sin^2\Psi$. A straight line was fitted to the data and the stress level printed out.

4.7 Results

4.7.1 Computer output

Figures 4.3(a) and (b) show two outputs from the computer. Figure 4.3(b) has been included as curvature is displayed in the 2θ against $\sin^2\Psi$ plot, the significance of which will be discussed later.

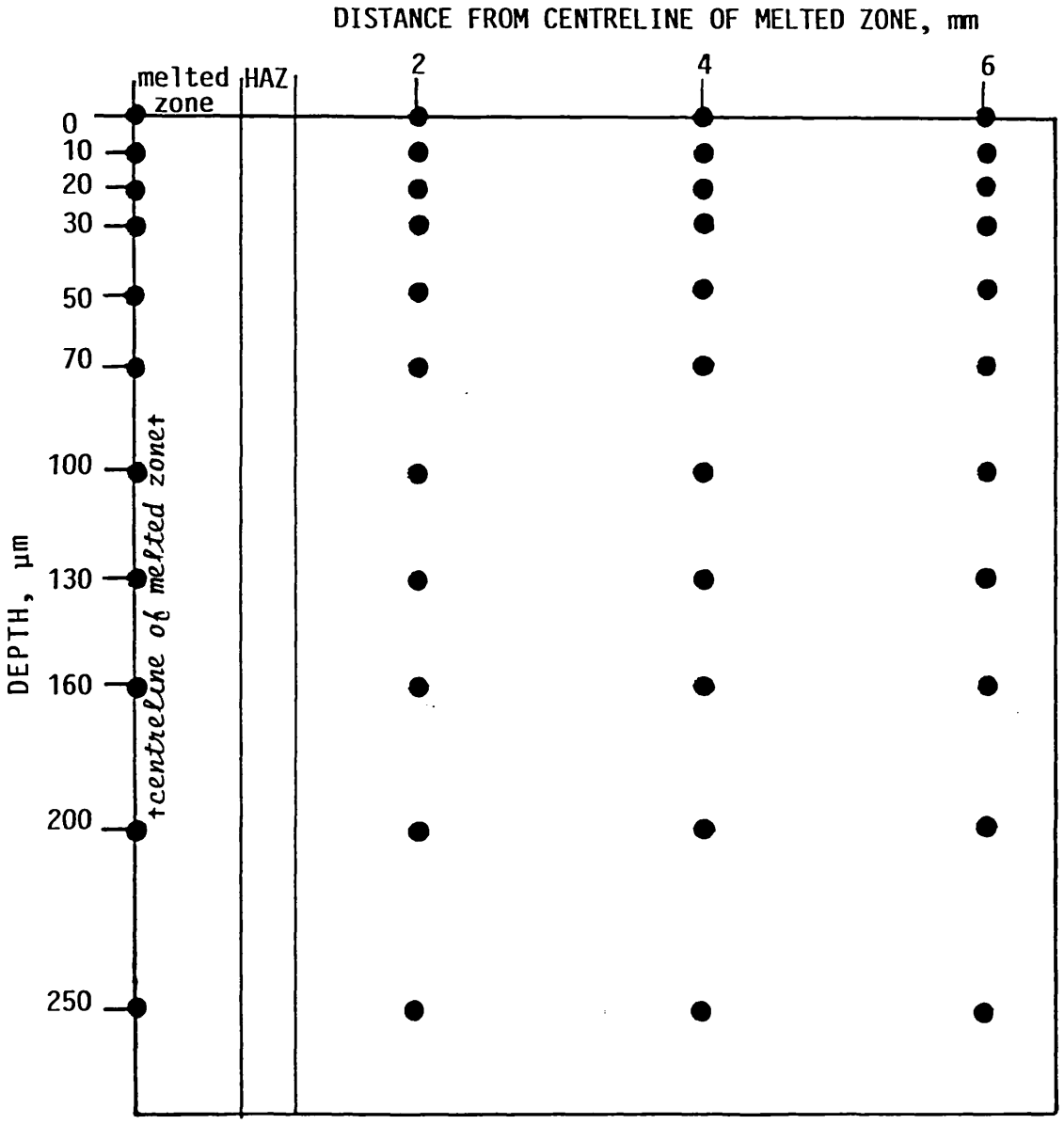
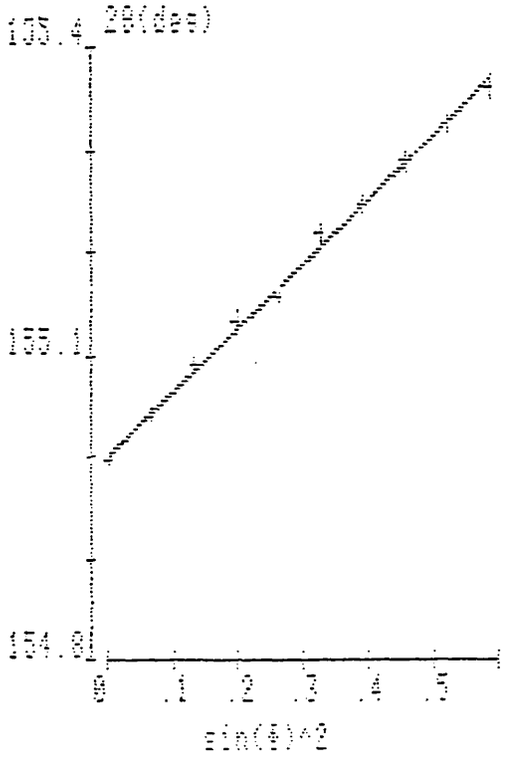


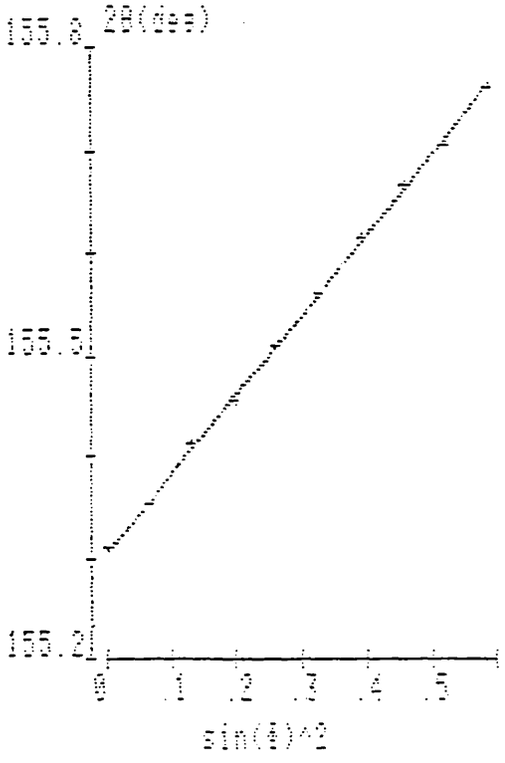
FIGURE 4.2

Display of co-ordinates of the points at which stress measurements were made

No of PSI STEPS = 10 RECORDING TIME = 15 seconds

PSI	2THETA POSITION		INTENSITY		FWHH
	Peak	C of Gravity	Peak	Bgrnd	
3.0	154.998+- .004	155.309+- .003	3186	408	1.14
15.1	155.041+- .005	155.353+- .003	3108	411	1.12
21.3	155.092+- .007	155.411+- .003	3249	405	1.13
26.4	155.134+- .010	155.455+- .003	3206	408	1.20
30.8	155.156+- .004	155.512+- .003	3201	383	1.11
34.9	155.221+- .007	155.561+- .003	3248	380	1.14
38.8	155.248+- .007	155.616+- .003	3067	372	1.18
42.5	155.290+- .010	155.667+- .003	3157	372	1.12
46.3	155.325+- .008	155.706+- .003	3052	353	1.17
50.0	155.364+- .012	155.764+- .003	2868	354	1.20





RESULTS USING PEAK TURNING POINT

LINEAR FIT:

STRAIN e(11) = -1156 +- 26

STRESS = -245 +- 5

RESULTS USING CENTRE OF GRAVITY

-1428 +- 13 (microstrain)

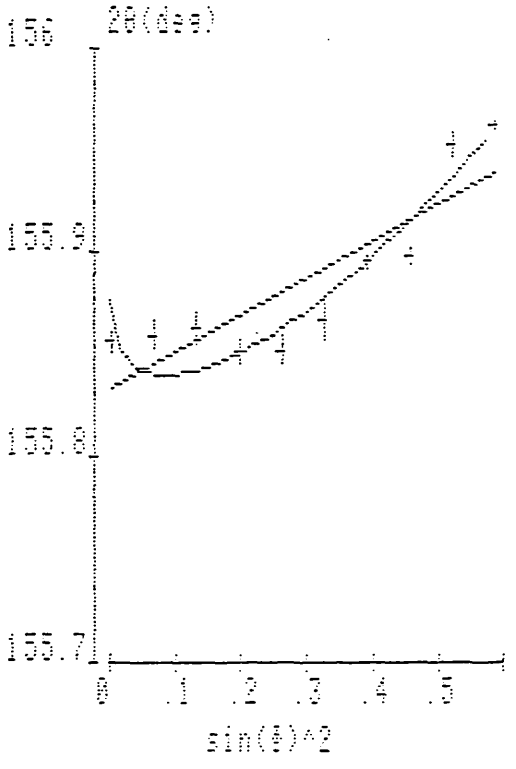
-303 +- 3 (MPa)

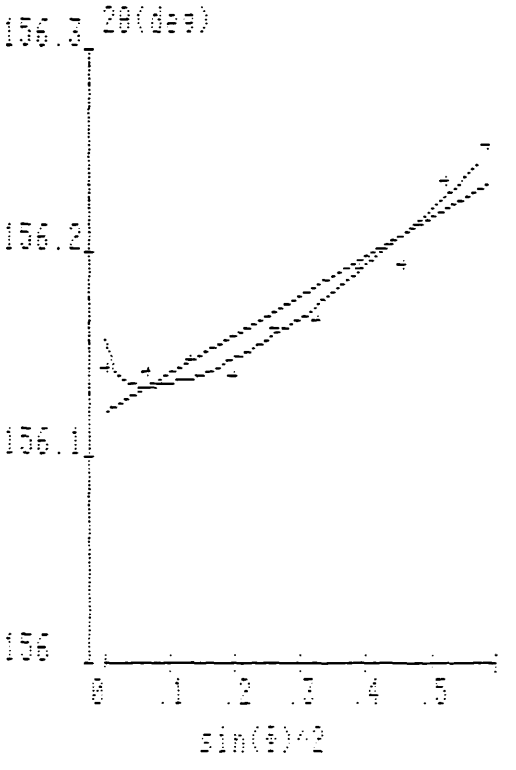
FIGURE 4.3(a)

Output from computer

No of PSI STEPS = 10 RECORDING TIME = 15 seconds

PSI	2THETA POSITION		INTENSITY		FWHH
	Peak	C of Gravity	Peak	Bgrnd	
3.0	155.857+- .005	156.143+- .002	9210	544	.89
15.1	155.859+- .007	156.142+- .002	9417	553	.90
21.3	155.864+- .008	156.148+- .002	9300	540	.87
26.4	155.851+- .005	156.140+- .002	9558	554	.89
30.8	155.852+- .007	156.163+- .002	9383	552	.85
34.9	155.868+- .010	156.167+- .002	9858	535	.80
38.8	155.896+- .003	156.192+- .002	10102	528	.84
42.5	155.899+- .004	156.194+- .002	9856	514	.82
46.3	155.953+- .006	156.236+- .002	9789	523	.89
50.0	155.963+- .002	156.253+- .002	9586	539	.86





RESULTS USING PEAK TURNING POINT

LINEAR FIT:

STRAIN e(11) = -335 +- 71

STRESS = -71 +- 15

RESULTS USING CENTRE OF GRAVITY

-348 +- 50 (microstrain)

-74 +- 10 (MPa)

FIGURE 4.3(b)

Output from computer

Going through Figure 4.3(a) in detail we have:

"No of PSI steps = 10". This tells us that the position of the diffracted beam, the "2 THETA POSITION" has been evaluated at 10 different Ψ angles. The values of these Ψ angles are given together with the position of the diffracted beam, calculated by two means. The first by the position of the turning point or point of highest intensity, "PEAK", and the second by the centre of gravity of the peak, "C of GRAVITY".

Intensity of peak and background are self-explanatory, whilst the full width half height [F.W.H.H.] values can give an indication of any peak broadening which can be caused by the presence of microstress.

The left hand plot of 2θ against $\sin^2\Psi$ uses the "peak" values of the 2θ position whilst the second uses the "C of Gravity" values. Two lines are then fitted to each set of data, the first is a linear fit and the second is a higher order polynominal function. Figure 4.1(b) shows this more clearly. The results quoted later are of those using the peak turning point.

4.7.2 Results of specimens 1, 2 and 3

Due to the wealth of information gained from the number of residual stress measurements taken, the figures drawn below are composed from some of the results data tabulated in Appendix 4 and have been selected to illustrate important trends.

4.7.2.1 Specimen 1 - Unalloyed

The structure of the laser melted zone was fully martensitic with a carbon content of 0.2 wt% C.

Transverse stresses

Figure 4.4 shows the transverse stresses plotted against the position in mm away from the centre line of the melted zone at different depths.

From Figure 4.4 it can be seen that the stresses in the melted zone are compressive and the magnitude of these stresses decreases with increasing depth. The stress in the melted zone at the surface, ~-420 MPa is very similar to that recorded by Lamb[5,59] ~-500 MPa on a single laser melted track in the same steel using a beam of 1.5kW and 2.0mm at 60mms^{-1}. Away from the melted zone the stresses become less compressive, producing tensile stresses at the 2.0mm point at depths of 70 and 100μm. Further from the melted zone the stresses tend to level off or decrease. The net result is that at the 6.0mm point the residual stresses at all depths are very similar lying between -50 and -100 MPa.

Longitudinal stresses

Figure 4.5 shows the longitudinal stresses plotted against the position in mm away from the centreline of the melted zone at different depths.

From Figure 4.5 it can be seen that the stresses in the melted zone at all depths are compressive and lie between -100 and -200 MPa. These are very similar to the ~-120 MPa measured by Lamb[5,59] in the same steel processed under the conditions mentioned above. Away from the melted zone the stresses initially tend to become more compressive before becoming less compressive. The net result is that the layers closest to the surface are in

Specimen 1 - Unalloyed

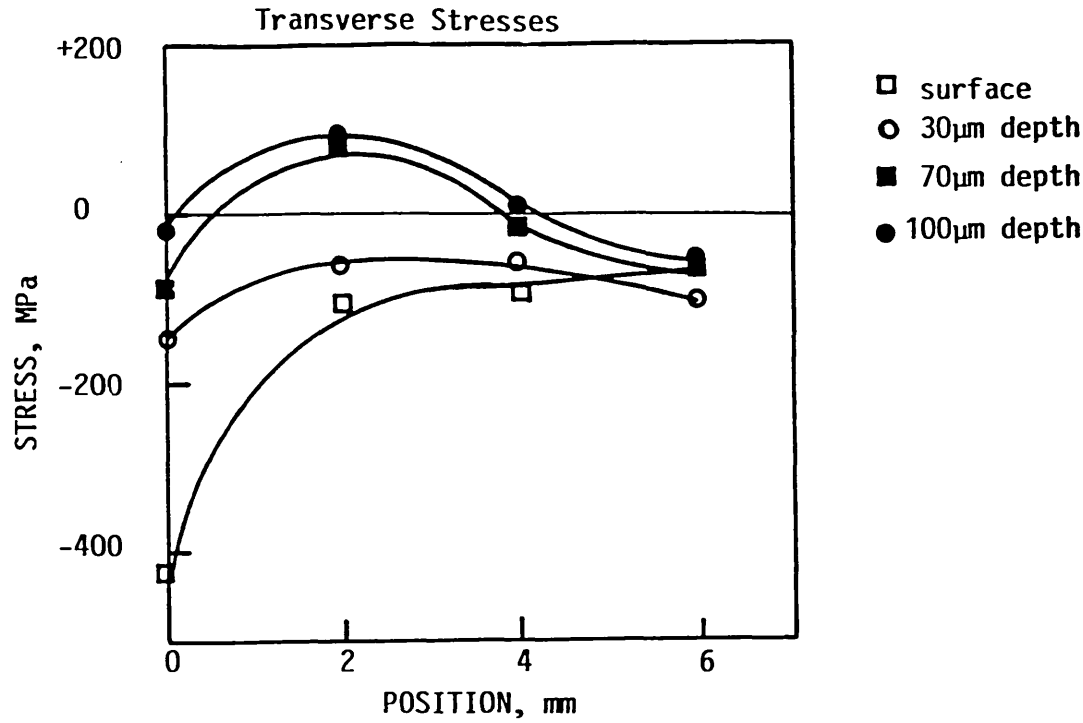


FIGURE 4.4

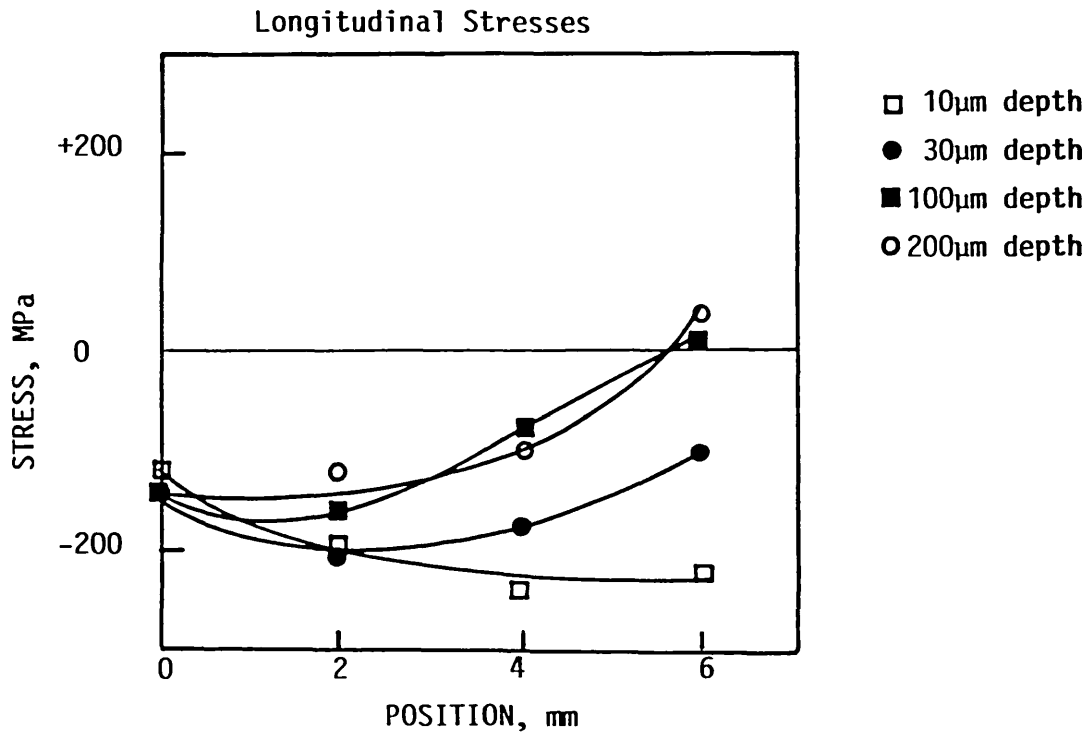


FIGURE 4.5

compression 6mm from the melted zone, whilst the deeper layers are in a state of tension.

4.7.2.2 Specimen 2 - Alloyed

Mass of carbon coating 10×10^{-6} gmm^{-2}. The structure of the laser melted zone was partially martensitic with a carbon content estimated to be ~0.5 wt% C.

Transverse stresses

Figure 4.6 shows the transverse stresses plotted against the position in mm from the centreline of the melted zone at different depths.

From Figure 4.6 it can be seen that the melted zone is in compression at almost all depths ranging from ~0 MPa at a depth of 200μm to -200 MPa at a depth of 70μm. In the layers close to the surface there is a sudden increase in the magnitude of the compressive stresses away from the melted zone from ~-80 MPa in the melted zone to ~-450 MPa 6mm away from it. No explanation was found to elucidate this effect. Further from the specimen surface the stresses become only slightly more compressive away from the melted zone and these results are very similar to those obtained by Marsden et al[64] for a single track processed under identical conditions but with a lighter carbon coating of only 4.8×10^{-6} gmm^{-2}.

Longitudinal stresses

Figure 4.7 shows the longitudinal stresses plotted against the position in mm from the centreline of the melted zone at different depths.

From Figure 4.7 it can be seen that the stresses in the melted zone are compressive from the surface at ~-125 MPa to a depth of 100μm, after which they are tensile, ~+40 MPa at a depth of 160μm. Away from the melted zone, the

Specimen 2 - Alloyed

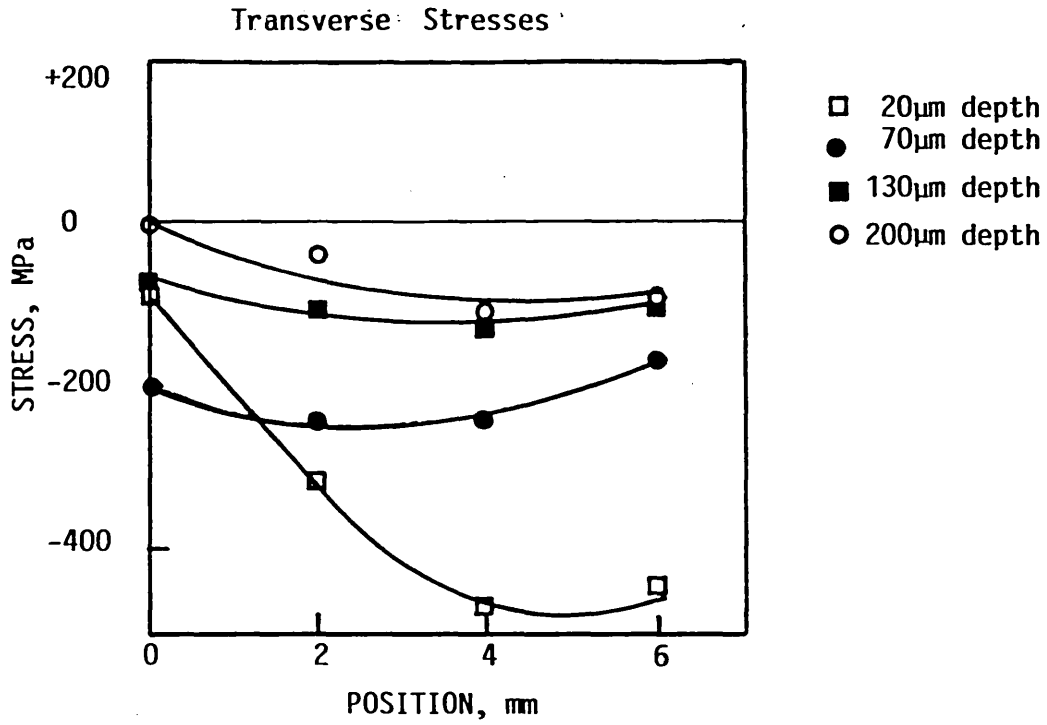


FIGURE 4.6

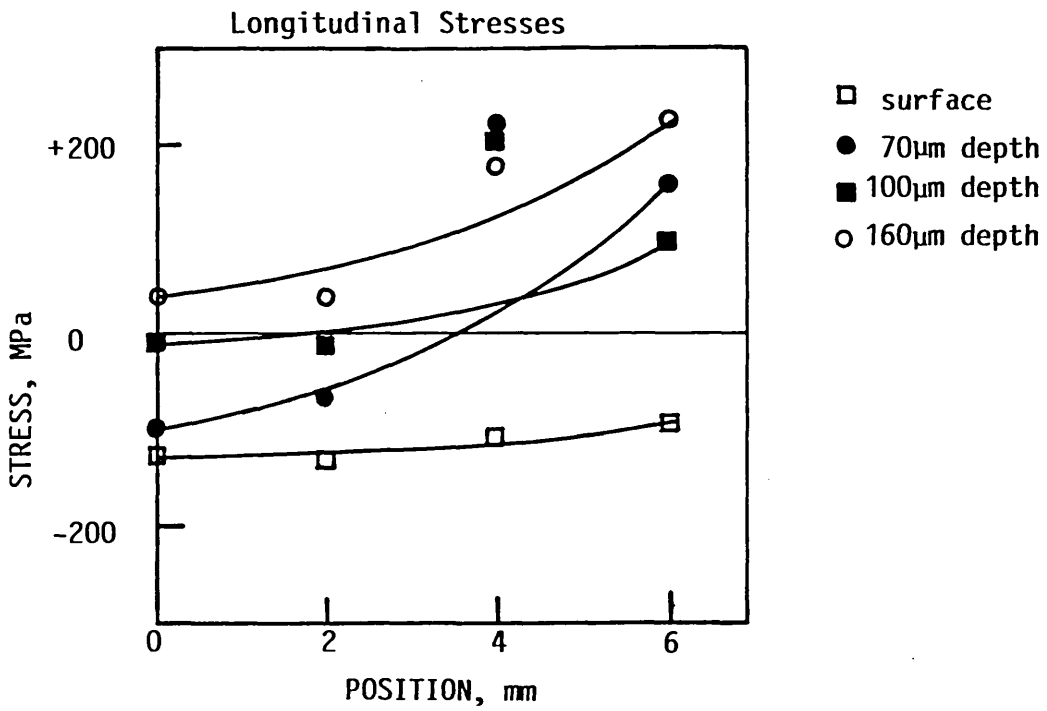


FIGURE 4.7

trend at all depths is for the stresses to become less compressive or more tensile.

4.7.2.3 Specimen 3 - Alloyed

Mass of carbon coating 40 x 10^{-6} gmm^{-2}. The structure of the melted zone was almost fully austenitic with a carbon content estimated to be ~1.0 wt% C.

Transverse stresses

Figure 4.8 shows the transverse stresses plotted against the position in mm away from the centreline of the melted zone at different depths.

From Figure 4.8 it can be seen that the stresses in the melted zone vary considerably ranging from -70 MPa at a depth of 20μm to ~+160 MPa at a depth of 200μm. Away from the melted zone to the 4mm point the stresses at all depths decrease becoming more compressive or less tensile. Taking a section down through the 4mm point the stresses close to the surface are compressive ~-250 MPa whilst those further from the surface are tensile +100 MPa at 200μm. From the 4mm point to the 6mm point the stresses in the layer 20 to 130μm below the surface experience a dramatic change in sense from highly compressive (~-100 to ~-250 MPa) to highly tensile (~+100 to ~+250 MPa), the cause of which is unknown.

Longitudinal

Figure 4.9 shows the longitudinal stresses plotted against the position in mm from the centreline of the melted zone at different depths.

Specimen 3 - Alloyed

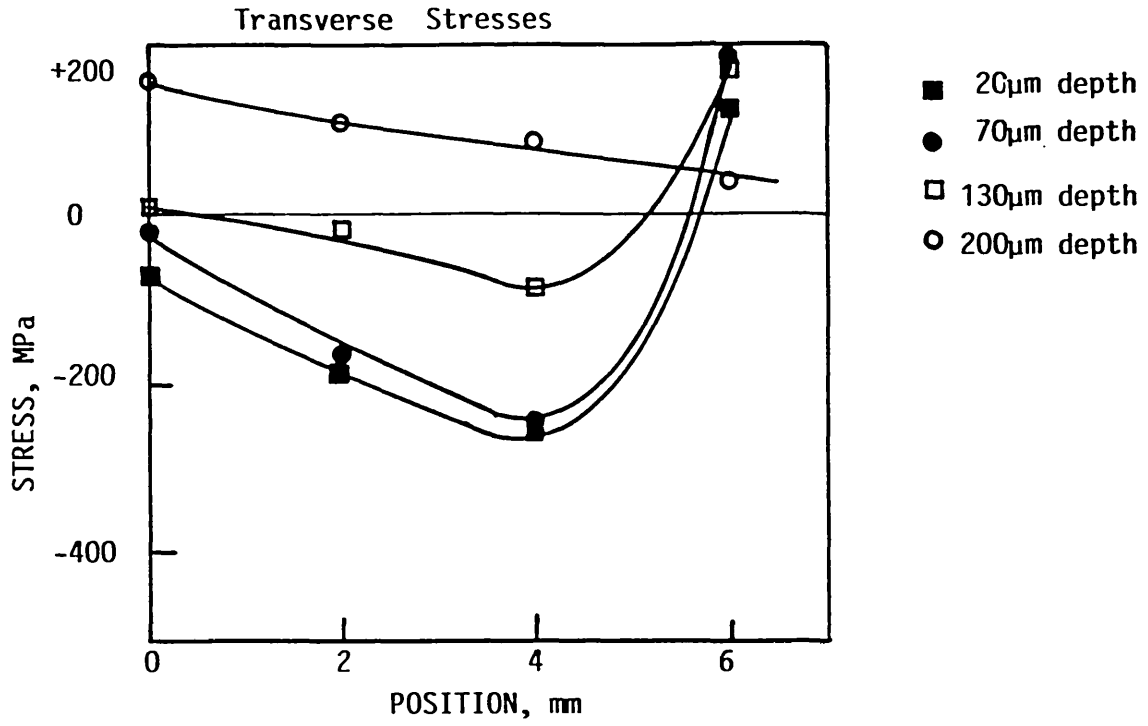


FIGURE 4.8

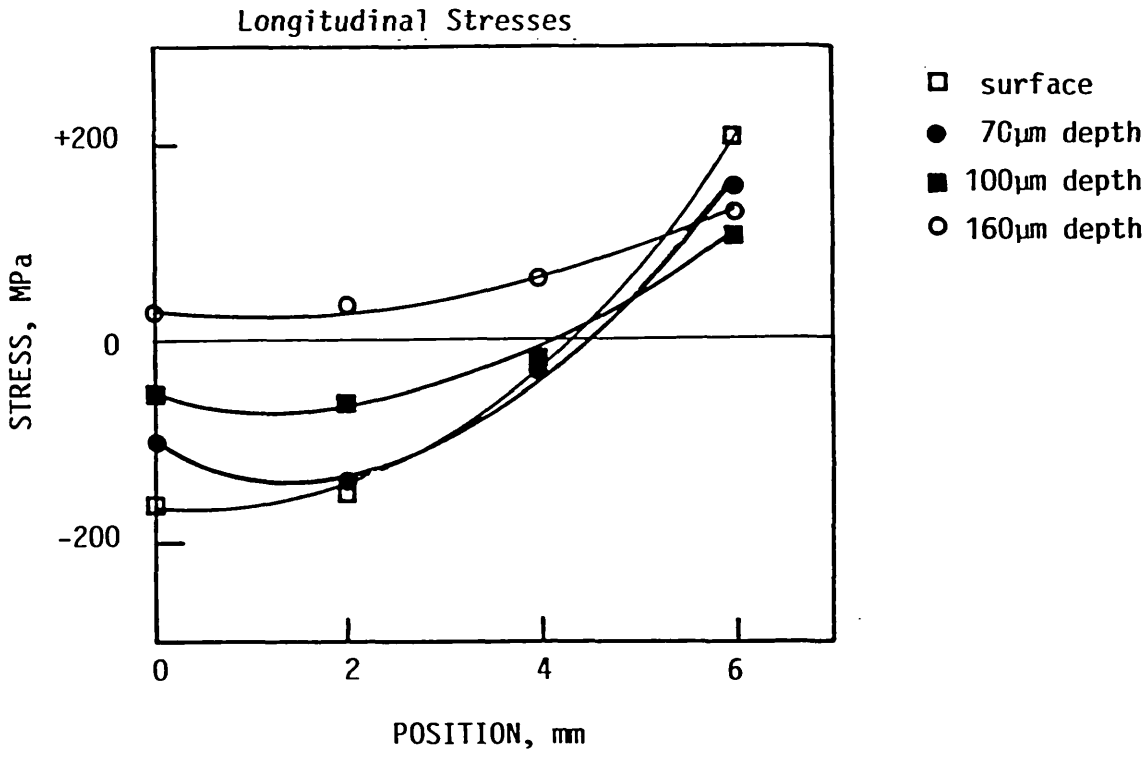


FIGURE 4.9

From Figure 4.9 it can be seen that the stresses in the melted zone vary from -170 to +20 MPa, the largest compressive stresses tending to be close to the surface whilst the tensile stresses are in the deeper regions of the melted zone. This is also the case for the fully and partially martensitic specimens. Away from the melted zone the trend is for the stresses to become less compressive and more tensile with distance.

4.7.2.4 General trends

Comparing all the Figures from 4.4 to 4.9 it can be seen that as the carbon content of the melt pool is increased the transverse stresses in the molten pool become less compressive and more tensile. Ranging from ~-20 to ~-400 MPa in the fully martensitic specimen to between ~+20 and ~-160 MPa in the austenitic specimen.

It can also be seen that the general shape of the longitudinal stress profiles is similar in all the specimens. This is also the case for the shape of the transverse stress profiles; the only anomaly to this is the shape of the transverse profile of Specimen 1, the fully martensitic specimen, from the melted zone to the 2mm point. Between these two points the stresses become markedly less compressive and in some cases tensile whilst in the other specimens there is a trend for the stresses to become less tensile and more compressive.

It should be noted that there is always an HAZ which transforms to martensite in all three specimens, which could explain the trend, in Specimens 2 and 3, for the stresses to become more compressive and less tensile from the melted zone towards the 2mm point in both the transverse and longitudinal directions.

4.8 Discussion

Initially, this section discusses factors effecting the accuracy of the results including curvature in the plot of 2θ against $\sin^2\Psi$, peak broadening and the effect of material removal, before moving on to discuss the factors effecting the magnitude and sense of the stresses as well as the distance over which they extend. These include, transformation plasticity, plastic deformation at elevated temperatures and stresses within and away from the melted zone.

4.8.1 Curvature in the plot of 2θ against $\sin^2\Psi$

Though the X-ray method of measuring residual stresses is essentially a surface measuring technique, the X-rays do penetrate the specimen surface to a finite depth, which is typically about 10μm. The material in this narrow band below the surface may be subject to a more complex stress condition than the uniaxial condition assumed at the surface. If this stress condition contains shear elements then curvature in the 2θ against $\sin^2\Psi$ plot will result[62]. The deviation of the curve from the linear fit is dependent upon the size of the shear stress. In this work few of the plots displayed curvature and those that did, deviated no more from the linear fit than that displayed in Figure 4.3(b).

The presence of curvature in a plot indicates that the measured value printed is not strictly the true value, as the shear component has not been taken into account. However, the change in the measured value printed, if the shear stress was taken into account would not be large and would not affect the trends observed and reported earlier.

4.8.2 Peak broadening and microstress

Several mechanisms lead to the broadening of diffraction peaks. Amongst these are the apparatus used, the diffraction angles employed, the crystal size and the presence of microstresses.

In this work the same apparatus and the same diffraction peak was used throughout, and therefore these factors should not contribute to any variation in the broadening of the peaks from one position in the material to another.

Peak broadening can be used to determine the crystal size[65], however this technique can only be used when the crystal size is less than 30nm. As the cell size within the melted zone and the grain size in the parent material is several orders of magnitude greater than 30nm. crystal size can also be ignored as a source of peak broadening.

The presence of peak broadening is therefore indicative of microstress, which is quite likely to be present when martensite forms due to the regions of high strain adjacent to the martensite laths.

Figure 4.10 shows the full width half heights of the peaks created from material in the melted zone and 6mm from the melted zone at different depths in Specimen 1, in the transverse direction. The 6mm position was included as it will not have transformed to martensite and would therefore be less likely to contain a peak broadening contribution due to microstress.

From Figure 4.10 it can be noted that there is usually little difference between the full width half heights of the two positions at any depth, indicating that

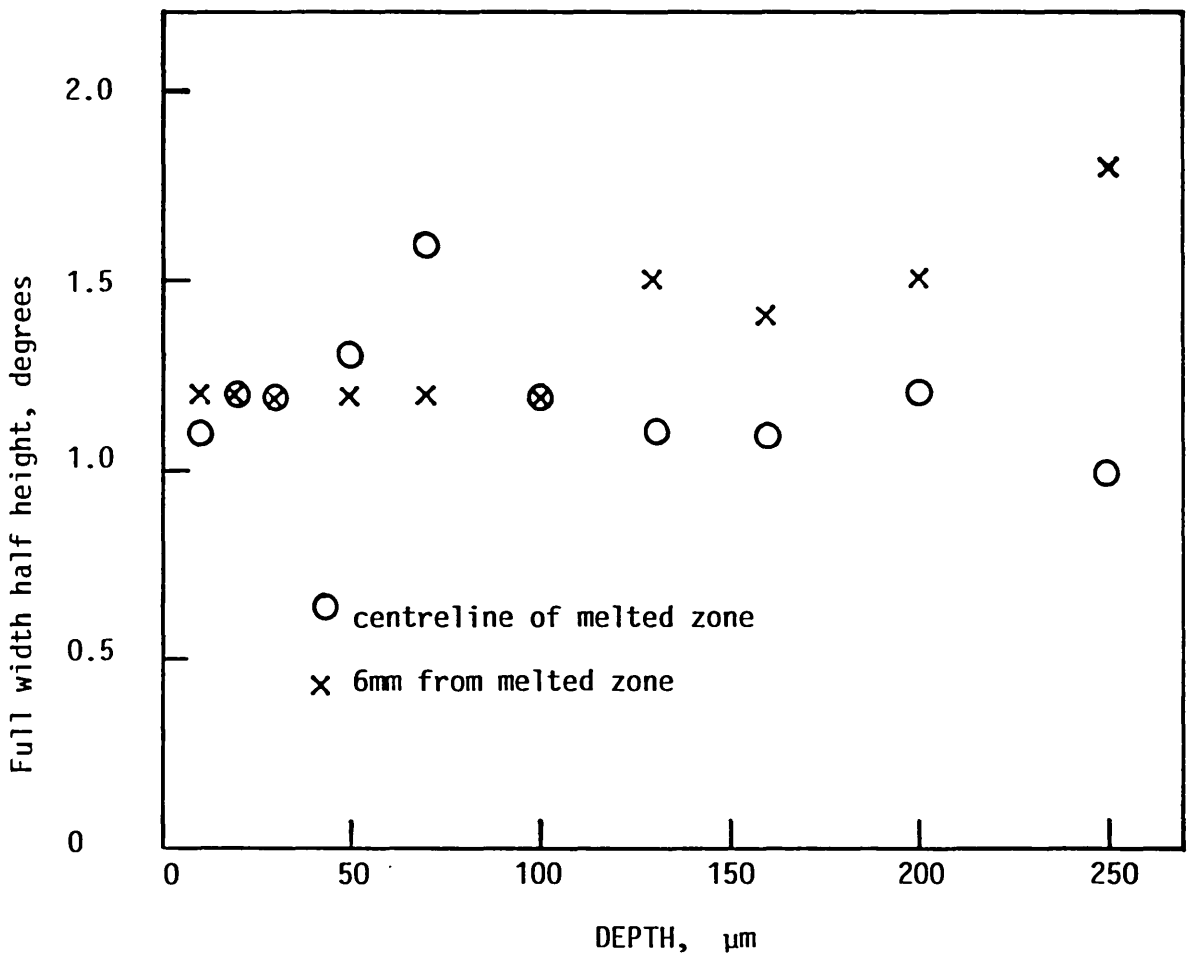


FIGURE 4.10

Full width half heights against depth

there is a comparable degree of microstress at the two positions at any depth.

4.8.3 Effect of material removal

To enable the measurement of the subsurface stresses, material was removed by grinding a slope of 1:100 onto the specimen surface. The measured stresses in the longitudinal direction are not parallel with the original specimen surface and therefore should be corrected. However, as the angle is small the correction required is small and has been ignored.

Another consequence of the material removal is that the measured stresses after removal are not the same as the stresses that existed before it. This is because as stressed material is removed from the specimen surface, the remaining material relaxes leading to a redistribution of the internal stresses. Work by Lamb[5] indicates that the correction is small and does not change the general stress profile and it has been ignored in this work.

4.8.4 Transformation plasticity

The highly compressive residual stresses in the unalloyed single laser melted track agrees with results obtained previously by Lamb[5,59] and Marsden[64]. High compressive stresses set up by the martensitic phase change have been reported in the welding literature, Jubb[66], Luxmore, Kan and Egan[67] and Macherauch[68]. These high compressive residual stresses indicate that transformation plasticity plays only a minor role in relieving the stresses. Parlane[53] suggests that any stresses accumulated before transformation are relaxed during transformation, therefore the residual stress

build up has to start again after the transformation process is complete. Tensile stresses would, therefore, be expected in the weld pool. However, the compressive stresses generated when the austenite to martensite phase change was taking place, involving a 3% volume expansion. fulfil the conditions for transformation plasticity to occur and confirm that it has little effect in this case.

It is known that transformation plasticity is a time dependent phenomenon, where the dependence of the flow stress, σ_f to the strain rate $\dot{\varepsilon}$ may be described as

$$\sigma_f = K\dot{\varepsilon}^m$$

where K and m are constants.

A values of m = 0.1 is for most materials in their normal state. Values of 0.3 to 0.6 are typical for super-plastic materials whilst a value of m ~ 1 was deduced for a 15.4 wt% Ni Fe alloy under transformation plasticity conditions by Kot and Weiss[69]. Due to the high cooling rates associated with laser processing the strain rate would be high leading to a high flow stress and thus little relaxation of the stress.

4.8.5 Plastic deformation at elevated temperatures

It was noted that the stresses in both directions in the melted zones of all the specimens tended to become less compressive and more tensile with depth. As it occurs for all the specimens it cannot be due to variations in the quantity of martensite with depth as Specimen 3 does not undergo the martensitic transformation.

Macherauch[68] describes how temperature differences between the surface and core of a weld. set-up

during cooling, can lead to stresses building up between the surface layers and the core. In welding it is assumed that the surface layers cool first. This would lead to compressive stresses in the surface layers and tensile stresses in the core if temperature differences were the sole effect responsible for the formation of residual stresses.

The above effect could explain the observed results, but in laser processing the surface cools last. In Chapter 3 it was stated that dendrites grow antiparallel to the maximum heat flow and it was described how the dendrites grew from the bottom and sides of the melt zone, with the surface solidifying last. After solidification heat flow into the bulk of the material continues. Results from a numerical model, produced by Mazumdar[70] and modified by Sharp[71], confirm this, with temperature differences of up to 500^{o}C being present in a vertical plane down the centreline of the track in the solid material directly behind the molten pool, with the highest temperature at the surface. This could be expected to lead to tensile stresses at the top of the melted zone and compressive stresses at the bottom. However, the stress measurements do not show this which would appear to confirm that little plastic deformation occurs at elevated temperatures in single laser tracks. The results produced by the model were in good agreement with experimental data.

4.8.6 Stresses in the melted zone

The contribution to the final stress profile of the stresses due to shrinkage during cooling is the same for all three specimens as they have all undergone the same time temperature history and hence cooled from the same temperature. This indicates that the differences which

exist between the final stress profiles of Specimens 1, 2 and 3 must be due to the transformation contributions.

The difference between the magnitude and sence of the transverse residual stresses in the melted zones of Specimens 1 and 3, the fully martensitic and the austenitic specimens, is quite dramatic. From about -20 to -450 MPa in Specimen 1 to between about +20 and +160 MPa in Specimen 3. This difference is caused by the 3% volume expansion experienced by the melted zone in Specimen 1 when it undergoes the austenite to martensite transformation, leading to the large compressive stresses measured.

The difference between the transverse stresses in the melted zones of the fully martensitic and partially martensitic specimens, Specimens 1 and 2, is much smaller than the difference between Specimens 1 and 3 described above. The transverse stresses in the melted zone of Specimen 2 are between about 0 and -200 MPa. Though the percentage of the molten zone transforming to martensite, estimated to be approximately 50%, is less than that for the fully martensitic specimen, it does so at a lower temperature. This is caused by the lowering of the M_s due to the increase in the carbon content. The significance here is that the yield stress of both austenite and martensite is greater at a lower temperature (ref. Section 4.2.3) and this may lead to a greater contribution from the incomplete transformation than expected.

4.8.7 Stresses away from the melted zone

The distances over which the stresses caused by laser processing are very large when compared to the diameter of either the melted zone or incident laser beam.

Figure 4.11 shows the thermal transients at the surface of an AISI 420 steel being heated by an incident laser beam of 1.6 kW and 2.0mm diameter, traversing the specimen at $10mms^{-1}$. These were calculated using a numerical model produced by Mazumdar[70] and modified by Sharp[71]. It can be seen that no material beyond 1.3mm from the centreline of the beam will undergo the martensitic transformation and that material more than 2.0mm from the centreline of the beam is not greatly affected. Therefore, the stresses measured in the specimens further than 2.0mm from the centreline of the melted zones must be a combination of stresses introduced into the specimen and balancing stresses to maintain the mechanical equilibrium of the sample.

4.8.7.1 Explanation of the general trends

Figure 4.12 shows a schematic representation of superimposition of transverse residual stresses due to shrinkage, quenching and phase transformation formed after welding[68]. This schematic in its present form is not suitable for application to laser surface treatments of metal for two reasons. Firstly, the heat input in welding is generally much greater leading to slow cooling rates (electron beam welding being an exception). Secondly, laser surface treatment of metals is not, as the name implies a through thickness technique, and this leads to differences in the way in which heat is dissipated.

Because of these differences between welding and laser surface melting/alloying a new schematic was drawn up for both the transverse and longitudinal stresses, Figure 4.13 and 4.14 respectively. As discussed earlier transformation plasticity and deformation at elevated temperature play minor roles in the "build-up" of residual stresses on cooling. Therefore, the problem was regarded as one of direct super-imposition of the contributions to the final stress profile due to shrinkage on cooling and phase transformations.

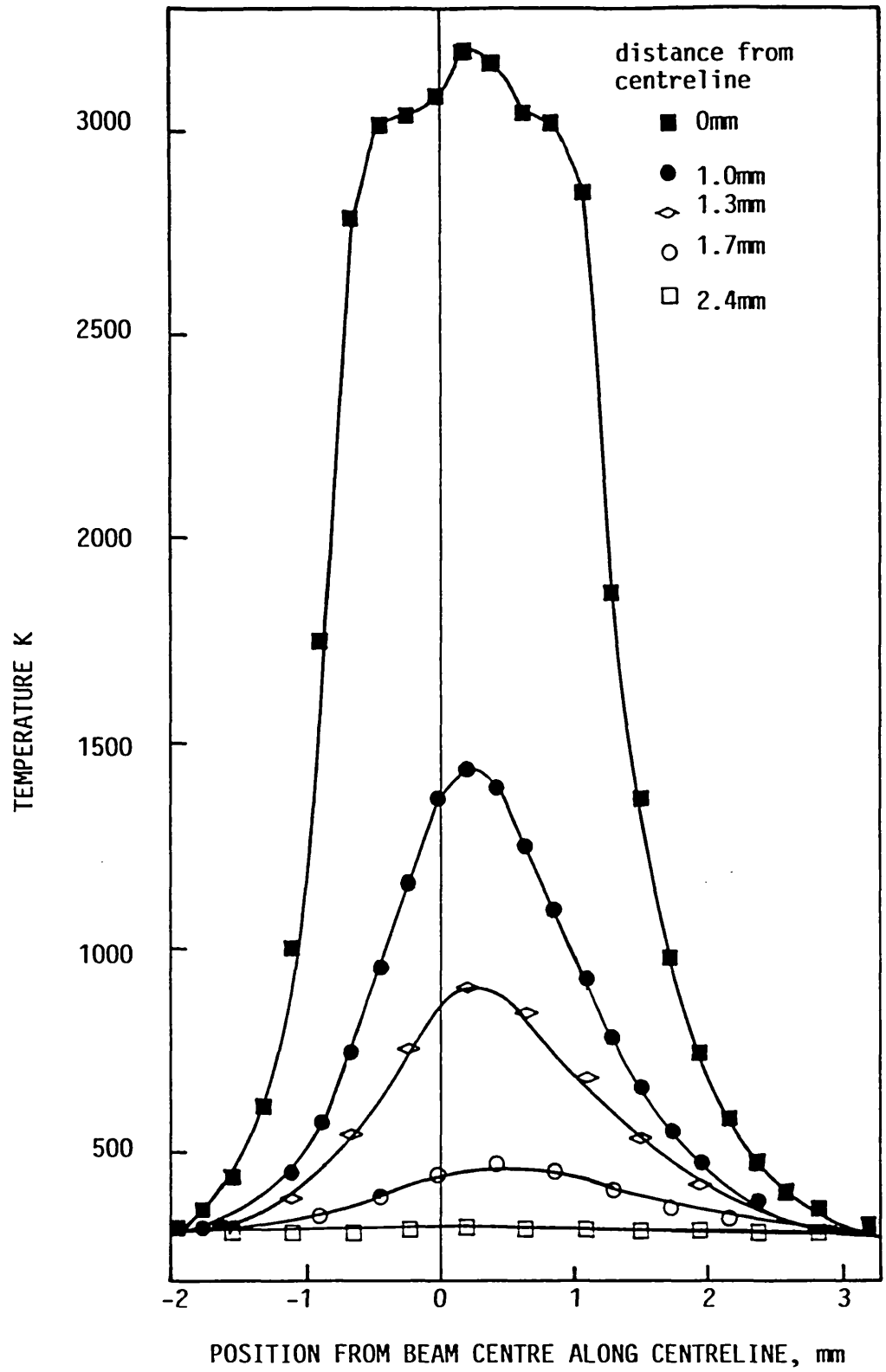


FIGURE 4.11

Thermal transients at the surface of parent material processed with P=1.6kW, D=2.0mm $V=10mms^{-1}$. Direction of laser travel is from right to left

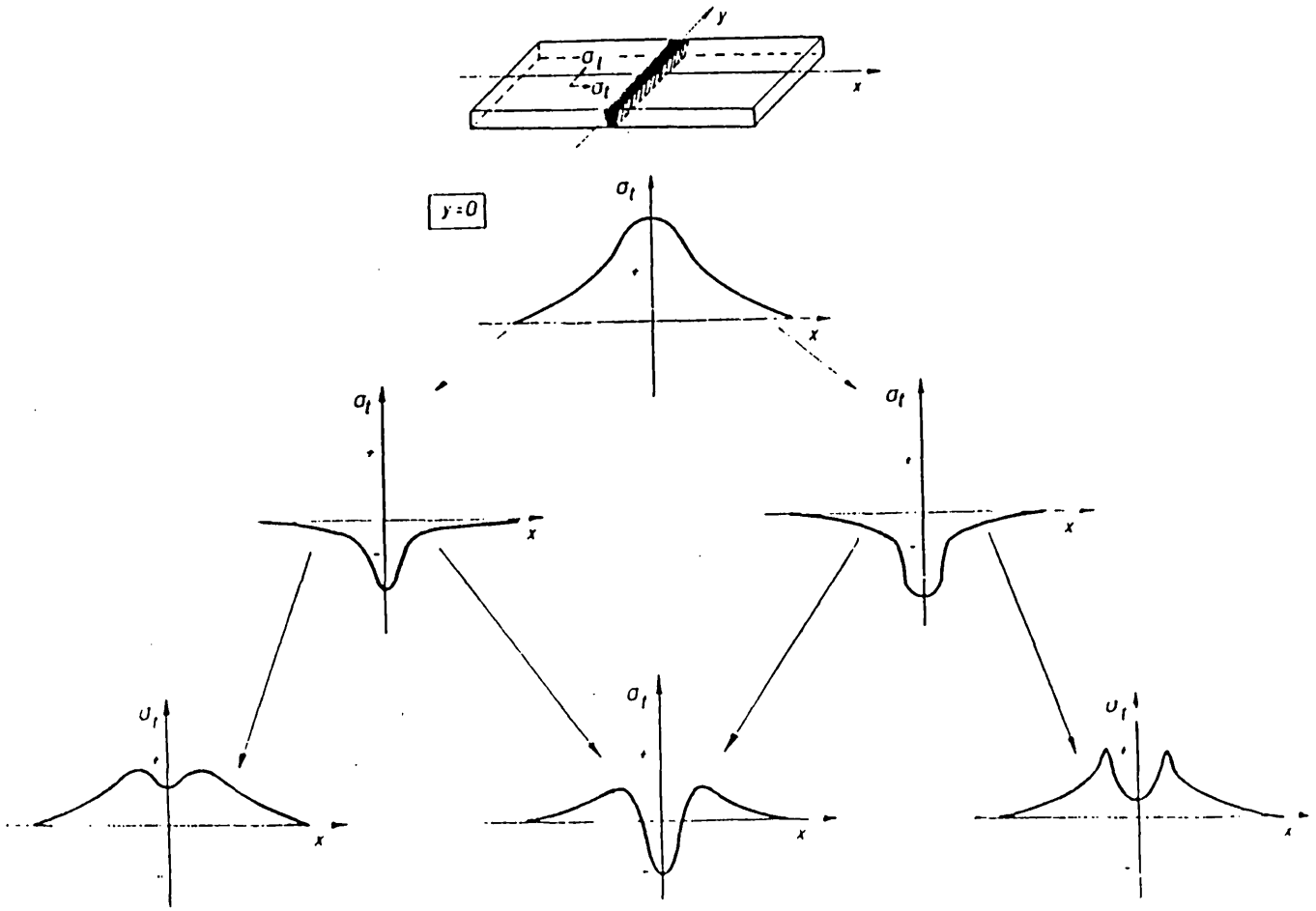


FIGURE 4.12

Schematic representation of superimposition of transverse residual stresses owing to shrinkage, quenching, and transformation. Top: shrinkage residual stress; Centre: quenching and transformation residual stresses respectively; Bottom: superimpositon of shrinkage and quenching, and transformation residual stresses (centre), and shrinkage and transformation residual stresses (right)[68]

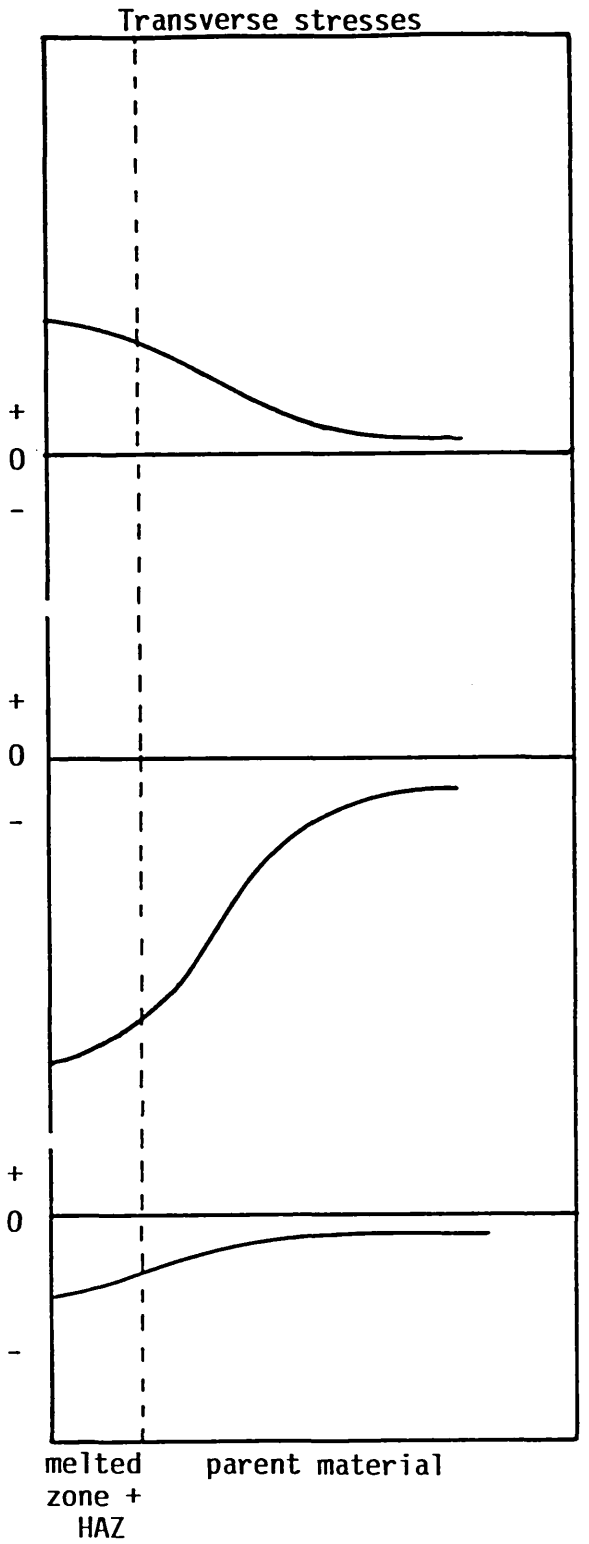


FIGURE 4.13

Schematic representation of transverse residual stresses owing to shrinkage and phase transformation. TOP: Shrinkage residual stress; MIDDLE: Transformation residual stress; BOTTOM: Shrinkage and transformation residual stresses

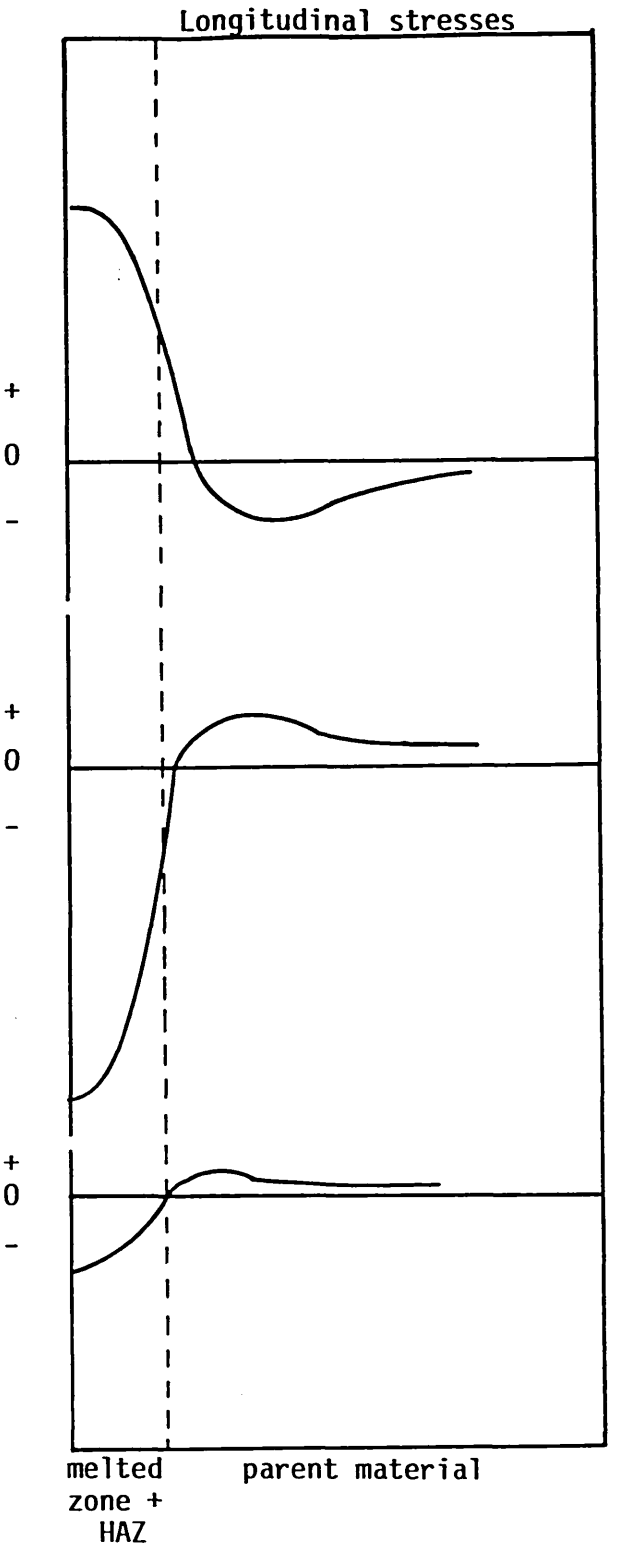


FIGURE 4.14

Schematic representation of longitudinal residual stresses owing to shrinkage and phase longitudinal. TOP: shrinkage residual stress; MIDDLE: Transformation residual stress; BOTTOM: shrinkage and transformation residual stresses

4.8.7.2 Transverse stresses

Figure 4.13 shows the schematic representation of the transverse residual stress "build-up" owing to shrinkage and transformation residual stresses. The general shape of the final stress profile is similar to those found in Figure 4.4 which shows the transverse stress profiles in the fully martensitic specimen. However, the large compressive stresses observed in the austenitic sample, Figure 4.8, especially away from the melted zone were not anticipated as there is no phase transformation causing an expansion and thus no reason for their presence.

4.8.7.3 Longitudinal stresses

Figure 4.14 shows the schematic representation of the longitudinal residual stress "build-up" owing to shrinkage and transformation residual stresses. There appears to be considerable deviation from the schematic by the stresses measured in the martensitic sample, Figure 4.5 compared to the schematic Figure 4.14. However, due to the course lateral spacing between the measuring points it is impossible to determine whether or not the stresses are oscillating about an average stress contour which follows that predicted by the schematic. This oscillation of the stresses has been observed by workers in the field of residual stress measurement e.g. Macherauch[48]. The compressive stresses observed in the austenitic sample, especially in the melted zone were not anticipated and again no explanation given.

4.9 Conclusions

1) The transverse residual stresses developed in single laser alloyed/melted tracks on 420 stainless steel varied between large and compressive (>-400 MPa) and smaller but tensile (200 MPa).

2) The longitudinal residual stresses displayed similar trends but were smaller in magnitude (-200 MPa to 50 MPa).

3) The compressive stresses were caused by the volume expansion during the austenite to martensite transformation; thus the stresses were dependent to a degree on the carbon content of the tracks, because of its effect on the M_s.

4) The stresses, in both directions, at the surfaces of the tracks tended to be more compressive than those within the tracks.

5) Plastic deformation at elevated temperatures played a minor role in the accumulation of residual stresses in the laser tracks during cooling.

6) Transformation plasticity played a minor role during the stress accumulation of those tracks that transformed to martensite, on cooling.

CHAPTER 5

EROSION

5.1.1 Introduction

420 stainless steel is used in the power generating industry in environments where it is susceptible to water droplet impact erosion. To simulate this under laboratory conditions requires expensive equipment. Cavitation erosion of a stationary specimen in close proximity to an oscillating source in a liquid was a more convenient and cheaper method of reproducing the effects of water droplet impact erosion.

It was first suggested by Kornfeld and Suvorov[72] in 1944 that cavities in a liquid might collapse in a non-symmetrical way, resulting in the formation of a liquid jet. This will occur for cavities in a pressure gradient field, produced for example, by other cavities collapsing. The presence of a solid surface near the collapse centre will cause the formation of a jet directed towards the surface. Experimental verification of this was obtained by Naude and Ellis[73] in 1961 and Lauterborn and Bolle[74] in 1975. It is known that a collapsing bubble emits a pressure wave of magnitude $\sim 10^3$ MPa into a surrounding liquid[75], but this wave is attenuated within a distance of the order of the initial radius of the bubble[76]. Consequently, it has been concluded that only those bubbles adjacent to the solid, about 1 in 30,000 of the total number[77] are able to cause any erosion damage. These observations led to the conclusion that cavitation and liquid impact erosion were essentially the same phenomenon.

5.1.2 Mechanisms of Erosion

The curve drawn in Figure 5.1 of mass loss against time of exposure is typical of that expected for an erosion test of either the water droplet impact or cavitation type.

This sigmoidal curve is often considered to represent three stages of erosion, designated primary secondary and tertiary as illustrated. During the primary stage, which may include an incubation period, the erosion rate increases slowly. This is followed by the secondary stage during which the erosion rate increases more rapidly to a maximum value after which it falls again towards a more constant value in the tertiary region.

During the incubation stage mentioned earlier, where no measurable loss of material is noted, plastic deformation of the material surface is occurring. The loss of material arises once fatigue processes have proceeded to a point where surface failure can occur. The plastic deformation eventually causes microscopically small pits to form. Longer exposure times result in more widespread damage and a deepening of the previously shallow pits.

Metallographic and X-ray diffraction studies have shown plastic deformation in the form of twinning and slip to occur in a layer about 30-300μm below the surface during the initial stages of damage[78,79]. This layer remains fairly constant throughout the subsequent stages of material removal. Material appears to be lost by ductile fracture of asperities in the early stages of the erosion process with fracture of work hardened material

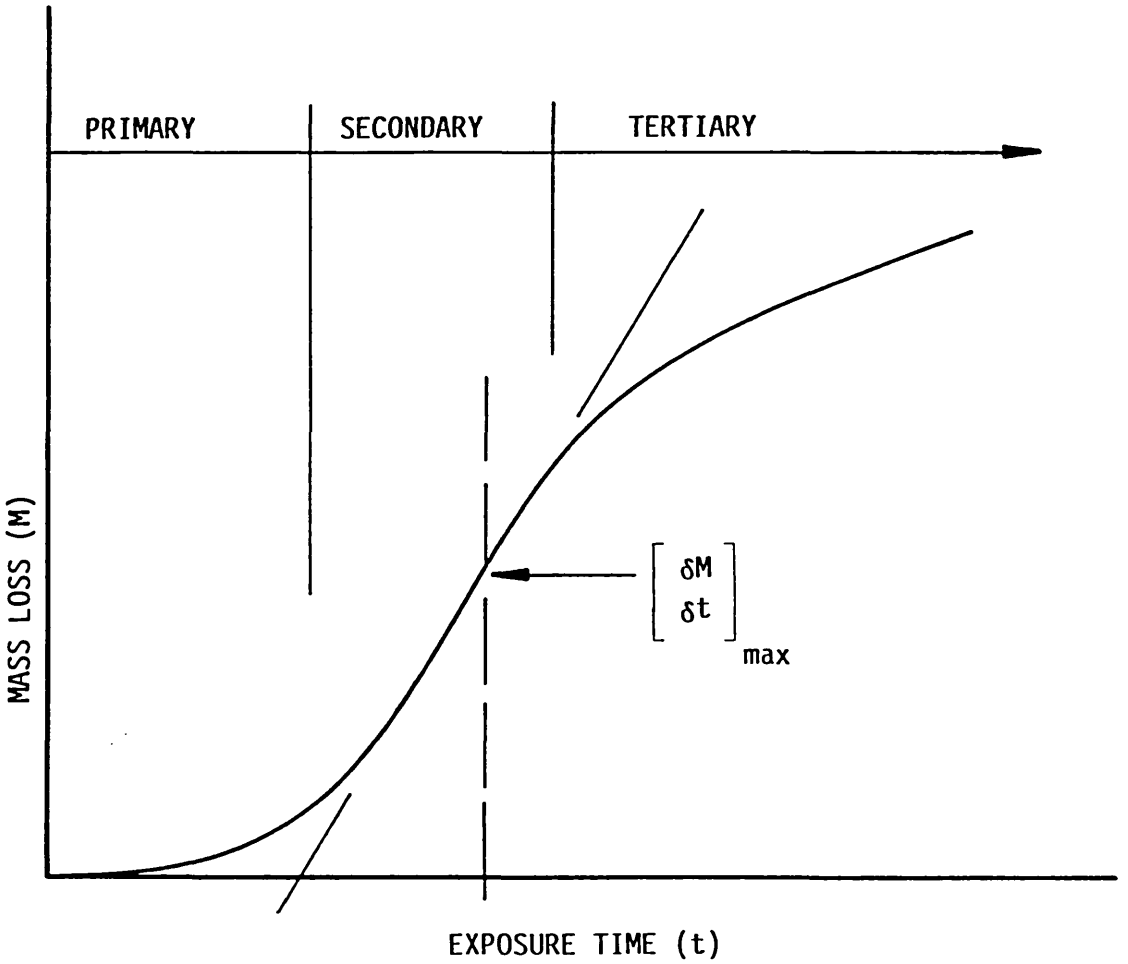


FIGURE 5.1

Typical mass loss against time of exposure curve, with divisions of primary, secondary and tertiary stages shown. (Linear co-ordinates)

and of ridges between erosion pits predominating in later stages.

5.1.3 Damage resistance of metals

Cavitation rates depend strongly upon material properties and although a wide range of properties have been considered including yield strength, U.T.S. ductility, strain energy, fatigue life, ultimate resilience, hardness, and various combinations of these, no simple relationship has been observed[80]. Historically hardness has been used as the best indicator of cavitation of liquid impact resistance[81,82]. However, hardness is only a good index of erosion resistance when the same alloy or very similar alloys are considered, as a small grain size and a fine dispersion of hard second phase particles will enhance erosion resistance. These characteristics, particularly the latter appear to give Stellites, a family of Co-Cr-W alloys their outstanding resistance to erosion with low hardness.

5.2 Experimental

5.2.1 The apparatus

Cavitation was produced in distilled water by a Lucus Dawe ultrasonic "Soniprobe 400". The device consists of a piezoelectric crystal oscillating at a resonant frequency of 20KHz attached to which is a stepped horn made of titanium, with a tip diameter of 19mm which amplifies the amplitude of vibration. When the horn is immersed in a liquid a cloud of bubbles is created and collapses with every vibratory cycle. Figure 5.2 shows a schematic of the experimental apparatus. The specimens were inserted and clamped into the holder, within the watertight container. The container was then raised by means of a laboratory jack until the specimen was

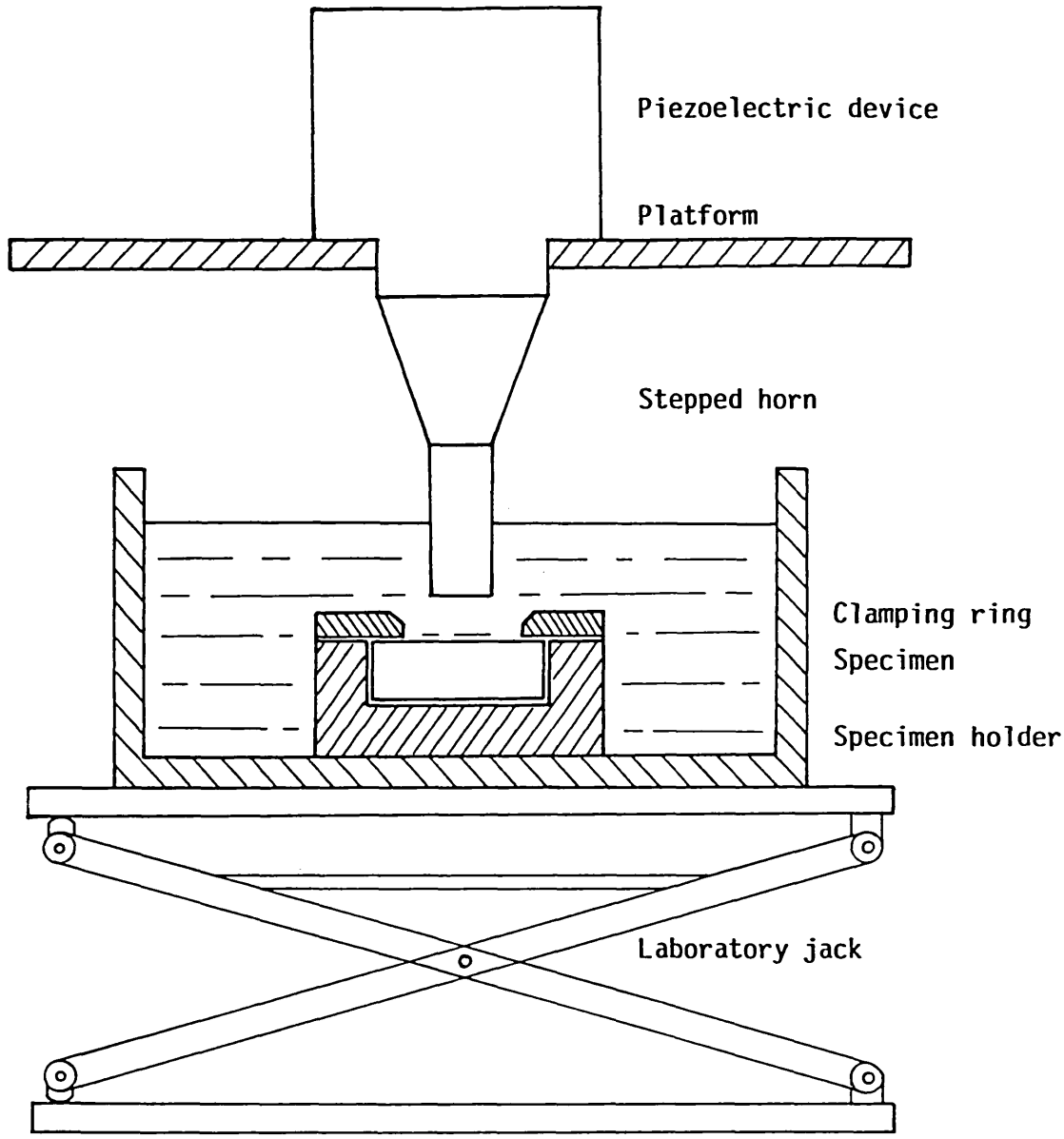


FIGURE 5.2

A schematic representation of
the experimental apparatus

0.5mm from the horn. This was achieved by using a "feeler gauge".

Before insertion of each specimen, its mass was measured using a chemical balance, accurate to 0.1mg and the surface roughness was measured with a Taylor-Holson Talysurf. Specimens were then removed at regular intervals to assess the mass loss and roughening of the surface. The erosion damage was inspected using both optical and scanning electron microscopy. To ensure that the specimen was always replaced accurately, a line was scribed onto the side of each specimen and this was aligned with one on the holder. Due to the time limitation, and the fact that to reach the tertiary stage of erosion would take many hundreds or thousands of hours, erosion tests were terminated once they were well into the secondary stage, usually after 30 hours.

5.2.2 The specimens

The specimens were 10mm thick discs, 32mm in diameter. In the case of the laser processed samples one face of the disc was completely covered by partially overlapping tracks, the treated face was then ground on silicon carbide paper (1200 grit) and polished using both diamond (6μm to 1/4μm) and alumina (0.05μm) polishing compounds until the surface roughness of the face was less than 0.005μm. This was also the condition of the surfaces of the specimens not given laser treatments. The beam conditions used for laser processing were 2.0mm diameter, a power of 1.6kW; and speed of traverse of 10 mms^{-1}; only the mass of the carbon coatings and the intertrack advance were varied. Table 5.1 describes the specimens tested, with the composition of the Stellite No 6 specimen given in Table 5.2. The stellite sample was included to give a comparison against which to gauge the results of the laser processed specimens as stellite is an alloy used commercially in conditions where erosion resistance is required.

TABLE 5.1

The Erosion Specimens

Specimen	Mass of carbon coating, $x10^{-6}$ gmm^{-2}	Intertrack advance, mm
A	4.6	0.5
B	4.3	0.5
C	4.4	1.5
D	4.8	1.0
E	11.0	0.5
F	12.9	1.0
G	10.1	1.0

T	420 steel oil quenched from 960°C and tempered at 760°C for 1 hour
Q	420 steel oil quenched from 960°C
S	Stellite No. 6 as-cast

TABLE 5.2

Composition of Stellite No. 6

Element, weight percent

Cr	W	C	Mo	Mn	Fe	Si	Ni	Co
28-32	3.5-5.5	0.9-1.4	1.5 max	2.0 max	3.0 max	2.0 max	3.0 max	Bal

required.

5.3 Results

5.3.1 Erosion data

Figure 5.3 shows the relationship between time of exposure and mass loss for the different specimens shown in Table 5.1. For all specimens, the plots show that after a primary stage there is a straight line relationship between the mass loss and time of exposure in the secondary state. No specimen reached the tertiary stage, not even the tempered sample, which after 26 hours exposure had lost 260mg. Not all the primary stages, which included an incubation period, are shown in Figure 5.3 in order to lend it clarity. However, the lengths of the primary stages are shown in Table 5.3 together with the surface hardness of each specimen.

TABLE 5.3

Specimen	Length of primary stage (hours)	Hardness Hv
T	1	220
Q	4	550
A	5	600
B	6	652
C	6	700
D	7	809
E	8	924
F	11	920
G	10	926
S	11	460

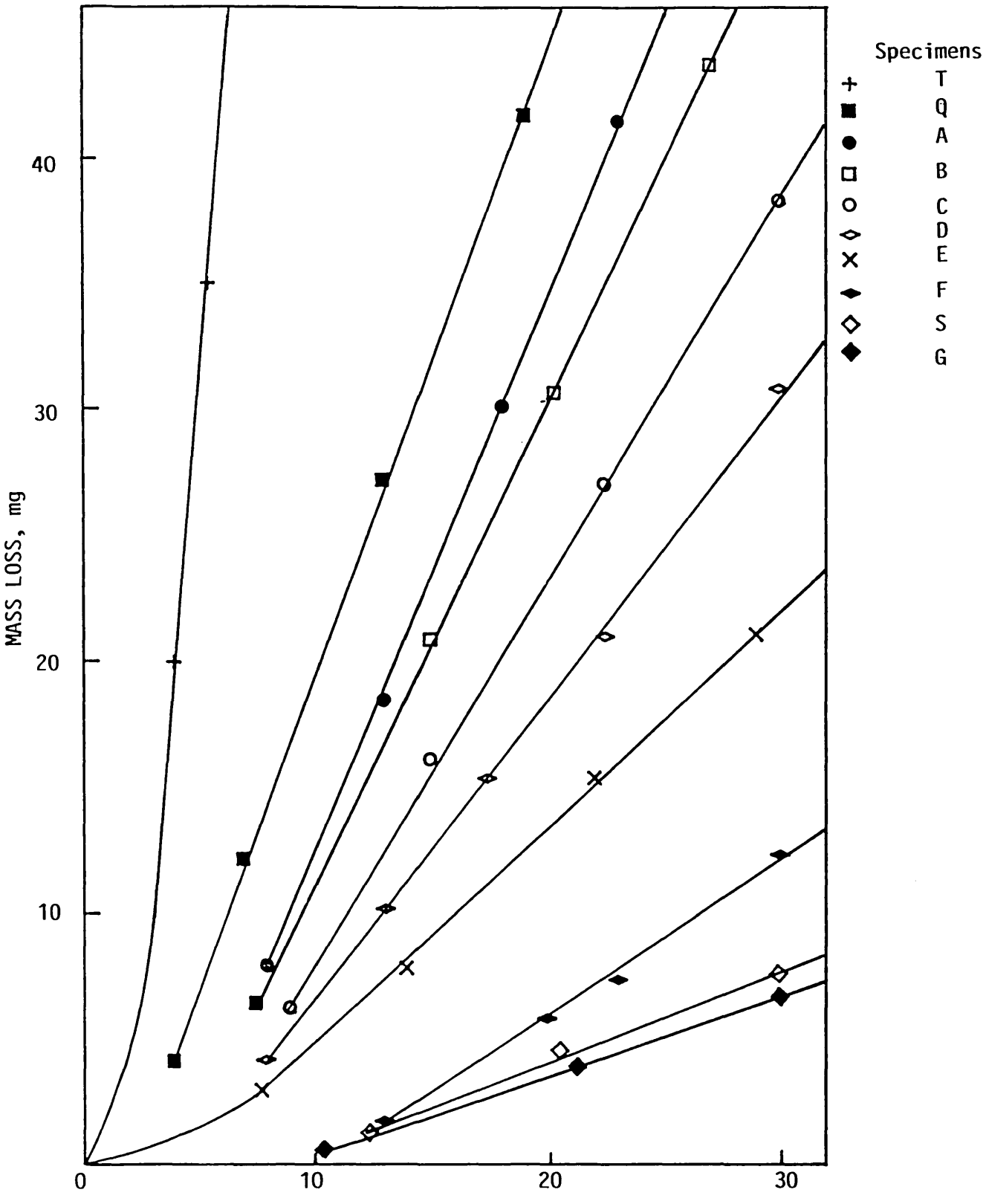


FIGURE 5.3

Mass loss against time for specimens shown in Table 5.1

From Table 5.3 it can be seen that the length of the primary stage appears to be proportional to the hardness of the specimen surface. The only exception to this is Specimen S, the stellite sample.

The rate of erosion in the secondary stage is equal to the gradients of the slopes shown in Figure 5.3. Table 5.4 shows the rates of erosion in the secondary stage obtained from Figure 5.3, together with the average hardness of the specimen.

TABLE 5.4

Specimen	Rate of erosion mg/hour	Hardness Hv
T	10.70	220
Q	2.37	550
A	2.18	600
B	2.00	652
C	1.52	700
D	1.17	809
E	0.85	924
F	0.62	920
G	0.25	926
S	0.35	460

This information is represented in graph form in Figure 5.4 with mass loss per hour plotted against hardness. It shows that there is an inverse relationship between them which is almost linear. The general trend, ignoring the stellite sample, is for the mass of material lost after a given time to decrease with increasing hardness, which tends to increase with increasing mass of carbon coating prior to laser treatment, Table 5.1.

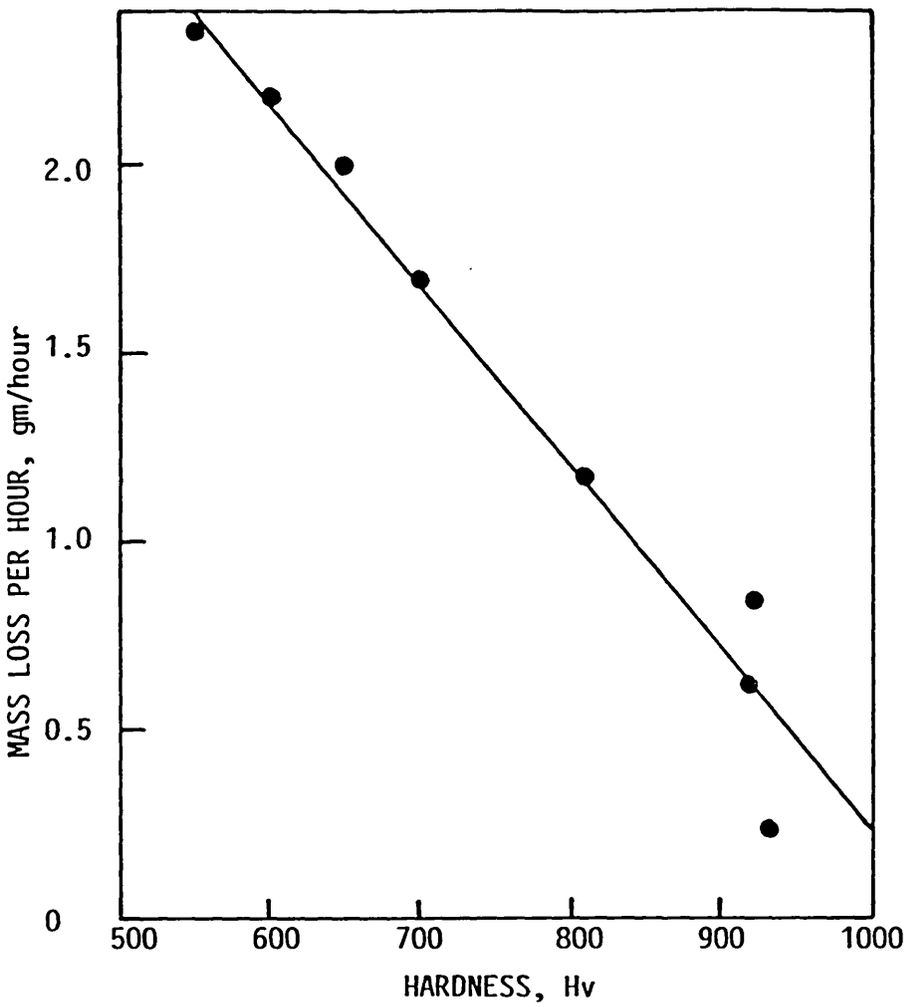


FIGURE 5.4

Mass loss per hour against hardness

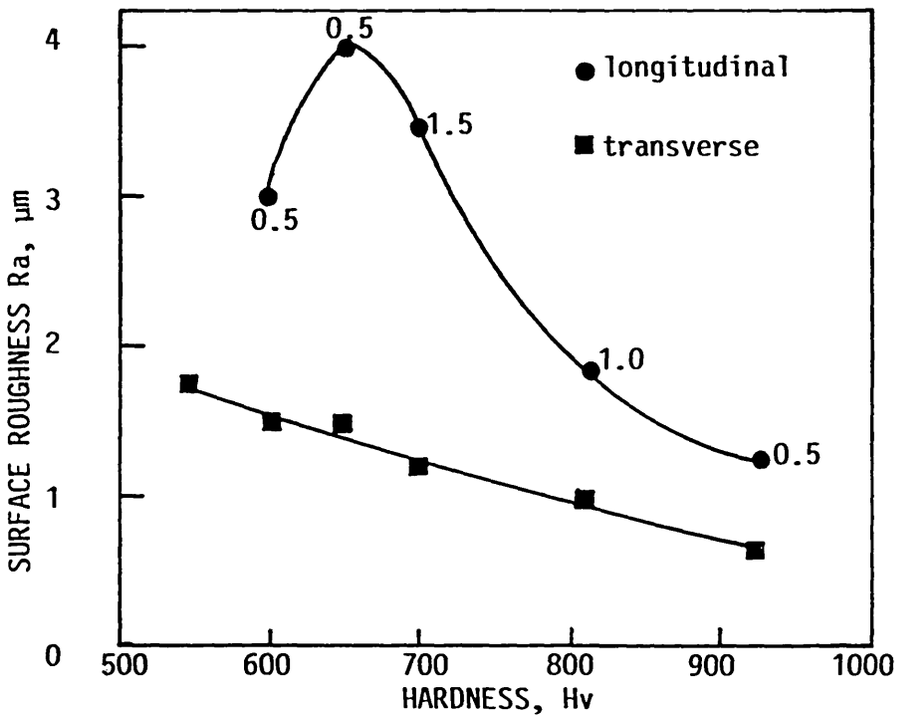


FIGURE 5.5

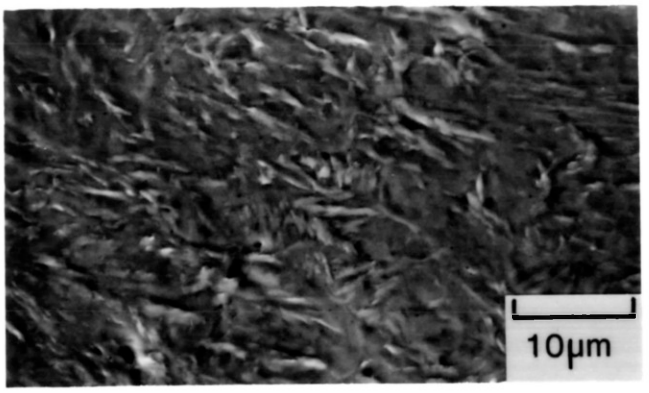
Final surface roughness against hardness, with intertrack advance (mm) indicated

Both Figures 5.3 and 5.4 show that all the laser treated samples are more resistant to erosion than the conventionally quenched material, together with the fact that Specimen G displays marginally superior resistance to erosion than the stellite sample which is renowned for its erosion resistance.

5.3.2 Damage to the specimens

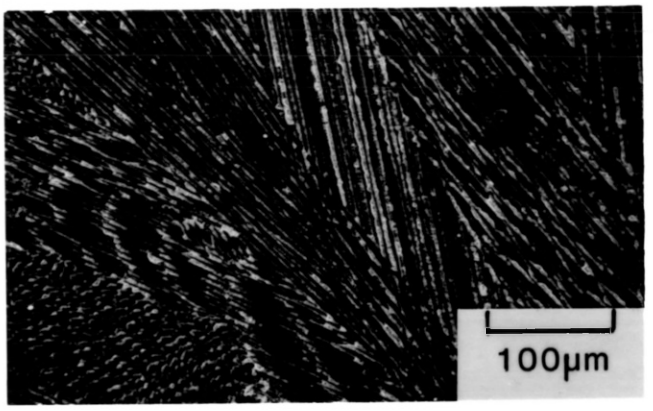
Initial cavitation damage in the incubation stage resulted in plastic deformation leading to the surface taking on a rumpled appearance. This topographical effect appeared to reveal the martensitic nature of the microstructure, as shown in Photograph 5.1 which was taken of Specimen A after 1 hour of exposure. As it was in the incubation stage no mass loss was noted. Further exposure caused deliniation of cell boundaries so that the microstructure could be observed. Photograph 5.2 shows dendritic or cellular alignment whilst Photograph 5.3 shows cells, of about 5μm diameter, at a higher magnification. Photographs 5.2 and 5.3 were taken after Specimen A had been exposed for 3 hours. This deliniation of the cell boundaries appears to have been caused by pits initiating in the cell boundaries, after the surface has become rumpled as shown in Photograph 5.4. At this stage there was some mass loss. The pits then grew as shown in Photograph 5.5. Photographs 5.4 and 5.5 were taken of Specimen E after 2 and 3 hours respectively.

Pits then initiated in the dendrites. Photograph 5.6 shows Specimen E after 7 hours exposure, and it can be seen that some dendritic material has remained undamaged (the dark material). These pits then grew until the entire surface was covered, signifying the end of the primary stage. Photograph 5.7 is of Specimen A after 8 hours, just before the end of the primary stage, showing an extensively damaged region with some undamaged areas remaining. Once the entire surface was



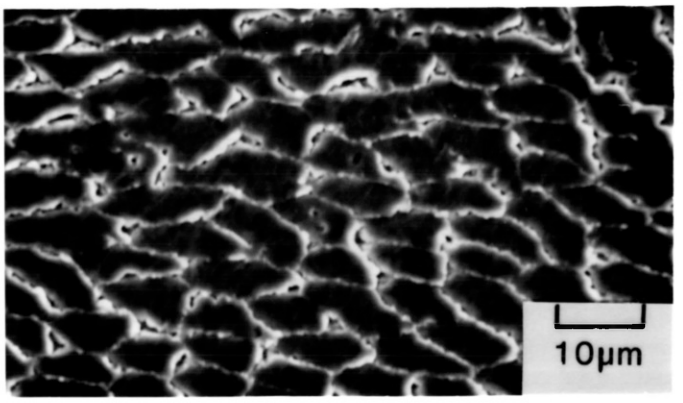
PHOTOGRAPH 5.1

Specimen A after 1 hour
of exposure



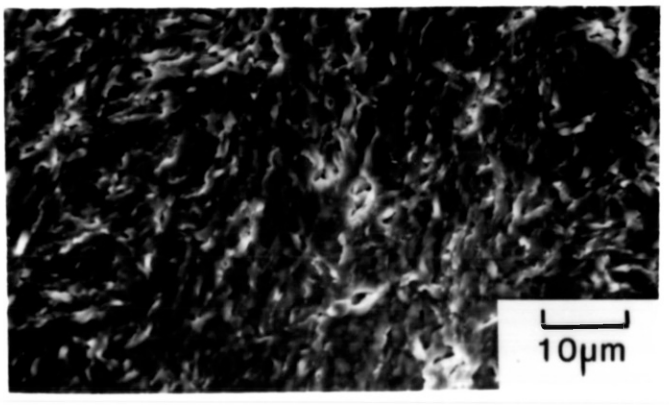
PHOTOGRAPH 5.2

Specimen A after 3 hours
of exposure



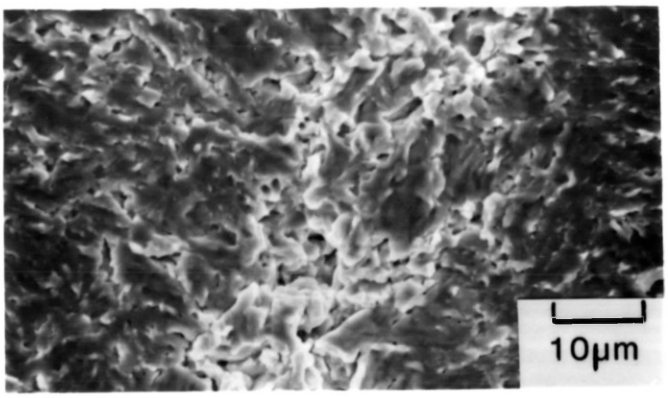
PHOTOGRAPH 5.3

Specimen A after 3 hours
of exposure



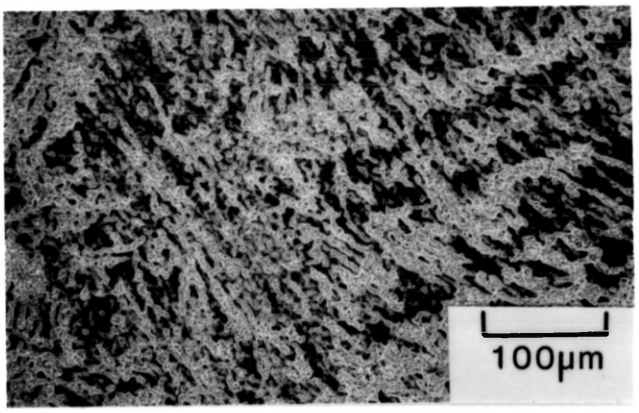
PHOTOGRAPH 5.4

Specimen E after 2 hours
of exposure



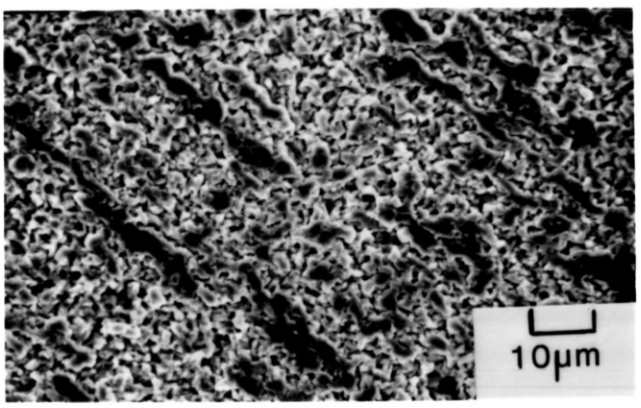
PHOTOGRAPH 5.5

Specimen E after 3 hours of exposure



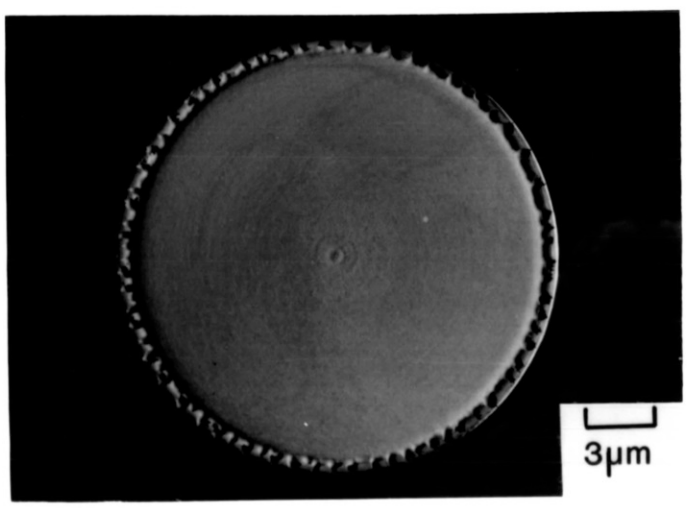
PHOTOGRAPH 5.6

Specimen E after 7 hours of exposure



PHOTOGRAPH 5.7

Specimen A after 8 hours of exposure



PHOTOGRAPH 5.8

The horn tip after a 30 hour test

damaged no focussing of the cavitation was noted and the damage remained uniform over the surface with no abnormally large pits forming. The time of exposure required by each specimen to reach the stages described above will vary, according to its hardness.

The final surface roughness measurements both longitudinal and perpendicular to the direction of laser travel, plotted against hardness are shown in Figure 5.5. Apart from the spurious longitudinal result at a hardness of ~650 Hv, the surface roughness in both directions decreases with increasing hardness. The degree of intertrack advance has little effect.

Hardness testing on the erosion damaged surfaces was carried out after the 30 hour tests to determine whether or not any increase in hardness due to work hardening had occurred. However, the uneven surface made accurate hardness measurements impossible to obtain.

5.3.3 Damage to the horn

Damage to the horn tip was observed which seemed to concentrate itself near to the circumference of the tip. Photograph 5.8 shows the damage caused by 30 hours of cavitation. The damage was machined off before the start of each 30 hour test. The pitting was typically ~250μm in depth. It was also noted that the damage incurred by the tip was greatest for specimens which showed the greatest resistance to erosion. No quantitative data is available.

5.4 Discussion

5.4.1 Erosion data

The plots in Figure 5.3 show the initial stages of a sigmoidal curve, typical of a mass loss against time curve for

a cavitation erosion test. The length of time associated with the primary stage appears to be directly proportional to the hardness of the specimen surface; the harder the surface, the longer the primary stage, Table 5.3. The gradient of the secondary stage, however, appears to be inversely proportional to the hardness; the harder the surface the smaller the gradient of the secondary stage, Figure 5.4.

Hardness or microhardness is often cited as a measure of erosion resistance[81,82,83], and the above observations indicate that there is a general increase in erosion resistance with increasing hardness, irrespective of intertrack advance, thus the results are as expected.

5.4.2 The specimens

The undulated or rumpled nature of the specimen surfaces before material loss has been noted, as observed by other workers. Vyas and Preece[72] found that simple F.C.C. metals, Al, Cu and Ni underwent plastic deformation in the early stages of cavitation erosion whilst Vaidya et al[79] also noted the effect in some age hardenable aluminium alloys. McGuire[84] tested 420 steel in both the quenched and the quenched and tempered conditions by water droplet impact erosion and also observed the rumpling of the specimen surface. This appears to confirm the similarity between cavitation and water droplet impact erosion in the early stages.

The fact that pits are initiated in the interdendritic eutectic could be due to the weak interlamellar interfaces succumbing to the extremely high shear stresses associated with the jetting action following the collapse of a cavity. Other workers, such as Heathcock et al[83] and Karimi[85] have found that the boundaries between two phases (austenite and ferrite) and the interfaces between carbides and the matrix

have proved to be good initiation sites for erosion damage.

Heathcock et al[83] tested two martensitic stainless steels under cavitation erosion conditions. The compositions of the steels are given below.

	Alloying elements wt%						
Alloy	**C**	**N**	**Mn**	**Si**	**Cr**	**Ni**	**Mo**
BS431S29	0.11	-	1.0	0.8	15.6	2.34	-
DIN 4112	0.91	-	1.0	1.0	18.5	-	1.15

The specimens were oil quenched from 1040^{o}C and tempered at various temperatures. It was found, predictably, that the erosion resistance of the hardened and tempered steels was dependent upon the hardness of the test specimens. The DIN 4112 samples were found to have the greatest erosion resistance, due to the higher carbon content of this alloy resulting in its martensitic matrix having a higher hardness than the BS431S29 alloy. However, the high carbon content of the DIN 4112 samples led to the formation of coarse chromium carbides which provided initiation sites for the erosion damage.

Karimi[85] working on cavitation erosion of a duplex (austenite + ferrite) stainless steel found that material removal started from the most favourable sites. In the duplex stainless steel these were the austenite-ferrite boundaries.

McGuire[84] found that the erosion resistance of the 420 steel decreased with decreasing hardness. It was also found that inclusions played an important role in damage initiation of the 420 steel when exposed to water droplet impact erosion, with the weak inclusion-matrix

interface providing the initiation site. It was also noted that other surface irregularities, such as scratches, were found to be initiation sites. One advantage of laser melting or alloying the 420 steel is that inclusions are unlikely to occur due to the high cooling rates which lead to high solidification rates.

Surface defects were unlikely to affect the results obtained in the present work due to the high quality surface finish given to each specimen prior to erosion testing. However, it would be of interest to repeat the experiments on the as-laser treated surfaces to determine what effects, if any, the laser processing conditions may have on the erosion resistance, due to surface topography effects.

5.4.3 The horn tip

The fact that the tip of the stepped horn suffered greater damage when vibrating close to more erosion resistant specimens, agrees with observations by Kikuchi and Hammitt[86]. They studied vibrating cavitation erosion with vibrating and stationary specimens, the vibrating specimens being attached to the end of the vibrating tip. Three materials were investigated, commercially pure lead, soft (1100.0) aluminium and AISI type 316 stainless steel. The mass loss of both vibrating and stationary specimens was determined. An aluminium vibrating specimen was paired with a lead stationary specimen and then a type 316 stainless steel specimen. It was found that the mass loss of the aluminium vibrating sample was 2 to 5 times higher when paired with the steel sample than when paired with the lead stationary sample under identical testing conditions. However, no explanation was given as to why this phenomenon occurs.

5.5 Conclusions

1) Laser surface alloying of 420 stainless steel with carbon can greatly enhance the erosion resistance of the steel.

2) The erosion resistance of the 420 steel specimens is dependent upon hardness.

3) All the laser treated samples were more erosion resistant than the conventionally quenched sample.

4) The degree of intertrack advance is of little consequence to the erosion resistance.

CONCLUSIONS

Structures

Laser surface alloying of 420 stainless steel with carbon can produce hard, macroscopically smooth tracks and surfaces suitable for most engineering applications without the need for a further finishing process e.g. grinding. Exceptions to this would be bearing surfaces which require exceptionally smooth finishes.

High levels of carbon (> 4 wt% C) can be introduced into the surface of 420 stainless steel in a controlled manner. The hardness increased with carbon content up to ~900 Hv, associated with martensite formation; increasing austenite retention with further increase in carbon led to lower hardness values, down to ~500 Hv until a hardness increase (up to ~1500 Hv) occurred as carbide appeared beyond the solubility limit. Structures beyond the solubility limit suffered from cracking and porosity. Slow transverse rates (< 10 mms^{-1}) favoured the production of homogeneous melted zones for all carbon coatings, whilst the lighter the coating the faster the transverse rate at which homogeneous melted zones could be produced.

The rapid cooling rates associated with laser processing, up to ~$6x10^4$ $^oCs^{-1}$ in the liquid state produced fine structures with cell and secondary dendrite arm spacings between approximately 3 and 0.6 μm.

Surface roughness measurements of single tracks showed that longitudinally the roughnesses varied between 0.7 and 7.0 μm (normally between 0.7 and 5.0μm) and across the tracks was always less than 1μm. On partially overlapping tracks the surface roughnesses varied between

0.7 and 5.0 μm longitudinally and between 2.0 and 5.0 μm across them.

Residual Stresses

The X-ray diffraction method of measuring residual stresses was used to take stress measurements in the longitudinal and transverse directions, in and adjacent to three laser melted/alloyed tracks at varying depths. The carbon contents of the three melted zones were different, with the structures being fully martensitic, partially martensitic/austenitic and almost fully austenitic. The stress results showed complex patterns.

The transverse stresses developed in the melted zones at different depths varied between approximate values of -400 and -20 MPa in the fully martensitic sample, between -200 and 0 MPa in the partially martensitic sample and between -50 and +200 MPa in the austenitic sample.

The longitudinal stresses developed in the melted zones at different depths were approximately -150 MPa in the fully martensitic sample and varied between approximate values of -150 and +50 MPa in the partially martensitic sample and -180 and +20 MPa in the austenitic sample.

The stresses at the surfaces of the tracks, in both directions tended to be more compressive than those within the tracks.

The compressive stresses are caused by the volume expansion associated with the austenite to martensite transformation, and thus the stresses were dependent upon the carbon content of the melted zone: the higher the

carbon content of the melted zone: the higher the carbon content, the lower the M_s, therefore less martensite forms and thus the more tensile and the less compressive the stresses.

Plastic deformation at elevated temperatures plays a minor role in the stress accumulation of the laser tracks during cooling.

Transformation plasticity plays a minor role during the stress accumulation, of those laser tracks that transform to martensite, on cooling.

Erosion

Cavitation erosion tests were carried out using an ultrasonically vibrating probe, immersed in distilled water in close proximity to a flat specimen.

It was found that laser surface alloying of 420 stainless steel with carbon greatly enhanced the erosion resistance of the steel. A fair correlation between the hardness of the specimen surface and erosion resistance was displayed. The degree of intertrack advance had no effect on the erosion resistance. All the laser treated samples were more erosion resistant than the conventionally quenched sample.

FUTURE WORK

The enhanced erosion resistance offered by laser surface alloying 420 stainless steel with carbon could be used in the power generating industry as a viable alternative to the current method of protecting components against water droplet impact erosions. However, before this could be achieved some fundamental work on processing 3-D specimens would have to be undertaken. A logical progression of the work would be to research into laser cladding of components manufactured from 420 stainless steel in order to repair damaged surfaces. The cladding material could either be the parent material, i.e. 420 stainless steel, which could then be laser surface alloyed or an erosion resistance material, such as a stellite.

More work is required to fully understand the accumulation of residual stresses after laser processing. Initially, work should involve measuring the stresses through the depth of and beyond the melted zone and HAZ, with the lateral spacing of the measuring points greatly reduced. After the above, work should be undertaken on partially overlapping tracks of varying degrees of overlap and varying degress of carbon content.

The corrosion behaviour of the single and overlapping surface should be studied as well as more fundamental work on the formation of martensite. There are many conflicting arguments about rapid solidification and its effect upon the martensitic transformation. The wide range of cooling rates made available by laser processing could be used to good effect with TEM.

REFERENCES

1) **Oakley, P.J.,** The Welding Inst Research Bulletin, Jan 1981, p22

2) **Hull, D.M. and Stewart, A.,** Lasers and Applications, Oct 1985, p75.

3) **Welch, M.,** Lasers and Applications, Jan. 1986, pp67-71

4) **Duley, W.W.,** "Laser Processing and Analysis of Materials", Plenum press, New York, 1976

5) **Lamb, M.,** Ph.D. Thesis, Imperial College, University of London, 1985

6) **Steen, W.M. and Courtney, C.** Materials in Engineering, Vol 2, No 3, March 1981

7) **Roth, M. and Cantello, M.** Conf. Proc. LIM 2, Birmingham, 1985, pp119-128

8) **Bedogni, V., Cantello, M., Cerri, W., Cruciani, D., Fest, R., Mor, G., Nenci, F., Vivoli, F.P.,** Conf. Proc. Laser Advanced Materials Processing (LAMP '87), Osaka, 1987, pp567-572

9) **Metal Progress,** 129 (5), 33, 1986

10) **Kear, B.H.,** SME Technical paper M.R., 76-867, 1976

11) **Anthony, T.R., and Cline, H.F.,** J. Appl. Phys. vol 49, no3, 1978, p1248

12) **Chen, Z.D., West D.R.F., and Steen, W.M.** Conf. Proc. 5th Inst. Congress on Applications of Lasers and Electro-optics. ICALEO '86, 10-13, Nov 86, Arlington, Virgina, USA, Edited by C.M. Banas and G.L. Whitney.

13) **Chen, Z.D.,** Ph.D. Thesis, Imperial College, University of London, 1988

14) **Steen, W.M., Chen, Z.D., and West, D.R.F.,** The Industrial Laser Handbook, 1987 Edition. Edited by D. Belforte and M. Levitt.

15) **Huberty, B., and Milmen, F.** Conf. Proc. European Conf. on Laser Treatment of Materials, 1986, Bad Nauheim, F.G.R., Edited by B. Mordike

16) **Draper, C.W. and Poate, J.M.**, International Metals Reviews, Vol 30, No 2, 1985, p85

17) **Walker, A., West, D.R.F., and Steen, W.M.**, Metals Technology, vol 11, Sept 1984, pp399-404

18) **Mordike, B.C., Bergmann H.W., and Grob, N.** Z. Workstofftech 14, 1983, pp253-257

19) **Weerasinghe, V.W.**, Ph.D. Thesis, Imperial College, University of London, 1985

20) **Das, S., Dumler, I. and Mazumdar J.**, Proceedings of 2nd International Conference on Lasers in Manufacturing. 26-28 March, 1985, Birmingham

21) **Moore P.G.**, SPIE, vol 198, Laser Applications in Materials Processing, 1980

22) **Molian, P.A.** Journal of Materials Science, 20, 1985, pp2903-2012

23) **Folkes, J.**, Ph.D. Thesis, Imperial College, University of London, 1987

24) **Katayama, S., Matsunawa, A., Moritimoto, A., Ishimoto, S. and Arata, Y.** Proc. Conf. ICALEO, Boston, USA, Nov 12-15, 1984

25) **Alexander, J.** Ph.D. Thesis, Imperial College, University of London, 1982

26) ANSI. Standard Z136.1, 1976, "For the Safe Use of Lasers", American National Standards Inst. New York, 1976

27) **Lim, G.C. and Steen, W.M.** Optics and Laser Tech., vol 6, 1982, p149

28) **Durnin, J. and Ridal, K.A.** Journal of The Iron and Steel Institute, Jan, 1968, pp60-67

29) **International Tables of X-ray Crystallography** Vol 4, pp72-98

30) **Cullity, B.D.**, "Elements of X-ray Diffraction", Addison and Wesley, 1956, pp107-143

31) **Southon, M.J., Witt, M.C., Harris, A. and Wallach, E.R.**, Vacuum, vol 34, no 10/11, 1984, pp903-909

32) **Walker, A., Flower, J.M., West, D.R.F.**, Journal of Material Science, vol 20, 1985, pp989-995

33) **Mordike, B.L., Bergmann, H.W. and Grob, N.** Z. Workstofftech 14, 1983, pp253-257

34) **Jones, H.,** "Rapid solidification of Metals", The Institute of Metallurgists, Monograph no8, 1983, pp40-43

35) **Bungart, K., Kunze, E., and Horn, E.,** Archiv. f. das. Eisenhuttenwesen, Marz, 1958, p193

36) **Thorpe, W.R. and Chicco, B.,** Met. Trans. A. 16A. 1985, pp1541-1549

37) **Rappaz, M., Gremaud, M., Dekumbis, R. and Kurz, W.,** Conf. Proc. Laser Treatment of Materials, 1986, Bad Nauheim, F.G.R., Edited by B. Mordike.

38) **Cohen, M., and Kear, B.H.,** Solidification Processing and Principles and Technologies II. Claitors publishing Div. Buton Rouge, L.A., 1980, Edited by R. Mehrabian et al.

39) **Kear, B.H., Breinan, E.M., and Greenward, L.E.** Metals Tech., vol 6, no4, 1979, pp121

40) **Walker, A.,** Ph.D. Thesis, Imperial College, University of London, 1986

41) **Walker, A.M., Lundberg, L.M., Hawkes, I., West, D.R.F. and Steen, W.M.** Int. Cast. Conf. II, Stockholm, aug, 1984

42) **Coriell, S.R. and Sekerka, R.F.,** Rapid Solidification Processing Principles and Technologies II, Claitors Publishing Div., Buton Rouge, L.A., 1980, Edited by R. Mehrabian et al

43) **Pickering, F.B.** International Metals Review. vol 21, 1976, p229

44) **Bee, J.V. and Wood J.V.,** Metal Science vol 16, 1982, pp268-274

45) **Molian, P.A.** Journal of Material Science. vol 20, 1985, pp2903-2012

46) **Ansell, G.S., Donachie, S.J. and Messler, R.W.,** Metall. Trans. vol 12, 1971, p2443

47) **Leslie, W.C., and Miller, R.L.,** Trans. ASM, vol 57. 1964, p972

48) **Macherauch, E., Wohlfahrt, H. and Wolfstieg, U.,** Zur Zweckmabigen Definition von Eigen Spannungen, H.T.M., 28, 1973, p201

49) **Harrison, J.D.,** "Residual Stresses and Their Effects", Welding Inst., London, 1981

50) **Harrison, J.D. and Leggatt, R.H.** ibid

51) **Dwight,** ibid

52) **Chastell, D., Doig, P., Flewitt, P.E.J. and Ryan, K.,** Corrosion Sci. vo 19, no5, 1979 p335

53) **Parlane A.J.A.,** "Residual Stresses and Their Effects", Welding Inst. London, 1981

54) **Easterling, K.,** "An Introduction to the Physical Metallurgy of Welding", Butterworths, 1983

55) **Jones, W.K.C. and Alberry, P.J.,** Conf. Proc. Residual Stresses in Welded Construction and Their Effects. Welding Inst., London, 1977

56) **Greenwood, G.W. and Johnson, R.H.,** Proc. Royal Soc., London, 283a, (1394), 403, 1965

57) **Anorg Z.,** Ally. Chem. 207, 21, 1932

58) **Clinard, F.W. and Sherby, O.D.,** Acta Met., vol 12, 1964, pp911-919

59) **Lamb, M., West, D.R.F., and Steen, W.M.,** Material Science and Technology, vol 2, 1986, pp975-980

60) **James, M.R., Gnanamutha, D.S. and Moores, R.J.,** Scripta Met. vol 18, no4, 1984, p357

61) **Cullity, B.D.,**"Elements of X-ray Diffraction", Chapter 16, Addison and Wesley, 1956

62) **Stokes, R., Lonsdale, D. and Doig, P.,** Industrial Diamond Review, no3, 1986, pp113-117

63) **Dallus, D.B.,** Tool and Manufacturing Handbook. McGraw Hill, 1976

64) **Marsden, C.F., West, D.R.F., and Steen, W.M.,** Conf. Proc. Lasers Advanced Materials Processing (LAMP '87), Osaka, 1987

65) **Barratt, C., and Massalski, T.B.,** "Structure of Materials", Third edition (revised) 1980

66) **Jubb, J.E.M.,** Metals Construction, vol 2, no10, 1970, p455

67) **Luxmore, A., Kan, D.K.Y. and Egan, G.R.,** Metals Construction, vol 2, no6, 1970, pp229-234

68) **Macherauch, E., and Wohlfahrt, H.,** Conf. Proc. Residual Stresses in Welded Construction and Their Effects, Welding Inst. London, 1977

69) **Kot, R.A., and Weiss, V.** Met. Trans. A., vol 1A, no10, 1970, p2685

70) **Mazumdar, J., Steen, W.M.,** J. Appl. Phy., vol 15 no2,1980

71) **Sharp, M.,** Ph.D. Thesis, Imperial College, University of London, 1986

72) **Kornfeld, M., and Suvorov, L.,** J. Appl. Phy. vol 15, June 1944, pp495-506

73) **Naude, C., and Ellis, A.T.,** J. Basic Eng. Trans. ASMF. Series D, vol 83, no4, Dec 1961 pp648-656

74) **Lauterborn, W., and Bolle, H.,** J. Fluid Mechanics, vol 72, 1975, p391

75) **Schulmeister, R.,** 1st Int. Conf. on Rain Erosion, 1965, p95

76) **Ivany, R.D.,** Tech. Rep., no15, Dept. Nucl. Eng., University of Michigan, 1965

77) **Knapp, R.T.** Trans ASME, vol 77, 1955, p1045

78) **Vyas, B., and Preece, C.M.,** Met. Trans. A, vol 8A, June 1977, pp915-923

79) **Vaidya, S., and Preece, C.M.** Met. Trans. A., vol 9A, March, 1978, pp299-307

80) **Hobbs, J.M. and McLoy, D.,** Metals and Materials, vol 6, 1972, p27

81) **Knapp, R.T., Daily, J.T. and Hammitt, F.G.,** "Cavitation", McGraw Hill, New York, 1970

82) **Hammitt, F.G. and Heymann, F.J.,** Metals Handbook, vol 10

83) **Heathcock, C.J. and Protheroe, B.E.,** Wear, vol 81, 1982, pp311-327

84) **McGuire, M.**, SE/SSD/82/R, 1982, CEGB, S.E. Region

85) **Karimi, A.**, Mat. Sci and Eng., vol 86, 1987, pp191-203

86) **Kikuchi, K., and Hammitt, F.G.**, Wear, vol 102, 1985, pp211-225

APPENDIX 1

LASER SURFACE ALLOYING 420 STEEL WITH NITROGEN

Introduction

For many years the nitriding of steels have produced engineering components with very hard wear resistant surfaces. Nitriding involves heating the component to between 450^{o}C and 600^{o}C in a nitrogenous atmosphere, usually "cracked" ammonia, to enable disassociated nitrogen to diffuse into the surface. However, it is undesirable, in some cases, to heat large components which have been machined to high dimensional tolerances as they may suffer from thermal damage and be ruined.

Laser surface alloying is therefore a way of solving this problem, as the overall heat input is low compared with conventional nitriding.

Folkes[23] has laser alloyed titanium with nitrogen by melting titanium with a continuous-wave CO_2 laser in a n atmosphere of oxygen free nitrogen to produce layers of TiN. Katayama et al[24] have CO_2 and pulsed yag lasers to produce TiN layers on titanium in an atmosphere of pure nitrogen.

Experimental

Initially, tracks were laser melted in an atmosphere of argon to act as a standard against which the laser alloyed structures could be compared. Oxygen Free Nitrogen (O.F.N.) was then supplied to the shroud and laser nozzle in place of the argon shown in Figure 2.2. with an additional gas jet placed so that O.F.N. can be blown directly at the molten pool. Processing of tracks was carried out under a 1.6 kW, 2.00 mm beam at 10 and 20 mms^{-1}.

After preliminary results the O.F.N. was replaced with a 10% H_2 90% N_2 formin gas and specimens were processed under similar beam conditions to those above. but at speeds of traverse between 10 and 80 mms^{-1}. Following initial examination of the formin gas specimens, four specimens were produced which had one face completely laser surface alloyed. The top 0.5mm was then ground off and analysed for total nitrogen content.

Several single track specimens were aged at 575^{o}C in air for 1 hour and other specimens were quenched into liquid nitrogen.

Ammonia gas could not be used as an alloying medium due to ventilation problems.

Results

The structures and hardnesses of the unalloyed laser melted tracks were similar to those described in Chapter 3. The structures and hardnesses of the tracks alloyed using both O.F.N. and Formin gas were very similar to those of the unalloyed tracks.

The specimens which had one face completely alloyed and were then analysed, showed total nitrogen contents ranging from 342 to 384 ppm; corresponding to approximately 8 to 9 x 10^{-3} wt% N.

The structures of the aged specimens were similar to the 420 base material in its received fully tempered condition. No evidence was found, from both optical and scanning electron microscopy, that chromium nitrides had formed and the hardness dropped from ~600 Hv before ageing to ~350 Hv afterwards.

No notable increase in hardness or change in structure was observed when specimens were quenched to -196^{o}C.

Discussion

From Figure A1.1 it can be seen that nitrogen gas at 1 atmosphere pressure is almost insoluble in pure iron at room temperature. At 1600^{o}C nitrogen gas at 1 atmosphere pressure is slightly soluble in pure iron, 0.045 wt%. The effect of various alloying elements on the solubility of nitrogen at 1600^{o}C can be seen in Figure A1.2. 420 steel is basically an iron, 13 wt% chromium steel, so the solubility of nitrogen gas at 1 atmosphere is approximately 0.14 wt% at 1600^{o}C.

When the base material is laser melted, convective flow occurs, Draper[16] has reviewed work on such flow effects, which causes the surface layer to flow to the bottom of the melt pool, thereby removing the oxygen contamination in the form of the Cr_2O_3 film present on the 420 base material. However, if the shrouding was not 100% effective contamination by oxygen could still occur, and thus the Formin gas was used.

When alloying with Formin gas (90%N_2 10%H_2) the hydrogen in the gas should react with any unwanted oxygen, thus eliminating the problem of oxygen contamination if the shrouding is not fully effective. However, the specimens alloyed with Formin gas showed no evidence of nitrogen absorbtion.

The results of the specimens analysed for total nitrogen content, were between 342 and 384 ppm: corresponding to ~ 8 to 9x10^{-3} wt% N. Specifications for "clean" steel usually require the nitrogen content to be

between ~ 1 x 10^{-2} and 4 x 10^{-3} wt%, indicating that there has been no large increase in the nitrogen content by laser surface alloying.

CrN is the principal nitride formed during the case-hardening of steels by nitriding and would be expected to precipitate on ageing at 575^{o}C for 1 hour, if nitrogen was in an extended solid solution. No precipitation of nitrides was noted; again indicating that there has been no large increase in nitrogen content due to laser surface alloying. The reduction in hardness after ageing was due to the tempering of the martensite.

As no notable increase in hardness or change in structure was observed in those specimens quenched to -196^{o}C, it can be assumed that the structure of all the laser nitrided specimens was fully martensitic.

Conclusions

1) Laser surface alloying with nitrpgen using O.F.N. and a Formin gas was unsucessful.

2) No substantial increase in hardness was noted above that achieved by laser surface melting in argon.

Further work

A system should be devised whereby it is safe to use ammonia gas in the shrouding system. From the free energy diagram of nitrides, Figure A1.3 the partial pressure of nitrogen would be ~10^{6} atm at the 1450^{o}C, approximately the melting temperature of the 420 steel, and is thus a far more potent nitriding agent than nitrogen gas at 1 atm.

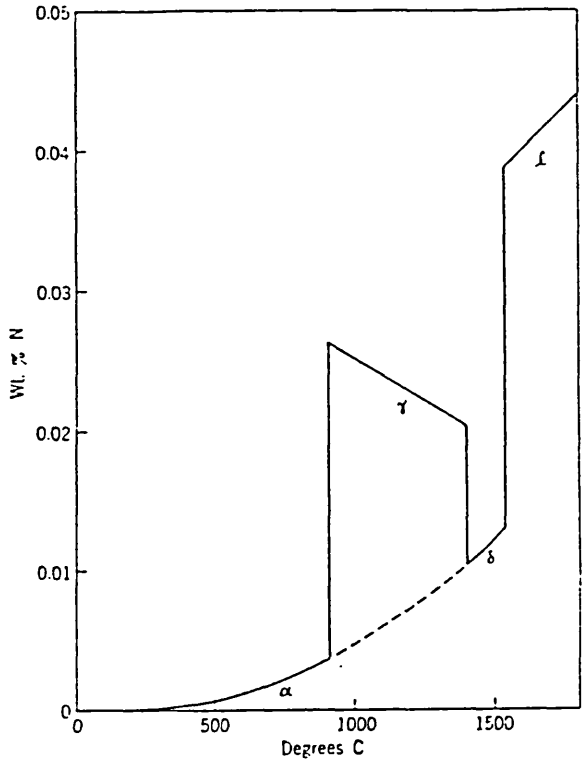


FIGURE A1.1

Solubility of nitrogen gas at 1 atm in iron; stable equilibrium diagram at 1 atm

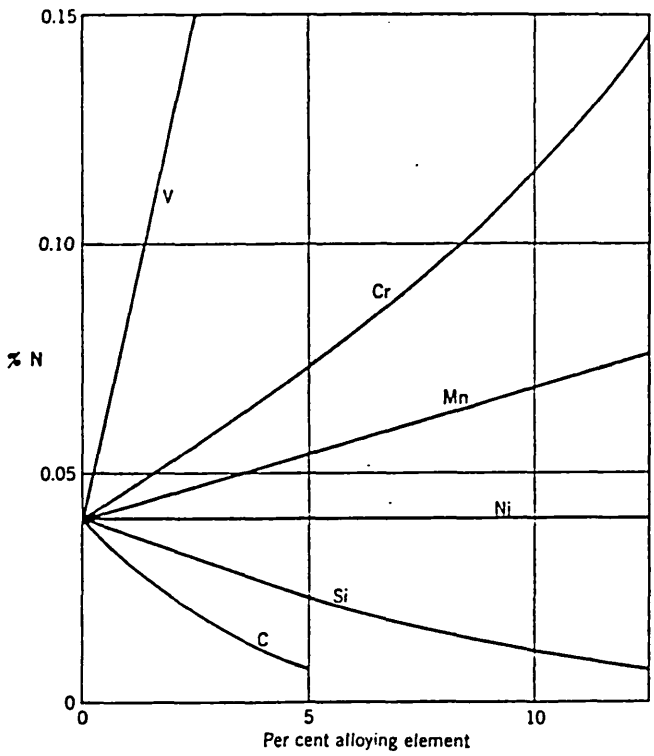


FIGURE A1.2

Effect of alloying elements upon the solubility of nitrogen gas at 1 atm in iron at 1600°C

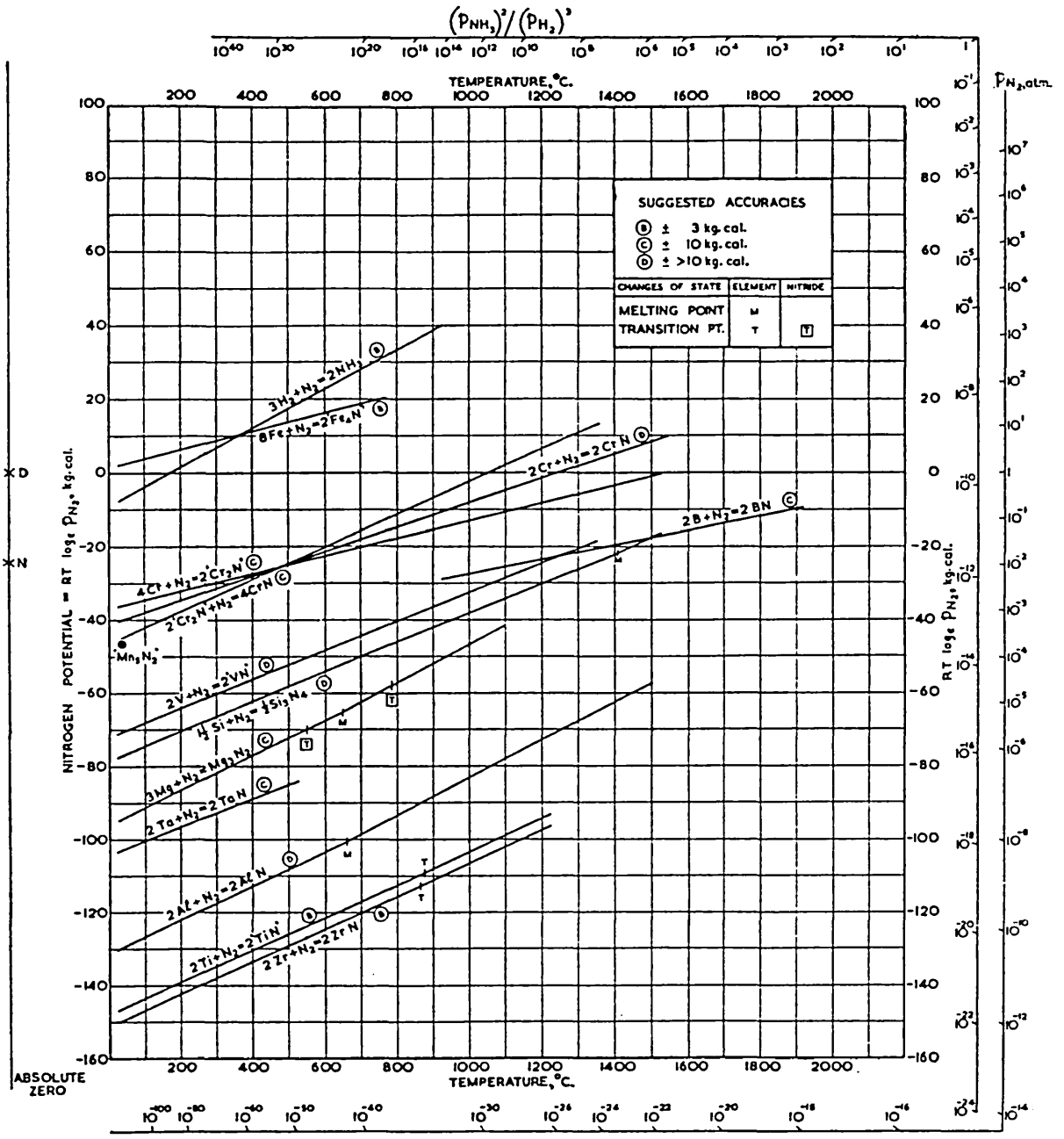


FIGURE A1.3

Free energy diagram of nitrides

APPENDIX 2

The integrated intensity of a diffraction line is given by one of the two equations below depending on whether it is an austenite or martensite line.

For martensite,

$$I_{(\alpha)} = V_\alpha \, v_\gamma \, m_\alpha (LP)_\alpha \, e_\alpha^{-2M} \, (F_\alpha f_\alpha)^2 \quad [A2.1(a)]$$

For austenite,

$$I_{(\gamma)} = V_\gamma \, v_\alpha \, m_\gamma \, (LP)_\gamma \, e_\gamma^{-2M} \, (F_\gamma f_\gamma)^2 \quad [A2.1(b)]$$

Values of f (the atomic factor) were obtained from the International tables[29]. Values of LP (the Lorentz-Polarisation factor), v (the volume of the unit cell) and M (for e^{-2M}) were obtained from Elements of X-ray Diffraction by Cullity[30].

$$LP = \frac{1 + \cos^2 2\Theta}{\sin^2\Theta + \cos\Theta}$$

For B.C.C. F = 2f when (h + k + l) = an even number
For B.C.C. F = 0 when (h + k + l) = an odd number
For F.C.C. F = 4f when h, k and l are either all odd or all even, i.e. unmixed
For F.C.C. F = 0 when h, k and l are mixed.

$v_\gamma = 48.5033$
$v_\alpha = 23.5535$

$$M \text{ (for } e^{-2M}) = \frac{6h^2T}{mK\Theta^2} \left[\Phi(x) + \frac{x}{4}\right] \left(\frac{\sin\Theta}{\lambda}\right)^2$$

where h = Plank's constant
T = the absolute temperature
m = the mass of the vibrating atom
k = Boltzmann's constant
Θ = the Debye characteristic temperature of the substance in °K
λ = the wavelength of incident of X-ray in Å
$x = \Theta/T$
$\Phi(x)$ = a function of x, for which values are given in Appendix 15 of reference 29

$$\frac{6h^2T}{mk\Theta} \text{ reduces to } \frac{1.15 \times 10^4 \, T}{A\Theta^2}$$

where A = Atomic number

For Fe, $\Theta = 430$, $T = 298$ } From Appendix 15 of reference 29

$\therefore x = 1.44$

$\Phi(x) = 0.703$ From Appendix 15 of reference 29

$$\therefore \quad M = \frac{1.15 \times 10^4 \times 298}{56 \times 430^2} \left[0.703 + 0.361 \right] \left(\frac{\sin \Theta}{1.54} \right)^2$$

From the above, Table A2.1 can be deduced and from the information given in Table A2.1, Table A2.2 can be deduced.

Plane	2θ	θ	$\frac{\sin\theta}{\lambda}$	LP	F	m	$\left(\frac{\sin\theta}{\lambda}\right)^2$	e^{-2M}	f
220 α	98.8	49.4	0.492	2.728	23.34	12	0.2425	0.844	11.670
311 γ	90.5	45.25	0.461	2.816	49.38	24	0.2122	0.862	12.345
211 α	81.8	40.9	0.425	3.149	26.41	24	0.1803	0.881	13.205
220 γ	74.4	37.2	0.392	3.683	56.244	12	0.1538	0.898	14.061
200 α	65	32.5	0.348	4.841	30.818	6	0.1214	0.919	15.409
200 γ	50.5	25.25	0.277	8.535	69.96	6	0.0765	0.948	17.475

TABLE A2.1

Plane	V^2	m	LP	e^{-2M}	$(Ff)^2$	=	C		
220_α	48.5033^2	12	2.728	0.844	$(23.340 \times 11.670)^2$	⇒	$C_{\alpha(220)}$	=	4822304016
311_γ	23.5535^2	24	2.816	0.862	$(49.3824 \times 12.345)^2$	⇒	$C_{\gamma(311)}$	=	12011261870
211_α	48.5033^2	24	3.149	0.881	$(26.41 \times 13.205)^2$	⇒	$C_{\alpha(211)}$	=	19050945590
220_γ	23.5535^2	12	3.683	0.898	$(56.244 \times 14.061)^2$	⇒	$C_{\gamma(220)}$	=	1377088385
200_α	48.5033^2	6	4.841	0.919	$(30.818 \times 15.409)^2$	⇒	$C_{\alpha(200)}$	=	14161288440
200_γ	23.5535^2	6	8.535	0.948	$(69.96 \times 17.475)^2$	⇒	$C_{\gamma(200)}$	=	40253902150

TABLE A2.2

APPENDIX 3

The integrated intensities of the $\{311\}_\gamma$, $\{220\}_\gamma$, $\{200\}_\gamma$, $\{211\}_\alpha$, $\{220\}_\alpha$ and $\{200\}_\alpha$ reflections were calculated and the nine possible ratios of I_α/I_γ were used to calculate V_γ. It is the average of these nine values of V_γ which is quoted as the % retained austenite in each case in Table A3.1.

Mass of carbon coating, $\times 10^{-6}$ gmm^{-2}	Degree of overlap, %	Integrated intensities $\{220\}_\alpha$	$\{311\}_\gamma$	$\{211\}_\alpha$	$\{220\}_\gamma$	$\{200\}_\alpha$	$\{200\}_\gamma$	% retained austenite $\pm\sigma$
4.95	1	19.08	8.14	60.59	8.68	22.00	9.20	16.3 ± 8.1
5.18	1	16.41	10.45	60.05	10.51	21.17	13.19	20.7 ± 8.5
7.33	1	16.67	11.50	57.16	11.46	22.19	11.74	21.3 ± 9.0
13.40	67	14.01	10.83	50.90	15.19	23.17	9.55	25.2 ± 10.0
16.00	1	10.97	18.93	32.09	15.81	22.02	84.71	46.3 ± 7.0
11.00	67	8.33	12.77	40.46	22.96	20.77	12.87	34.0 ± 14.0
4.29	67	24.00	5.79	73.71	5.83	22.63	7.27	11.1 ± 6.3
12.90	33	8.59	13.32	40.96	16.21	19.73	10.57	24.5 ± 11.0
4.80	33	18.35	8.89	61.46	8.15	21.46	8.33	16.4 ± 8.6
10.10	33	8.90	12.90	46.85	18.14	22.46	11.39	29.8 ± 12.0
8.30	1	9.15	13.65	40.90	14.21	20.15	16.95	31.5 ± 9.5
3.03	1	18.48	8.40	67.93	7.46	22.80	11.61	15.8 ± 7.0

TABLE A3.1

Position		STRESS MPa					
		Specimen 1 - Unalloyed		Specimen 2 - Alloyed		Specimen 3 - Alloyed	
Depth µm	Distance from centre-line, mm	Transverse	Longitudinal	Transverse	Longitudinal	Transverse	Longitudinal
0	0	-421 ± 49	-181 ± 12	+74 ± 28	-125 ± 6	-274 ± 103	-102 ± 3
0	2	-107 ± 8	-296 ± 23	-188 ± 16	-131 ± 5	+2 ± 10	-111 ± 5
0	4	-94 ± 6	-156 ± 12	-299 ± 17	-104 ± 5	-152 ± 11	-38 ± 9
0	6	-65 ± 5	-354 ± 30	-292 ±12	-89 ± 5	-129 ± 11	+19 ± 15
10	0	-116 ± 7	-120 ± 21	-22 ± 35	-245 ± 5	+74 ± 57	-98 ± 4
10	2	-1344 ± 324	-195 ± 9	-293 ± 24	-145 ± 5	-36 ± 10	-145 ± 7
10	4	-21 ± 7	-247 ± 11	-381 ± 11	+216 ± 12	-199 ± 9	-15 ± 7
10	6	-96 ± 10	-219 ± 24	-423 ± 40	-74 ± 7	-214 ± 20	+65 ± 22
20	0	-105 ± 8	-191 ± 14	-84 ± 25	-281 ± 6	+2974 ± 1322	-136 ± 10
20	2	-211 ± 50	-235 ± 10	-308 ± 27	-156 ± 6	+38 ± 10	-155 ± 6
20	4	-5 ± 8	-190 ± 12	-461 ± 17	+270 ± 10	-271 ± 11	-23 ± 7
20	6	-93 ± 14	-249 ± 32	-438 ± 31	+139 ± 22	-289 ± 27	+124 ± 21
20	0	-146 ± 8	-142 ± 10	--	-288 ± 6	-70 ± 13	-163 ± 4
30	2	-65 ± 26	-207 ± 5	-90 ± 5	-198 ± 7	-183 ± 7	-145 ± 14
30	4	-59 ± 13	-175 ± 18	-88 ± 6	+279 ± 6	-250 ± 15	-13 ± 8
30	6	-101 ± 7	-97 ± 17	-90 ± 5	+145 ± 34	+127 ± 16	+210 ± 18
50	0	-103 ± 12	-184 ± 6	-336 ± 6	-218 ± 6	-18 ± 14	-157 ± 9
50	2	+7 ± 10	-173 ± 6	-334 ± 6	-165 ± 7	-163 ± 13	-144 ± 7
50	4	-69 ± 9	-101 ± 5	-320 ± 6	+242 ± 8	-243 ± 12	-20 ± 4
50	6	-104 ± 7	+7 ± 29	-252 ± 7	+115 ± 40	+184 ± 17	+194 ± 21
70	0	-88 ± 34	-15 ± 11	-198 ± 8	-97 ± 10	+43 ± 26	-98 ± 9
70	2	+78 ± 12	-157 ± 9	-241 ± 6	-65 ± 10	-142 ± 10	-140 ± 7
70	4	-12 ± 9	-65 ± 12	-236 ± 7	+215 ± 7	-203 ± 12	-17 ± 17
70	6	-62 ± 12	+28 ± 27	-163 ± 20	+165 ± 35	+189 ± 15	+162 ± 13
100	0	-17 ± 52	-142 ± 11	-117 ± 4	-7 ± 10	+12 ± 14	-48 ± 7
100	4	+10 ± 9	-79 ± 7	-161 ± 5	+208 ± 9	-82 ± 13	-13 ± 7
100	6	-63 ± 10	+19 ± 14	--	+101 ± 40	+174 ± 28	+111 ± 31
130	0	+115 ± 1	-143 ± 16	-67 ± 6	+44 ± 8	+132 ± 37	+19 ± 7
130	2	+21 ± 6	-152 ± 7	-101 ± 5	+46 ± 5	+11 ± 9	-49 ± 7
130	4	-48 ± 7	-71 ± 15	-122 ± 5	+200 ± 9	-112 ± 8	+40 ± 6
130	6	-34 ± 30	+31 ± 16	-98 ± 7	+100 ± 87	-56 ± 17	+185 ± 33
160	0	+52 ± 29	-154 ± 7	-64 ± 7	+40 ± 5	+156 ± 16	+133 ± 31
160	2	+33 ± 8	-13 ± 8	-110 ± 7	+43 ± 4	+91 ± 11	+19 ± 7
160	4	+9 ± 65	-99 ± 12	-109 ± 6	+180 ± 7	+46 ± 10	-49 ± 7
160	6	+176 ± 33	+59 ± 2	-109 ± 6	+288 ± 54	-36 ± 11	+40 ± 6
200	0	+5 ± 33	-146 ± 6	+1 ± 7	+37 ± 7	+156 ± 18	+112 ± 7
200	2	-87 ± 48	-121 ± 9	-36 ± 4	+62 ± 5	+114 ± 6	+51 ± 8
200	4	+9 ± 10	-96 ± 7	-105 ± 5	+174 ± 5	+90 ± 8	+141 ± 11
200	6	+32 ± 25	+39 ± 21	-91 ± 6	-54 ± 99	+44 ± 19	+122 ± 23
250	0	+101 ± 7	+136 ± 68	-81 ± 6	+5 ± 8	+159 ± 10	-179 ± 182
250	2	+43 ± 8	+167 ± 28	-165 ± 11	+7 ± 6	+51 ± 8	+17 ± 10
250	4	-262 ± 140	+131 ± 11	-138 ± 12	+53 ± 11	-31 ± 9	+44 ± 9
250	6	-112 ± 16	+76 ± 33	-153 ± 18	-163 ± 144	-173 ± 18	-81 ± 32

APPENDIX 4

Residual stress data